

BORON INTERACTION WITH GERMANIUM AND SELF-INTERSTITIALS IN  
SILICON

By

LJUBO RADIC

A DISSERTATION PRESENTED TO THE GRADUATE SCHOOL  
OF THE UNIVERSITY OF FLORIDA IN PARTIAL FULFILLMENT  
OF THE REQUIREMENTS FOR THE DEGREE OF  
DOCTOR OF PHILOSOPHY

UNIVERSITY OF FLORIDA

2006

Copyright 2006

by

Ljubo Radic

This document is dedicated to the professors that perpetually ask the question:  
And why is that?

## ACKNOWLEDGMENTS

I would like to thank my advisor, Dr. Mark E. Law, for the support and guidance throughout this work. This section would be incomplete without a mention of my colleagues from the SWAMP group, whom I owe many an interesting discussion. This includes Ibrahim Avci, Tony Saavedra, Renata Camillo-Castillo, Robert Crosby, Robert Robison, Chad Lindfors, Michelle Phen and others.

## TABLE OF CONTENTS

	<u>page</u>
ACKNOWLEDGMENTS .....	iv
LIST OF TABLES .....	vii
LIST OF FIGURES .....	viii
ABSTRACT .....	xiii
CHAPTER	
1 INTRODUCTION .....	1
1.1 Brief Historical Overview.....	1
1.2 MOS Transistor Structure.....	3
1.3 MOS Transistor Operation .....	3
1.3.1 Limiting Factors in MOS Performance .....	4
1.3.2 MOS Transistor Scaling .....	4
1.4 Semiconductor Processing Technologies .....	5
1.4.1 Ion Implantation .....	6
1.4.2 Diffusion.....	9
2 LITERATURE REVIEW .....	22
2.1 Dopant Diffusion in Silicon.....	22
2.2 Self-diffusion in Silicon.....	24
2.3 Germanium Diffusion in $\text{Si}_{1-x}\text{Ge}_x$ .....	25
2.4 Boron Diffusion in Silicon.....	27
2.4.1 Boron as Interstitial Diffuser in Silicon.....	27
2.4.2 Pre-amorphization and B.....	28
2.5 Boron-interstitial Clusters.....	29
2.6 Boron Diffusion in $\text{Si}_{1-x}\text{Ge}_x$ .....	31
2.7 Modeling Boron Diffusion in $\text{Si}_{1-x}\text{Ge}_x$ .....	35
3 BORON CLUSTERING IN SILICON .....	62
3.1 Boron-interstitial Cluster Dissolution.....	62
3.1.1 Introduction .....	62
3.1.2 Experimental.....	64

3.1.3 Results and Discussion .....	65
3.1.4 Modeling.....	67
3.2 Boron Cluster Formation and Preamorphization.....	68
3.2.1 Experiment and Findings.....	68
3.2.2 Modeling.....	70
3.3 Conclusion.....	75
4 BORON CAPTURE AT THE OXIDE/SILICON INTERFACE AND END-OF-RANGE DISLOCATION LOOPS .....	98
4.1 B Interaction with Oxide/silicon Interface Under TED.....	98
4.1.1 Experimental Conditions.....	98
4.1.2 Simulations.....	102
4.2 Boron Segregation to the EOR Loops .....	104
4.2.1 Experimental.....	105
4.2.2 Simulations.....	105
4.3 Conclusions.....	106
5 BORON INTERACTION WITH GERMANIUM UNDER INTERSTITIAL SUPERSATURATION .....	127
5.1 Prior Work - Model Implementation .....	127
5.1.1 Bandgap Narrowing.....	127
5.1.2 Boron Diffusion in Si and Interaction with Ge .....	128
5.2 Experiment Design and Considerations.....	129
5.2.1 Experimental Conditions.....	131
5.2.2 Experimental Results.....	132
5.2.3 Simulations.....	133
5.3 Constant B Concentration Experiment .....	134
5.3.1 Experimental conditions and results.....	134
5.3.2 Simulations.....	136
5.4 Conclusions.....	136
6 SUMMARY AND FUTURE WORK .....	151
6.1 Summary.....	151
6.2 Future Work.....	153
6.2.1 Material Specification – B Marker Layers in Relaxed Si <sub>1-x</sub> Ge <sub>x</sub> .....	153
6.2.2 Information Expected .....	154
LIST OF REFERENCES.....	157
BIOGRAPHICAL SKETCH .....	162

## LIST OF TABLES

<u>Table</u>	<u>page</u>
2-1 Extracted B diffusivity prefactor ( $D_0$ ) and activation energy ( $E^a$ ) from experiment of Zangenberg et al.....	38
3-1 Retained boron dose [ $\text{cm}^{-2}$ ] in different processing steps. ....	77
4-1 Sample labels and implant sequence, showing Ge implant dose as the only variable in the sequence .....	108
4-2 Active dose and carrier type measured by Hall-van der Pauw system .....	109
4-3 Integrated dose from the measured B profiles in the control sample annealed at $825^\circ\text{C}$ , taking full profile ( $Q_1$ ) and ignoring the surface spike ( $Q_2$ ).....	110
4-4 Integrated dose from the measured B profiles in the $4 \times 10^{15} \text{ cm}^{-2}$ Ge implanted sample annealed at $825^\circ\text{C}$ , taking full profile ( $Q_1$ ) and ignoring the surface spike ( $Q_2$ ).....	111

## LIST OF FIGURES

<u>Figure</u>	<u>page</u>
1-1 Triode electron tube schematic .....	14
1-2 Number of components per integrated circuit vs. time, later known as “Moore’s law” .....	15
1-3 Number of transistors vs. time, shown to realize the original prediction of G. E. Moore, as well as updated trends .....	16
1-4 Schematic cross-section of a nMOSFET transistor.....	17
1-5 Schematic of an ion implanter .....	18
1-6 Illustration of an ion implantation process, in particular (a) a single ion path and (b) the resulting damage cascade .....	19
1.7 Silicon crystal viewed from (a) $\langle 110 \rangle$ direction and (b) tilted $\sim 10^\circ$ off the $\langle 110 \rangle$ direction .....	20
1.8 Illustration of fluxes entering and exiting a given volume.....	21
2-1 Diffusion mechanisms in silicon: a) interstitialcy diffusion, b) kick-out, c) vacancy diffusion, and d) concerted exchange .....	39
2-2 Self-diffusion in Si as measured by Bracht , with symbols denoting different samples .....	40
2-3 Self-diffusion in Si as measured by Ural et al. Dots represent measured diffusivities, solid line is the best fit expression for self-diffusion. ....	41
2-4 Interstitial fraction, $f_{Si}$ of the self-diffusion from Ural et al. The lines represent predictions from several metal diffusion experiments. ....	42
2-5 Germanium diffusivities for various temperatures and Ge contents, after Zangenberg et al .....	43
2-6 Activation energies and prefactors for various Ge contents, after Zangenberg .....	44
2-7 Activation energies and prefactors for various Ge contents, after Strohm .....	45

2-8	Comparing diffusivities of Ge in $\text{Si}_{1-x}\text{Ge}_x$ as measured by Zangenberg and Strohm .....	46
2-9	Comparison of Ge diffusion with respect to ambient and consequential interstitial or vacancy supersaturation .....	47
2-10	B profiles after an implant of $2 \times 10^{14}$ at 60keV, annealed at a) 800 °C and b) 950°C .....	48
2-11	B profiles, as-grown and after 1h at 670°C .....	49
2-12	Fractional activation and sheet resistance of samples annealed at 750°C for: a) varying B dose at 80keV, and b) $4 \times 10^{14} \text{ cm}^{-2}$ at varying energy .....	50
2-13	B profiles used in experiment by Mirabella et al. showing the as-grown, annealed for 2 min at 815°C, as well as illustrating the methodology for determining the active fraction .....	51
2-14	Time evolution of the clustered B dose during annealing at 815 to 950 °C, with extracted time constants. ....	52
2-15	Structure used by Kuo et al. with a B marker layer in the $\text{Si}_{0.83}\text{Ge}_{0.17}$ strained layer .....	53
2-16	Diffused B profiles after 30 minute anneal at 860°C in a) Si and b) $\text{Si}_{0.83}\text{Ge}_{0.17}$ ....	54
2-17	Effective B diffusivity as a function of B concentration .....	55
2-18	Diffusivity of B in $\text{Si}_{0.7}\text{Ge}_{0.3}$ layer .....	56
2-19	B profiles in multiplayer structure before (dashed line) and after (solid line) annealing at 975°C .....	57
2-20	Illustration of a structure used by Kuo et al. showing relaxed $\text{Si}_{1-y}\text{Ge}_y$ and pseudomorphic $\text{Si}_{1-x}\text{Ge}_x$ .....	58
2-21	B diffusivity at 800°C as a function of strain, with the numbers in the parenthesis are (x,y) Ge content. Positive strain represents biaxial tension and negative strain biaxial compression. ....	59
2-22	Schematic description of the structure used by Zangenberg et al. to measure B diffusion in $\text{Si}_{1-x}\text{Ge}_x$ .....	60
2-23	B profiles before (thin line) and after (thick) 850°C annealing of a given B well concentration. ....	61
3-1	Secondary ion mass spectrometry (SIMS) measured boron profiles of investigated implant conditions after first anneal step, 750°C for 30 minutes in inert ambient.....	78

3-2	Secondary ion mass spectrometry (SIMS) measured boron profiles. Initial condition is after 750°C, 30 minutes inert anneal. Subsequent anneal is 850°C, 60 minutes in respective ambient. ....	79
3-3	Active dose measured by Hall-van der Pauw method, during the annealing at 850°C. The time zero measurement corresponds to the condition after a 750°C, 30 minutes inert anneal. ....	80
3-4	Active fraction, the ratio of active to retained dose (integrated SIMS profile), compared for the different annealing ambient at the end of the 850°C, 60 minutes anneal. The initial condition is after a 750°C, 30 minutes inert anneal. ....	81
3-5	Major cluster formation and dissolution paths of Liu et al. with B <sub>3</sub> I and B <sub>2</sub> I <sub>3</sub> containing most of the B clustered dose in figure a) and simulation of B clustering and dissolution during thermal processing used in experiment in figure b) ....	82
3-6	Cluster formation and dissolution paths of modified Liu et al. energetics, with B <sub>4</sub> I <sub>4</sub> and B <sub>2</sub> I <sub>3</sub> containing most of B clustered dose, are shown in figure a), with simulation of B clustering and dissolution (modified energetics) during thermal processing used in experiment is shown in figure b) ....	83
3-7	Boron profiles of material used in the study of Jones et al., unimplanted and annealed in inert ambient at 800°C .....	84
3-8	Boron profiles after a 5x10 <sup>15</sup> Si implant at 146keV, annealed in inert ambient at 800°C .....	85
3-9	Boron marker layers and excess interstitial damage following a 146keV Si implant shows proximity of deepest marker layer to the damage.....	86
3-10	Doses of important clusters in a simulation of a B 4x10 <sup>14</sup> 20keV implant into crystalline Si, during a 30 minutes 750°C anneal, resulting in activation ~18% .....	87
3-11	Doses of important clusters in a simulation of a B 4x10 <sup>14</sup> 20keV implant into preamorphized Si (with excess interstitial dose increased by a factor of 6), during a 30 minutes 750°C anneal, resulting in activation >85%.....	88
3-12	Doses of important clusters in a simulation of a B 4x10 <sup>14</sup> 20keV implant into preamorphized Si (at liquid nitrogen temperatures), during a 30 minutes 750°C anneal, resulting in activation >90%.....	89
3-13	Simulated boron profiles after 5 seconds at 800°C, following a Si implant of 5x10 <sup>15</sup> cm <sup>-2</sup> at 146keV. Diffusion of self-interstitials and BI pairs are annulled in the amorphous material. ....	90

3-14	Simulated boron profiles after 30 seconds at 800°C, following a Si implant of $5 \times 10^{15} \text{ cm}^{-2}$ at 146keV. Diffusion of self-interstitials and BI pairs are annulled in the amorphous material. ....	91
3-15	Simulated boron profiles after 3 minutes at 800°C, following a Si implant of $5 \times 10^{15} \text{ cm}^{-2}$ at 146keV. Diffusion of self-interstitials and BI pairs are annulled in the amorphous material. ....	92
3-16	Simulated boron profiles after 5 seconds at 800°C, following a Si implant of $5 \times 10^{15} \text{ cm}^{-2}$ at 146keV. Diffusion of self-interstitials and BI pairs are annulled in the amorphous material, and the binding energies of small BICs are reduced. ....	93
3-17	Simulated boron profiles after 30 seconds at 800°C, following a Si implant of $5 \times 10^{15} \text{ cm}^{-2}$ at 146keV. Diffusion of self-interstitials and BI pairs are annulled in the amorphous material, and the binding energies of small BICs are reduced. ....	94
3-18	Simulated boron profiles after 3 minutes at 800°C, following a Si implant of $5 \times 10^{15} \text{ cm}^{-2}$ at 146keV. Diffusion of self-interstitials and BI pairs are annulled in the amorphous material, and the binding energies of small BICs are reduced. ....	95
3-19	Simulated clustered doses in BIC experiment for B implant $4 \times 10^{14} @ 20 \text{ keV}$ , model presented earlier in the chapter.....	96
3-20	Simulated clustered doses in BIC experiment for B implant $4 \times 10^{14} @ 20 \text{ keV}$ , model parameters adjusted to cover regrowth behavior .....	97
4-1	Profiles of B and Ge in as-implanted sample A .....	112
4-2	Cross-section TEM (XTEM) images of samples (a) A and (b) D under 100000 magnification.....	113
4-3	B profiles from Ge implanted samples during annealing at 700°C.....	114
4-4	B profiles from Ge implanted samples during annealing at 825°C.....	115
4-5	SIMS profiles of Ge, As and B in samples: A, with $4 \times 10^{15} \text{ cm}^{-2}$ Ge (1min@825°C), B with $1.2 \times 10^{15} \text{ cm}^{-2}$ Ge (as-implanted) and C with $4 \times 10^{14} \text{ cm}^{-2}$ Ge (as-implanted) per figure a, b, c, respectively .....	116
4-6	B profiles from control sample during annealing at 700°C.....	117
4-7	B profiles from control sample during the annealing at 825°C.....	118
4-8	Simulated B profiles of control sample during anneals at 825°C.....	119
4-9	Simulated B profiles of control sample during anneals at 825°C, diffusion enhancement factor reduced five times .....	120

4-10	Simulated B profiles of control sample during anneals at 825°C, assuming surface trapping of BI.....	121
4-11	Simulated B profiles of $4 \times 10^{15} \text{ cm}^{-2}$ Ge implanted sample (As contaminated) during anneals at 825°C, assuming electric field effect dominant .....	122
4-12	B profiles from sample E1 during annealing at 750 °C.....	123
4-13	B profiles from sample E1 during annealing at 825°C.....	124
4-14	Simulated B profiles of B segregation to the loops in sample E1 during annealing at 750°C .....	125
4-15	Simulated B profiles of B segregation to the loops in sample E1 during annealing at 825°C .....	126
5-1	Profiles of B and Ge in as-implanted sample 2A .....	138
5-2	Cross-section TEM (XTEM) image of sample 2A under 100000 magnification ..	139
5-3	Boron profiles during the annealing at 780°C for: a) Ge implanted sample, b) control sample .....	140
5-4	Simulated B profiles of Ge implanted sample during anneals at 780°C .....	141
5-5	Simulated B profiles of control sample during anneals at 780°C.....	142
5-6	B profiles from control sample during annealing at 750 °C.....	143
5-7	B profiles from control sample during annealing at 825°C.....	144
5-8	B profiles from Ge implanted sample during annealing at 750 °C .....	145
5-9	B profiles from Ge implanted sample during annealing at 825 °C .....	146
5-10	B profiles from Ge implanted sample during annealing at 560 °C .....	147
5-11	B profiles from Ge implanted sample during annealing at 600 °C.....	148
5-12	Simulated B profiles from Ge implanted samples during annealing at 750°C.....	149
5-13	Simulated B profiles from Ge implanted samples during annealing at 825°C.....	150
6-1	Dopant profiles in a $\text{Si}_{1-x}\text{Ge}_x$ material. Figure a) contains Ge profile for $\text{Si}_{0.8}\text{Ge}_{0.2}$ material, while figure b) has B profile .....	155
6-2	Boron profile in $\text{Si}_{0.8}\text{Ge}_{0.2}$ material .....	156

Abstract of Dissertation Presented to the Graduate School  
of the University of Florida in Partial Fulfillment of the  
Requirements for the Degree of Doctor of Philosophy

BORON INTERACTION WITH GERMANIUM AND SELF-INTERSTITIALS IN  
SILICON

By

Ljubo Radic

August 2006

Chair: Mark E. Law

Major Department: Electrical and Computer Engineering

Understanding the diffusion phenomena in silicon is imperative for the rapid and efficient development of the future semiconductor processes. Boron is pertinent as the dopant of choice in formation of a p-type semiconductor, yielding higher activation and carrier mobilities than the alternatives. In order to overcome certain transient behavior, such as transient diffusion enhancement and clustering, these phenomena have to be characterized and modeled.

One part of this dissertation describes the investigation of the properties of the significant boron-interstitial clusters (BICs). Previous models described boron clustering through the single dominant cluster, assumed to be interstitially poor. An experimental investigation of the BIC dissolution with respect to annealing ambient revealed a reaction contrary to the expectations from that model, suggesting that one of the dominant clusters may be interstitially rich. Additionally, the time dependence of the reactivation indicated the reactivation process was coming from two sources. Using a set of ab-initio

calculations as a starting point, adjusting to dependence on the annealing ambient, the model showed appropriate reaction. An earlier experiment probed the formation of the BICs with a separation by amorphous/crystalline interface. Assuming the inability of the self-interstitial or boron-interstitial pair to enter the amorphous layer significantly reduces the cluster formation. However, further adjustments were necessary to properly capture the difference between the enhanced diffusion phenomena in the regrown amorphous layer, and a distinct clustering peak in the crystalline material.

Another part of the dissertation examines the interaction of Ge and B in silicon under interstitial supersaturation. Experimentally observed segregation of B onto oxide/silicon interface in samples with no Ge implant did not occur in the presence of Ge. In conjunction with increase in peak concentration of B in the presence of Ge, this experimental evidence supports an earlier hypothesis of the Ge-B pairing as the cause of the diffusivity reduction of B in  $\text{Si}_{1-x}\text{Ge}_x$ . Modifying the model to account for the interstitial supersaturation and extracting the pair formation energy from a relative increase in the diffusion activation energy in higher Ge concentration, the model qualitatively captures the phenomena.

## CHAPTER 1 INTRODUCTION

### **1.1 Brief Historical Overview**

The twentieth century saw several significant changes in the fields of engineering. The advent of the vacuum tube gave rise to the field of electronics. It consisted of the filament as the emissive element, cathode, anode and the control grid (Fig. 1-1). With negative voltage applied to the grid the cathode current could be cut off, while increasing the control voltage amplified the current. Amplification of the signal made long distance phone and radio communication practical.

One of the significant benefits of the vacuum tubes is the simplicity of construction. In the 1930s, Julius Edgar Lilienfeld filed two patents for controlling electric current [Lil30] which would today be described as MESFET (metal-semiconductor field effect transistor) and depletion-mode MOSFET (metal-oxide-semiconductor field effect transistor). Since the clean environment and surface control required to produce viable semiconductor material were not available before the middle of the twentieth century, his inventions were forgotten until twenty years later.

Another application of cathode tubes was in early computers. Electronic Numerical Integrator And Computer (ENIAC) was the first electronic computer, built from 1943 to 1946, and it contained 17,468 vacuum tubes, 7,200 crystal diodes, 1,500 relays, 70,000 resistors, 10,000 capacitors and around 5 million hand-soldered joints. It required rewiring for execution of a new program, and could perform 5000 additions per second while consuming 160kW of power.

The first fully functional transistor was developed at Bell Laboratories, by John Bardeen, Walter Houser Brattain, and William Bradford Shockley, who were awarded the Nobel Prize in physics in 1956. Though their goal was to use the high quality germanium crystals to form a field-effect transistor (FET) predicted by Lilienfeld, but they actually found a bipolar junction transistor (BJT). After some time, and a number of solved problems, the percentage of functional transistors (yield) was still not very high and production of high purity germanium still posed a problem. In the 1960s, Texas Instruments tried using silicon instead of germanium, which was easier to work with. Several factors led to the ascent of the silicon based MOSFETs: water insoluble native oxide ( $\text{SiO}_2$ ), physical and electrical properties of the oxide, no interface states between the silicon and the oxide that could serve as electron traps or recombination sites, as well as improvements in production facilities. By that time, transistors replaced majority of the vacuum tubes.

The trend of miniaturization continued as Jack Kilby [Kil59] at Texas Instruments patented a “solid circuit” in germanium. Soon afterwards, Robert Noyce of Fairchild Semiconductor was awarded a patent for a "unitary circuit" made of silicon. Planar MOSFET technology scaling has been driving the semiconductor technologies since then. As expressed in an observation by Gordon E. Moore [Moo65], the number of transistors per square inch on integrated circuits had doubled every year since the integrated circuit was invented (Fig. 1-2). This growth continues, as shown in Fig. 1-3 [Moo03], to this day. The rest of the introduction will concentrate on MOS technology as the dominant technology today.

## 1.2 MOS Transistor Structure

MOSFET transistors fall into the category of unipolar transistors, meaning that only one carrier type is responsible for conduction. While different types of FETs control the conduction between the source and the drain (S/D) electrodes in different ways, all of them operate with either electrons or holes. This is not the case for the BJT, where both carrier types are involved.

MOS transistors can be divided into several types. First, the transistor can have a n-type or a p-type channel. Second, the transistor can have a channel existing or not, with no voltage applied to the gate electrode. In case there is an electrical connection existing between the source and the drain region, the device is said to be a depletion mode device. Otherwise, there is no connection unless the proper voltage is applied to the gate, such as in enhancement mode device. Most transistors in digital circuits are used as switches, for which the enhancement mode device is more suitable.

## 1.3 MOS Transistor Operation

The schematic cross-section of an enhancement mode nMOSFET is shown in Fig. 1-4. The external contacts are source, drain, and gate. Body contact is usually connected to the source, thus physically differentiating between the source and the drain. This also forms a reverse polarized  $pn$  junction at the drain-body boundary, as  $V_{DS} > 0$  is necessary for nMOS operation. For a  $V_{GS}$  lower than the threshold voltage  $V_T$ , the p-type region separates the source and the drain allowing no current flow, and the device is said to be turned off. As the  $V_{GS}$  increases to values over the  $V_T$ , the electron rich region forms a channel near the surface between the source and the drain. This facilitates the current flow from the drain to the source, and the device is said to be turned on. Therefore, the

gate voltage  $V_{GS}$  controls the current flow between the drain and the source with the transistor acting as a switch.

### 1.3.1 Limiting Factors in MOS Performance

The MOS device performance is limited by the design and the parasitic effects. The design parameters, such as gate length, width, and oxide thickness, gate material, source and drain region thickness, factor in to determine the transistor's performance. The parasitic effects are leakage currents, parasitic resistances and capacitances. The technologically necessary overlap of the gate over the source and the drain region forms two capacitors:  $C_{GS}$  and  $C_{GD}$ . Even though the capacitance amounts are usually similar, the latter is electrically more significant. During the switching from an off state into an on state, the transistor operates as a small signal amplifier. The increase in the small signal difference between the gate and the drain effectively increases  $C_{GD}$  by the voltage amplification factor. The parasitic resistances include the resistances in the S/D regions, their extensions, transition resistances towards metal contact, and internal resistance of the poly-silicon gate electrode.

### 1.3.2 MOS Transistor Scaling

The continued advances of semiconductor technology, expressed in transistor density and speed, are due to the scaling of the planar technology on silicon and the properties of silicon dioxide. Reduction in gate length had increased the current and reduced the input capacitance, both of which reduce switching time. Decreasing the dimensions of the transistor also meant that more transistors were available per chip, thus increasing the computing power.

The decrease of the dimensions of the transistor does pose some technological difficulties. The breakdown electric field of the silicon dioxide is a material property one

can not circumvent. Thus the scaling limited by the maximum electric field is labeled constant field scaling, requiring the reduction of the gate voltage in proportion to the reduction of the oxide thickness. As the source and the drain regions come closer together, the depletion regions could touch or merge, giving rise to a leakage current irrespective of the gate voltage. This is known as sub-threshold leakage, causing problems with the power consumption and the detection whether the transistor is on or off. Similarly, the reduction of the lateral dimensions increases the capacitances between metal lines. The reduction of physical dimensions also requires reduction in operating voltages in order to keep below the breakdown electric field of the oxide. Though the operating voltage is reduced, the extremely small oxide thickness poses a problem as tunneling becomes significant with several monolayer thick oxides. New materials with higher dielectric constants, allowing for thicker layer, have also been introduced. In order to keep the conduction of the transistor under the control of the gate, the conduction must take place on or near the surface. With reduction of operating voltages that area is reduced as well. This means that source and drain region depths have to be scaled with the lateral dimensions. The parasitic resistances of S/D are inverse proportional to the depth, thus requiring increased doping to keep them fixed. The contact material and resistance also play a role in the parasitics, somewhat mitigated by the recent switch from Al to Cu for metal interconnects.

#### **1.4 Semiconductor Processing Technologies**

Semiconductor integrated circuits are formed by an application of following processes: (1) growth or a deposition of a layer, (2) exposure to light, (3) patterning or etching, (4) dopant implantation, and (5) thermal annealing. The latter two are the

frequently used to form the n-type or p-type semiconductor regions, later to become a part of the device, and will be discussed in further detail.

### 1.4.1 Ion Implantation

Ion implantation is the dominant method of introducing dopant into silicon material. The accuracy of the implanted dose and the dopant distribution in depth are the reason for its widespread use. The process of ion implantation begins with a gas or a solid source providing an ionized beam (Fig. 1-5). The ion beam then goes through a magnet and an aperture, providing the mass separation of elements and isotopes extracted from the source. The voltage used to accelerate the ions from the source is called the extraction voltage. The extraction voltage and the acceleration voltage both contribute to the final ion's implant energy. The ion beam passes through the scanning plates in  $x$  and  $y$  directions, and the deflection before reaching the target wafer. The wafer sits in a Faraday cage that repels the incidental electrons and integrates the incoming charge from the ion beam. The direct and accurate measurement of the incoming ion beam current, also the implanting dose rate, provides the accuracy in the total implanted dose. The aforementioned deflection serves to remove neutrals, ions that lost the charge between the aperture and the scan plates, from the beam reaching the target wafer and introducing an error in the dose measurement.

The two major mechanisms of the energy loss of an ion entering the crystal lattice are electron ( $S_e$ ) and nuclear ( $S_n$ ) stopping (Eq. 1-1), with  $N$  as the lattice density.

$$-\frac{dE}{ds} = N \cdot (S_e(E) + S_n(E)) \quad (1-1)$$

As the incoming ions enter the crystal lattice, they are stripped of the outer electron shell and slowed by the interaction with (“drag” of) the bound and free electrons. The stopping energy can be approximated by a velocity proportional, and expressed as

$$S_e(E) \cong k \cdot \sqrt{E} \quad (1-2)$$

Nuclear stopping involves Coulombic interaction between the ion and the host lattice atom. As the ion approaches the target atom, the electrostatic repulsion deflects the ions path, and/or removes the host atom from its lattice position. In the case neither the ion nor the host atom occupy the lattice position, the collision has produced a vacancy and an interstitial atom (the dislodged host atom). Alternatively, the ion performs a replacement collision, by removing the host atom from a lattice position and occupying it, thus becoming substitutional and creating a self-interstitial.

For practical calculations, nuclear stopping can be approximated [Zie00a] by

$$S_n(E) = \frac{8.462 \cdot 10^{-15} \cdot Z_1 Z_2 M_1}{(M_1 + M_2)(Z_1^{0.23} + Z_2^{0.23})} S_n(\varepsilon) [eV / (atom / cm^2)] \quad (1-3)$$

where the  $Z$  and  $M$  are atomic number and mass, subscripts 1 and 2 denote ion and target atoms, and the reduced energy  $\varepsilon$  is

$$\varepsilon = \frac{32.53 M_2 E_0}{Z_1 Z_2 (M_1 + M_2)(Z_1^{0.23} + Z_2^{0.23})} \quad (1-4)$$

and the reduced nuclear stopping  $S_n(\varepsilon)$  can be calculated as

$$\text{for } e < 30: S_n(\varepsilon) = \frac{\ln(1 + 1.1383\varepsilon)}{2(\varepsilon + 0.01321\varepsilon^{0.21226} + 0.19593\varepsilon^{0.5})} \quad (1-5)$$

$$\text{for } e > 30: S_n(\varepsilon) = \frac{\ln(\varepsilon)}{2\varepsilon} \quad (1-6)$$

The occurrence of collision events is random and makes the individual ion path rather difficult to predict (Fig. 1-6a). Though the individual ion travels a distance  $R$ , the peak of ion distribution is the mean projected range  $R_p$ , a far more interesting value. The projected range is defined as

$$R_p = \frac{1}{N} \sum_i x_i \quad (1-7)$$

where  $x_i$  is the depth of a given ion  $i$ . It can also be approximated [Lin63] by

$$R_p = \frac{R}{1 + \frac{M_2}{3M_1}} \quad (1-8)$$

In ideal case of uniform and amorphous target, with collision frequency and energy transfer per collision being random, the implanted ion distribution can be described by a Gaussian function  $N(x)$ . Implant dose is  $Q$ , and  $\Delta R_p$  is the vertical distribution spread.

$$N(x) = \frac{Q}{\Delta R_p \sqrt{2\pi}} \exp\left(-\frac{(x - R_p)^2}{2\Delta R_p^2}\right) \quad (1-9)$$

For a crystalline target, the distribution is somewhat different. Certain directions in the crystal structure allow for less collisions and deeper penetration, commonly referred to as channeling. The nuclear stopping is minimal in the case of channeling, as the angle of incidence is rather small and the Coulombic repulsion keeps the ion in the channel. The electron stopping is smaller, thus allowing the ion to travel significantly longer distances. Fig. 1.7 illustrates the difference between looking into a channel and when the tilt is applied. Wafer tilt and twist are used to prevent channeling by providing seemingly random distribution of silicon atoms on the surface plane. Also, a sacrificial oxide layer

called screening oxide is sometimes used to randomize the incoming ion's trajectories before entering the silicon lattice.

During a single ion's path, it may displace as much as  $10^4$  silicon atoms by nuclear collisions before it comes to rest (Fig. 1-6b). If the primary ion collides with a host lattice atom with more than the energy of displacement  $E_d$  ( $E_d$  is 14 eV for silicon [Bau69]), the now interstitial atom continues to travel through the lattice until it collides with another lattice atom, thus creating additional damage cascades. The damage depends on the atomic species, as heavier atoms lose most of their energy in collisions, while lighter atoms initially lose a significant portion of their energy due to electronic stopping. In case of high implant doses, the damage can displace a percentage of the lattice atoms (over 10% [Chr81]), creating amorphous zones. The amorphization is sometimes used as an introductory step in low energy implants to prevent channeling, called pre-amorphization implant (PAI).

After the implantation step is complete, there can be a significant interstitial and vacancy concentrations in the implanted region. Only a small portion of the implanted dopant atoms has occupied the lattice positions rendering them electrically inactive. These damaged regions need to be restored to a monocrytalline lattice and dopants activated, which is accomplished by a high temperature thermal treatment.

#### 1.4.2 Diffusion

Fick's laws describe diffusion of given specie, as the change of concentration with respect to position and time. Diffusion is a thermally activated process, so one can write the probability  $p$  of an atom species  $X$  hop between two lattice positions as

$$p = \exp\left(-\frac{\Delta G_X^m}{kT}\right) \quad (1-10)$$

where  $\Delta G_x^m$  is migration energy of a species  $X$ , and  $k$  is the Boltzmann constant. The frequency of hop attempts could be approximated by the Debye frequency  $\nu$ , which makes the frequency of hops species  $X$  makes to a neighboring site

$$\Gamma = \nu \cdot p \quad (1-11)$$

Now, assuming two lattice planes separated by a distance  $a$ , with concentrations  $n_1$  and  $n_2$ , jump frequency of  $\frac{1}{2}\Gamma$  in each direction, during a small interval of time  $t$ , the atom  $X$  hops can be written as

$$\text{plane 1} \rightarrow \text{plane 2} \quad \frac{1}{2}\Gamma \cdot n_1 \cdot t \quad (1-12)$$

$$\text{plane 2} \rightarrow \text{plane 1} \quad \frac{1}{2}\Gamma \cdot n_2 \cdot t \quad (1-13)$$

thus resulting in the flux  $J$ , over an area  $A$ .

$$J = \frac{1}{2} \frac{\Gamma}{A} \cdot (n_1 - n_2) \quad (1-14)$$

If one expressed the above equation in terms of concentration  $c$ ,

$$c = \frac{n}{A \cdot a} \quad (1-15)$$

$$J = \frac{1}{2} \Gamma \cdot a (c_1 - c_2) \quad (1-16)$$

and applied it over the incremental distance  $\partial x$ , it gives the formula of the Fick's first law.

$$J = -\frac{1}{2} \Gamma \cdot a^2 \frac{\partial c}{\partial x} = -D \frac{\partial c}{\partial x} \quad (1-17)$$

Given the above equation, one can express the diffusivity as

$$D = g \cdot \Gamma \cdot a^2 = g \cdot \nu \cdot a^2 \cdot \exp\left(-\frac{\Delta G_X^m}{kT}\right) \quad (1-18)$$

with  $g$  as the geometric factor,  $g = \frac{1}{2}$  for one dimensional diffusion, and  $g = \frac{1}{6}$  for a three dimensional problem. The migration energy consists of enthalpy  $H$  and entropy  $S$ , as in the following equation

$$\Delta G_X^m = \Delta H_X^m - T \cdot \Delta S_X^m \quad (1-19)$$

Incorporating that into the diffusivity equation yields the final expression,

$$D = g \cdot \nu \cdot a^2 \cdot \exp\left(\frac{\Delta S_X^m}{k}\right) \cdot \exp\left(-\frac{\Delta H_X^m}{kT}\right) = D_{0X} \cdot \exp\left(-\frac{Q_X}{kT}\right) \quad (1-20)$$

with  $D_{0X}$  as the prefactor, and the  $Q_X$  as the activation energy.

The first Fick's law (derived above) describes the relation of flux with concentration, though it has no dependence on time. The second Fick's law defines the relationship of the concentration with time and position.

If a flux  $J_1$  entering the box is greater than the flux  $J_2$  exiting the box, the concentration in the box must increase in accord with the conservation of matter principle. The principle of Fick's second law is described in equations below

$$\frac{\partial c}{\partial t} = \frac{A \cdot J_1 - A \cdot J_2}{A \cdot \partial x} = \frac{J_1 - J_2}{\partial x} = -\frac{\partial J}{\partial x} \quad (1-21)$$

The number of dopants entering the box per unit time from the left is  $AJ_1$ , dopants leaving the box on the right is  $AJ_2$ , and their difference divided by the volume is equal to concentration per unit time. Using the equation from the first Fick's law, the equation governing the diffusion of dopant look like this in one dimension.

$$\frac{\partial c}{\partial t} = -\frac{\partial J}{\partial x} = -\frac{\partial}{\partial x} \left( -D \frac{\partial c}{\partial x} \right) = D \frac{\partial^2 c}{\partial x^2} \quad (1-22)$$

In three dimensions it yields a bit longer expression.

$$\frac{\partial c}{\partial t} = -\left(\frac{\partial J}{\partial x} + \frac{\partial J}{\partial y} + \frac{\partial J}{\partial z}\right) = -\nabla \cdot \mathbf{J} = \nabla \cdot (D\nabla c) = D\nabla \cdot (\nabla c) = D\nabla^2 c \quad (1-23)$$

$$\nabla^2 = \frac{\partial^2}{\partial x^2} + \frac{\partial^2}{\partial y^2} + \frac{\partial^2}{\partial z^2} \quad (1-24)$$

There are several conditions where the solution of Fick's laws provides general and frequently used solutions. In a limited source diffusion, assuming an instantaneous source depositing a fixed amount  $Q$  of impurity atoms on the surface of otherwise pristine silicon, the diffused profile would be in the form of

$$c(x, t) = \frac{Q}{\sqrt{\pi Dt}} \exp\left(-\frac{x^2}{4Dt}\right) \quad (1-25)$$

Another interesting case is diffusion from a constant source, similar to predeposition step, when impurities are introduced into silicon while maintaining constant surface concentration  $c_s$ . The constant surface concentration is generally maintained through abundant source, such as polysilicon or oxide doped above solid solubility at the predeposition temperature. The diffusing part of the dopant concentration would then be at the solid solubility. The solution of Fick's laws with these boundary conditions results in complementary error function,

$$c(x, t) = c_s \operatorname{erfc}\left(\frac{x}{2\sqrt{Dt}}\right) \quad (1-26)$$

A more common case in semiconductor processing is the combination of implant and anneal. Presuming a dose  $Q$  of a dopant was implanted with an energy  $E$ , with a mean projected depth  $R_p$  with vertical straggle  $\Delta R_p$ , the distribution after an implant would be

$$c(x) = \frac{Q}{\Delta R_p \sqrt{2\pi}} \exp\left(-\frac{(x-R_p)^2}{2\Delta R_p^2}\right) \quad (1-27)$$

Following anneal at temperature  $T$ , with diffusivity  $D$  for a time  $t$ , the distribution would be

$$c(x) = \frac{Q}{\sqrt{2\pi(\Delta R_p^2 + 2Dt)}} \exp\left(-\frac{(x-R_p)^2}{2\Delta R_p^2 + 4Dt}\right) \quad (1-28)$$

provided the profile was sufficiently far away from the surface, satisfying the following:

$$R_p^2 \gg 2\Delta R_p^2 + 4Dt \quad (1-29)$$

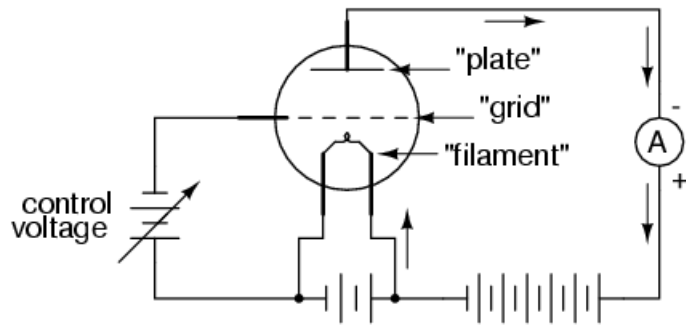


Figure 1-1. Triode electron tube schematic [Psi06]

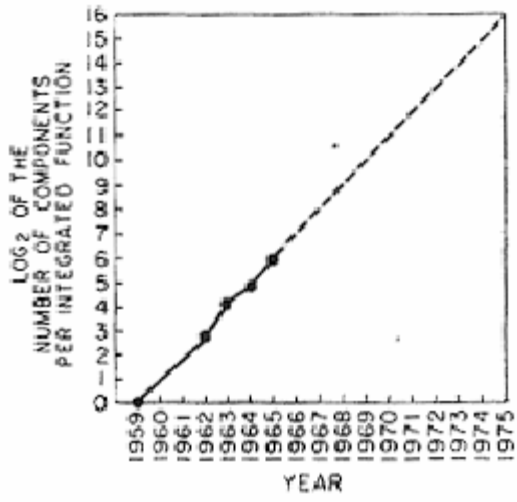


Figure 1-2. Number of components per integrated circuit vs. time, later known as “Moore’s law” [Moo65]

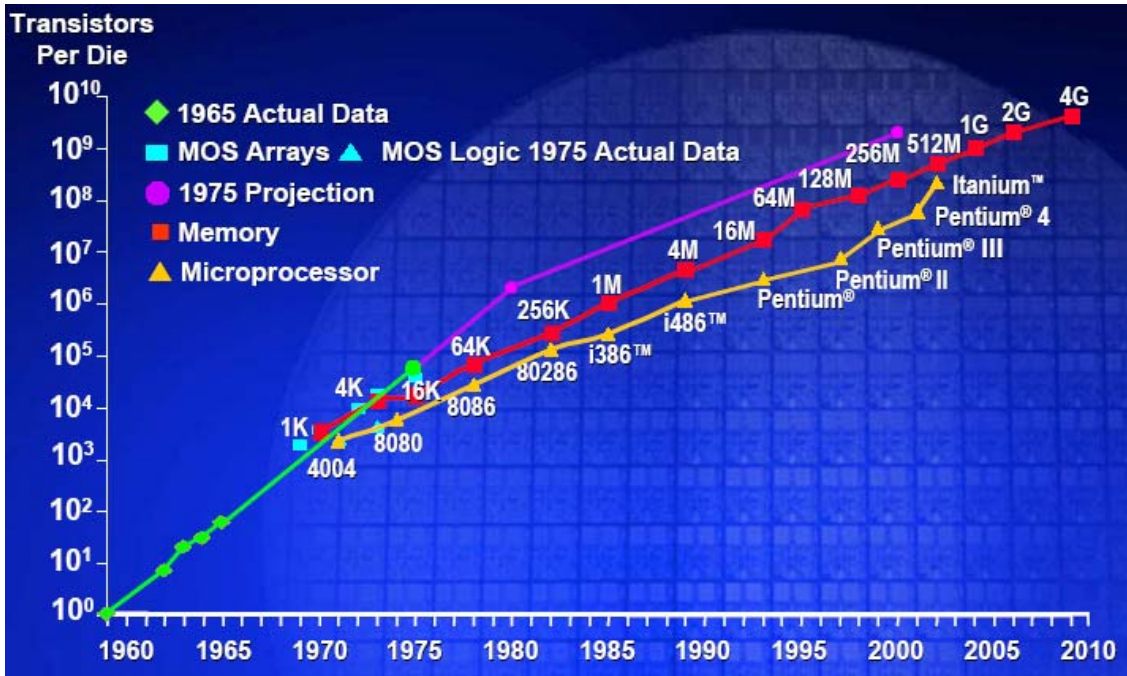


Figure 1-3. Number of transistors vs. time, shown to realize the original prediction of G. E. Moore, as well as updated trends [Moo03]

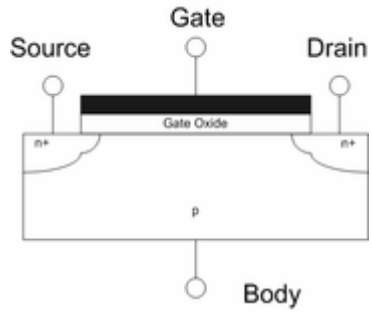


Figure 1-4 Schematic cross-section of a nMOSFET transistor

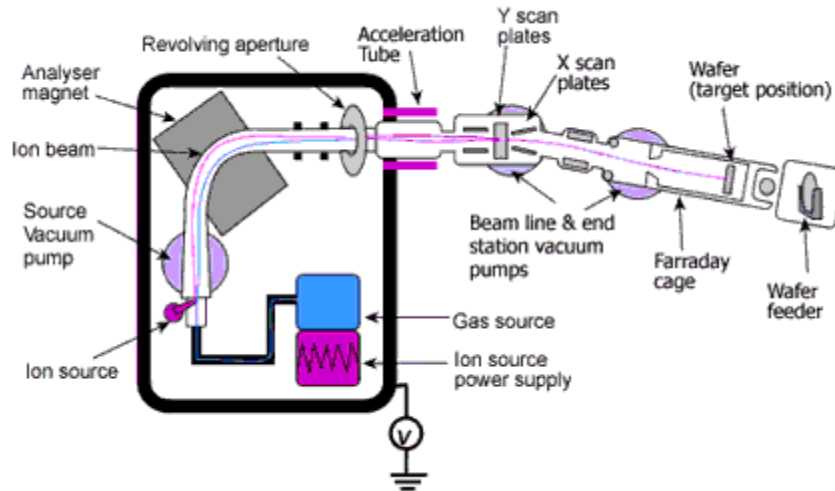


Figure 1-5. Schematic of an ion implanter [Imp06]

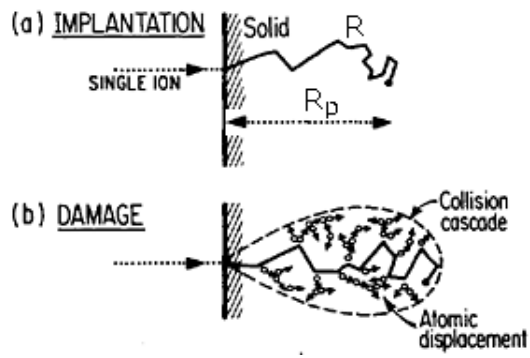


Figure 1-6. Illustration of an ion implantation process, in particular (a) a single ion path and (b) the resulting damage cascade [Wil84]

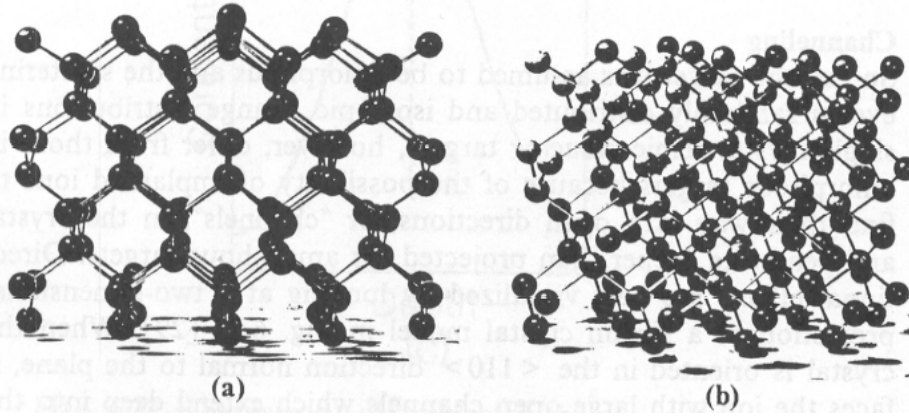


Figure 1.7 Silicon crystal viewed from (a)  $\langle 110 \rangle$  direction and (b) tilted  $\sim 10^\circ$  off the  $\langle 110 \rangle$  direction [May70]

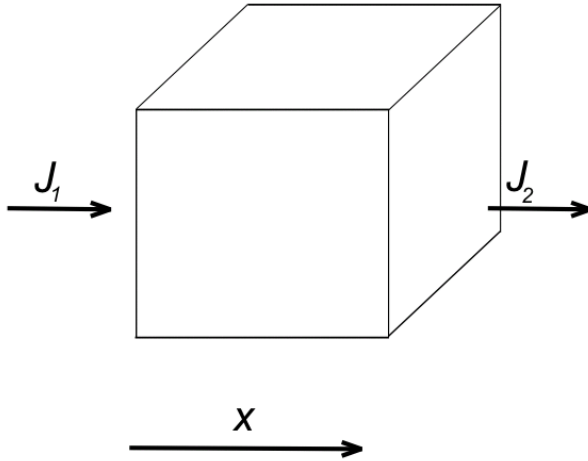


Figure 1.8. Illustration of fluxes entering and exiting a given volume

## CHAPTER 2 LITERATURE REVIEW

### **2.1 Dopant Diffusion in Silicon**

This section outlines some significant quantities influencing the diffusion of a given dopant species in silicon.

Diffusion in the silicon crystal, according to the standing theory [Fah89a], occurs through four mechanisms. Namely: interstitialcy and kick-out mechanism, which are interstitially mediated, vacancy mediated and concerted exchange. The former three require a point defect, an interstitial or a vacancy, respectively. Point defects interact with the dopant atom to form a dopant-defect pair. These pairs then diffuse by a random walk mechanism to generate net dopant diffusion. The kick-out mechanism involves an interstitial that does not form a pair with the dopant atom. Rather, the dopant atom is kicked out into the void, becomes an interstitial and diffuses through the channels in the crystal lattice. Eventually the dopant atom kicks out a silicon atom forming a silicon interstitial and occupies its lattice position. The fourth mechanism, concerted exchange, does not require point defect presence. Rather, it consists of two atoms, a dopant atom and a silicon atom, simultaneously exchanging positions. It is frequently neglected, as theoretical studies suggest the activation energy for concerted exchange would be prohibitively high [Nic89], compared to point defect mediated mechanisms. Recent experiments attempted to estimate the concerted exchange fractional contribution in diffusion [Ura99a]. The results of those experiments were somewhat ambiguous,

allowing for the existence of concerted exchange mechanism, but also allowing for its fraction contribution of zero. These four diffusion mechanisms are illustrated in Fig. 2-1.



$$E_{AX}^f = E_X^f - E_{AX}^b, \quad (2-2)$$

$$E_A = E_{AX}^f + E_{AX}^m = E_X^f - E_{AX}^b + E_{AX}^m, \quad (2-3)$$

Equation 2-1 describes the formation of a dopant-defect pair. The dopant is denoted as  $A$ , and the defect as  $X$ , which can be a silicon interstitial,  $I$  or a vacancy,  $V$ . Formation of a dopant-defect pair,  $AX$  leads to a lower energy state, as given in the Eq. 2-2.

Breaking of the pair requires a binding energy,  $E_{AX}^b$  which is provided by the lattice.

Motion of the pair occurs when a migration energy barrier,  $E_{AX}^m$  is overcome. Therefore, the dopant diffusion process via a point defect requires the formation of the defect, its reaction with a dopant atom in a substitutional site, to form a dopant-defect pair, which then migrates contributing to macroscopically observable diffusion behaviour. Activation energy for diffusion, in that case, can be written as a function of the formation energy of the defect  $X$ ,  $E_X^f$ , the binding energy of the dopant-defect pair  $AX$ ,  $E_{AX}^b$ , and the migration energy of a dopant defect pair  $AX$ ,  $E_{AX}^m$ , as shown in the Eq. 2-3. In single crystal silicon, those energies have fixed values. In  $\text{Si}_{1-x}\text{Ge}_x$  alloys, those values can vary with Ge content. For a complete picture, one should have information on both defect and dopant pair diffusion, with respect to Ge content. Also, Ge diffusion could be a function of Ge content, and should be investigated to allow simulation of spatially varying Ge profiles. The experimental data available in the literature will be discussed later in this chapter.

## 2.2 Self-diffusion in Silicon

Despite numerous theoretical and experimental studies on self-diffusion in silicon, contributions from interstitial and vacancy components are uncertain. Radioactive tracer technique results are limited by a 2.6 hour lifetime of  $^{31}\text{Si}$ , so monitoring heavy metal diffusion is frequently used in attempting to extract self-diffusion parameters. With the availability of the isotopically pure silicon sources, structures could be grown (by molecular beam epitaxy (MBE) or chemical vapor deposition (CVD)) with isotopically enriched or depleted layers. This approach requires no assumptions in measuring prefactors and activation energies for interstitial and vacancy diffusion.

The study of Bracht et al. [Bra98] measured self-diffusion of Si in an inert ambient. The samples were sealed in Ar filled capsules and annealed at temperatures ranging from 855°C to 1388°C. The extracted diffusivity  $D_{Si}$  (Eq. 2-4) contains both interstitial and vacancy diffusion components. Taking interstitial diffusivity measured in a Zn diffusion experiment [Bra95] as  $C_I^* D_I$  (Eq. 2-5), they extracted  $C_V^* D_V$  (Eq. 2-6).

$$D_{Si} = \left(530 \pm_{170}^{250}\right) \exp\left(-\frac{(4.75 \pm 0.04)eV}{k_B T}\right) [cm^2/s] \quad (2-4)$$

$$C_I^* D_I = 2980 \exp(-4.95eV/k_B T) [cm^2/s] \quad (2-5)$$

$$C_V^* D_V = 0.92 \exp(-4.14eV/k_B T) [cm^2/s] \quad (2-6)$$

Ural et al. [Ura98] performed a similar study measuring self-diffusion through diffusion of  $^{30}\text{Si}$  from naturally abundant, into isotopically depleted layers. The natural abundance of 3.1% was reduced to 0.002% in isotopically depleted layers. During the annealing, samples were subjected to inert, oxidizing and nitridizing ambient. Oxidizing ambient injects silicon interstitials [Hu74], while nitridizing ambient injects vacancies

[Fah85] from the surface. This perturbation of the point defect concentrations allows the extraction of the fractional interstitial,  $f_I$  and vacancy,  $f_V$  contributions to self-diffusion, without assumptions. Self-diffusivity measured in inert ambient was  $D_{Si}$  (Eq. 2-7), matching the values of Bracht et al. [Bra98]. Extracted  $f_I$  was in a range of 0.55-0.6( $\pm 0.1$ ), while interstitial and vacancy diffusivities were  $D_{SiI}$  (Eq. 2-8) and  $D_{SiV}$  (Eq. 2-9), respectively.

$$D_{Si} = 560 \exp(-4.76eV/k_B T) [cm^2/s] \quad (2-7)$$

$$D_{SiI} = 149 \exp(-4.68eV/k_B T) [cm^2/s] \quad (2-8)$$

$$D_{SiV} = 636 \exp(-4.86eV/k_B T) [cm^2/s] \quad (2-9)$$

### 2.3 Germanium Diffusion in $Si_{1-x}Ge_x$

Determining Ge diffusivity with respect to Ge content is interesting, particularly for a spatially varying Ge profile, such as base of a BJT or 2D hole gas (2DHG) transistors.

Zangenberg et al. [Zan01] measured Ge diffusion in  $Si_{1-x}Ge_x$  ( $x < 0.5$ ), MBE grown layers. Diffusion was measured using  $^{70}Ge$  as a tracer into  $^{72}Ge$  rich layers, during anneals at temperatures from 850 to 1050 °C. Transmission electron microscopy was used to confirm that the dislocation density was low enough not to influence diffusivity measurement. The diffusivities measured are shown in Fig. 2-5, with the extraction of prefactor and activation energies in Fig 2-6.

A more comprehensive study was performed by Strohm et al. [Str02]. Various material types used include MBE, CVD, Cz and FZ grown material, collected from a number of academic and industrial sources.  $^{31}Si$  and  $^{71}Ge$  isotopes were used as tracers, introduced into the material by ion implantation. Tracer dose below the threshold for formation of extended defects ensured negligible influence of implantation process.

Transient electron microscopy (TEM) and etch pit measurements verified that the dislocation density was under  $10^7$  cm<sup>-2</sup>. The samples were annealed at temperatures of 650 to 1250 °C in inert ambient. Their extracted prefactors and activation energies for Ge diffusion are shown in Fig. 2-7. Despite the difference in prefactors and activation energies, the diffusivities agree quite well to the values provided by Zangenberg, as shown in Fig. 2-8.

Large number of samples having different Ge concentrations provided a rather small stepping in Ge content. It is interesting that such variation of sources produced such a nicely behaving plot. A distinct change in the prefactor dependence with increasing Ge content occurs around 35% Ge, not as visible in the activation energy dependence. The authors attribute this to the change in the diffusion mechanism, from interstitial to vacancy dominated, as one increases Ge content.

The situation is not as clear when it comes to fractional interstitial and vacancy contributions to Ge diffusion. Initial studies of Fahey et al. [Fah89b] estimated  $f_i$  and  $f_v$  using ammonia ambient anneals. Ammonia (NH<sub>3</sub>) annealing ambient, reacting with a bare silicon surface, injects vacancies into the bulk [Fah85][Kri96][Kri97][Mog96]. The same ambient, reacting with oxide (SiO<sub>2</sub>) injects interstitials. Reference was provided by a sample coated in oxide and nitride, ensuring no surface reaction, and no point defect injection. Samples contained a Ge marker layer grown by MBE. Peak Ge concentration was ~5%. Anneals conducted under vacancy and interstitial injection both diffused the Ge profile more than the reference sample. At a temperature of 1050°C, they estimated  $f_i = 0.3-0.4$ . Unfortunately, data for other temperatures was not provided.

Studies of Griglione et al. [Gri00, Gri01] concentrated on extraction of  $f_I$  and  $f_V$  by annealing  $\text{Si}_{0.85}\text{Ge}_{0.15}$  layers in inert and oxidizing ambient at temperatures ranging from 900 to 1200 °C. Diffusion of buried B marker layer was monitored to verify the oxidizing reaction on the surface injected interstitials and estimate interstitial diffusivity enhancement. The enhanced diffusion of the buried B marker layer also showed that the  $\text{Si}_{0.85}\text{Ge}_{0.15}$  layer does not significantly perturb interstitial population, meaning there was no pile-up of silicon interstitials in GeI pair. Since the oxidizing ambient resulted in reduced diffusion (Fig 2-9.) of Ge from the  $\text{Si}_{0.85}\text{Ge}_{0.15}$  layer, it was inferred that the diffusion was vacancy mediated. To verify this, anneals in nitridizing ambient were performed at temperatures of 1100 and 1200 °C. Instead of the expected increase in diffusivity, a considerable reduction in diffusivity was observed, thus making it difficult to draw a firm conclusion on the available data.

## 2.4 Boron Diffusion in Silicon

### 2.4.1 Boron as Interstitial Diffuser in Silicon

Boron is generally accepted to be an interstitially diffusing species [See68][Fah85][Fan96][Gos97]. More recent measurements [Ura99b] of B diffusion in interstitial and vacancy supersaturation, gave  $f_I$  values higher than 0.84, assuming the vacancy concentration was unperturbed. A more strict assumption on the recombination of equilibrium point defects  $\frac{C_I^{eq}}{C_I^{ox}} \leq \frac{C_V^{ox}}{C_V^{eq}} \leq 1, \frac{C_V^{eq}}{C_V^{nit}} \leq \frac{C_I^{nit}}{C_I^{eq}} \leq 1$  yields  $f_I$  values above 0.94.

The exact mechanism of B microscopic diffusion is not certain, between interstitial pair diffusion and kick-out mechanism. Recent ab-initio calculations [Win99] suggest B diffusion is mediated by a BI pair. The pair binding energy was calculated to be 0.8eV, while the migration energy was 0.2 eV. According to the Eq. 2.5, the activation energy

for B diffusion would also depend on the formation energy of an interstitial. Since the values of point defect formation and migration energies used in FLOOPS are somewhat different than the ones used in this study, a free parameter is necessary to match the macroscopically observed activation energy. In this case, the binding energy of a BI pair is used as a free parameter. The value of 0.5 eV was used to match the B diffusivity values of FLOOPS defaults.

#### **2.4.2 Pre-amorphization and B**

B implants into crystalline silicon material seldom provide the optimal results, due to channeling, solid solubility limit and the deactivation to form boron-interstitial clusters (BICs). Low energy implants require implantation in deceleration mode in order to provide viable implant currents. Even then, there is a possibility of energy contamination due to the neutralization of the charged species before reaching the decelerating stage. Once the B ion enters the silicon lattice, a certain portion of the implanted dose channels, increasing the *pn* junction depth. Increasing the dose to reduce the parasitic resistances can result in BIC formation, thus decreasing active B concentration below solid solubility limit.

Some of these detrimental effects can be mitigated by pre-amorphizing the silicon crystal. The disordered structure of the amorphous silicon prevents channeling [Zie00b], thus reducing the *pn* junction depth. Activation can also benefit from the preamorphization, as the amorphous layers can be regrown at low temperatures (450-600°C) incorporating dopant concentrations higher than solid solubility at the regrowth temperature. The spatial separation of the end of range (EOR) damage and the dopant suppresses the formation of BICs [Jon96a]. Germanium is the popular choice of

amorphizing implant species due to producing less damage than the silicon implant for the same implant dose [Cla02].

## 2.5 Boron-interstitial Clusters

Dopants are mostly introduced into a Si wafer via implantation process, which is followed by an annealing process. During the thermal process, the damaged crystalline lattice is repaired and the dopants fall into the substitutional positions, thus becoming electrically active.

However, the annealing process following a B implant under certain conditions, such as yielding a peak concentration above  $1 \times 10^{19} \text{ cm}^{-3}$ , does not activate all the dopants. The implanted profile splits into two regions, the immobile peak and the rapidly diffusing tail, as first observed by Michel et al. [Mic87]. The immobile portion of the profile is particularly interesting as it is at a concentration much lower than the solid solubility of B in Si, above  $4 \times 10^{19} \text{ cm}^{-3}$  for temperatures over  $800^\circ\text{C}$  [Vic69]. In the comparison between the annealed profiles at 800 and  $950^\circ\text{C}$ , immobile peak is far more pronounced at the lower temperature (Fig. 2-10). The same is the case with the diffusion in the tail regions, as the transient enhanced diffusion (TED) is reverse activated, having higher diffusion enhancement at lower temperatures.

Stolk et al. [Sto95] investigated the formation of the immobile peak portion, by implanting Si into a wafer containing B  $\delta$ -doped layers. The Si  $5 \times 10^{13} \text{ cm}^{-2}$  implant at 40 keV contained the damage into the top  $0.1 \mu\text{m}$  layer, directly affecting only the B layer marked as 1 (Fig. 2-11). The annealed B profiles show several interesting characteristics. First and second  $\delta$ -doped layers have significantly diffused tails, indicating the interstitial supersaturation as expected after a Si implant and consequential TED. But, these  $\delta$ -doped

layers also have immobile peaks, indicating that the majority of B in them is inactive. The shouldering concentration (the intersection of the immobile peak and the diffused tail) of the 1<sup>st</sup> and 2<sup>nd</sup>  $\delta$ -doped layer is significantly lower than B solid solubility at the anneal temperature, indicating that some mechanism other than the solubility limit is preventing B diffusion. The 3<sup>rd</sup>  $\delta$ -doped layer exhibits lower diffusion enhancement than the first two, but it does not have a visible immobile portion. All the other  $\delta$ -doped layers diffuse closer to the equilibrium diffusivities.

This experiment shows that the interaction between self-interstitials and substitutional B can form immobile peaks. Furthermore, it shows the excess interstitials from the implant damage can diffuse and interact with substitutional B forming metastable clusters visible as immobile B peaks after an anneal. As these clusters are the product of the interaction of self-interstitials and boron, thus called boron-interstitial clusters.

To probe the dissolution kinetics of BICs, Lilak et al. [Lil02] used thirteen B implant conditions. The samples were annealed at 750°C for 30 minutes in order to deactivate the majority of the B dose. Then, the samples were followed through a number of times during anneals at 750 or 850 °C, using the Hall effect measurement and spreading resistance profiling (SRP) to measure activation. Some measurements are shown in the figure 2-12. These measurements indicate that the increase in dose with constant implant energy, as well as the decreasing implant energy with constant dose, decrease the activation upon annealing at temperatures  $\sim$ 750°C. Another important parameter, the energy required for the reactivation of B was extracted from these measurements to a value around 3eV.

A similar experiment was done by Mirabella et al. [Mir03], using the MBE grown B marker layers. The shallowest marker layer was used to monitor the clustering process, while the deeper marker layers were used to monitor the interstitial supersaturation. These samples were implanted with  $5 \times 10^{13} \text{ cm}^{-2}$  Si at 20keV, providing the excess interstitials for the clustering process. The active dose was measured after several anneals with temperatures in the range from 815 to 950 °C, and compared to the as-grown dose of  $3 \times 10^{13} \text{ cm}^{-2}$ . The methodology was different than the one used in Lilak et al., as the active dose was extrapolated from SIMS measurement. It was assumed the diffusing tails form a Gaussian distribution within the entire profile, and representative of the active fraction of the B profile (Fig. 2-13). Such an indirect approach eliminates the possibility of measuring electrically partially active clusters, rather measuring the substitutional B concentration through its availability to partake in a diffusion process.

Having determined the active fraction in a number of anneals, they extracted the activation energy for reactivation as  $3.2 \pm 0.4 \text{ eV}$ , in agreement with the previous measurement of Lilak et al. The B clustered doses and time constants used in the extraction are shown in figure 2-14.

## 2.6 Boron Diffusion in $\text{Si}_{1-x}\text{Ge}_x$

There are several reports [Kuo93][Kuo95a][Zan01] on the reduction of B diffusion in  $\text{Si}_{1-x}\text{Ge}_x$  compared to Si. The first report of reduced B diffusivity in  $\text{Si}_{1-x}\text{Ge}_x$  was by Kuo et al. [Kuo93]. The structure used in the measurement is shown the Fig. 2-15.

The layers were grown on  $\langle 100 \rangle$  n-type Czochralski Si wafers in a CVD process. Initially, a layer of undoped Si was deposited. On top of that a 60 nm thick  $\text{Si}_{0.83}\text{Ge}_{0.17}$  layer, in-situ doped with B concentrations from  $10^{18}$  to  $3 \times 10^{19} \text{ cm}^{-3}$  in the center 20 nm.

A silicon capping layer of 60 nm was deposited to enhance the stability of the  $\text{Si}_{0.83}\text{Ge}_{0.17}$  layer. Control samples contained only the B layer. Secondary ion mass spectrometry (SIMS) was used to extract dopant profiles. Initial profiles, as well as profiles after a 30 minute anneal at  $860^\circ\text{C}$  in nitrogen ambient, are shown in Fig. 2-16.

At the top of Fig. 2-16 profiles for boron in the sample without the Ge layer can be seen, while the plot at the bottom indicates a B layer contained in 17% Ge layer. Square symbols are used to plot the as-grown profiles, while the plus (+) symbol demonstrates the annealed profiles. The extracted diffusivity was found to be approximately an order of magnitude lower in  $\text{Si}_{1-x}\text{Ge}_x$  sample, as shown in the Fig. 2-17.

Moriya et al. [Mor93] also report on the reduction of B diffusivity in  $\text{Si}_{1-x}\text{Ge}_x$  layers. In one experiment, 15 nm  $\text{Si}_{0.7}\text{Ge}_{0.3}$  layers were grown by rapid thermal chemical vapor deposition (RTCVD), within which a B peak concentration of  $8 \times 10^{19} \text{ cm}^{-3}$  was introduced in the middle 5 nm of the  $\text{Si}_{0.7}\text{Ge}_{0.3}$  layer. Ge rich layer was grown on a Si buffer layer and capped with Si layer, all containing a background B concentration of  $10^{18} \text{ cm}^{-3}$  to avoid electric field effect influence on diffusion. Si control samples only differed in the fact they contained no Ge. The samples were annealed in a rapid thermal annealing system (RTA) at temperatures from  $850^\circ\text{C}$  to  $1000^\circ\text{C}$ , in an inert ambient. The Si control showed no significant deviation from the accepted values for diffusivity of B, thus verifying no anomalous material effects were present. This was not the case for B diffusion in  $\text{Si}_{0.7}\text{Ge}_{0.3}$  layer. The diffusivity of B in  $\text{Si}_{0.7}\text{Ge}_{0.3}$  layer was significantly lower than the control, as shown in Fig. 2-18. Activation energy extracted was about 1 eV higher than the accepted values for B diffusion in Si.

A separate experiment in the same publication [Mor93] tried to measure B diffusion as a function of Ge content (10%-50%). The multilayer structure was grown MBE and annealed at 975°C for 30 seconds. As Fig. 2-19. shows, increase in the Ge content reduces B diffusivity.

Another experiment by Kuo et al. [Kuo95a] attempts to isolate the strain influence on diffusion. As Ge has 4.2% larger lattice constant than Si, it introduces a strain into the lattice. Separating the influence of strain from the Ge content was achieved using the structure shown in Fig. 2-20. First, a graded buffer layer was grown on <100> p-type Si wafer was grown. The buffer layer contained linearly increasing Ge content, serving to relax the strain with a minimum of threading dislocations. Second, a 0.25 $\mu$ m relaxed Si<sub>1-y</sub>Ge<sub>y</sub> layer was grown to serve as a substrate for a pseudomorphic diffusion structures. Third, pseudomorphic 60 nm thick Si<sub>1-x</sub>Ge<sub>x</sub> layer was grown, containing a 20 nm B layer. Fourth and last, the capping 40 nm Si<sub>1-y</sub>Ge<sub>y</sub> layer was grown to ensure thermal stability.

Having an independent control over  $x$ ,  $y$  Ge contents, one can engineer the strain for a given  $x$  percent Ge. In order to investigate the dependence of diffusion irrespective of strain,  $x$  has to be equal to  $y$ . Another application could be to investigate the diffusion as a function of Ge content, with a constant strain. That can be accomplished for  $x=y+z$ , where  $z$  is any Ge content delivering the desired strain. Some of these combinations are shown in the Fig. 2-21.

There are several things to note. First, diffusivity around 0% strain is a function of Ge content. Second, strain dependence for 10% and 20% Ge is rather weak, indicating that the strain is not the dominant component in reduction of B diffusivity with increasing Ge content. Rather, it would seem the chemical effect of Ge is more significant. It is

interesting that the Ge presence reduces the B diffusivity, particularly since the self-diffusion of Ge and Si increase with Ge content in  $\text{Si}_{1-x}\text{Ge}_x$  alloys [Str02]. Presuming that B diffusion remains interstitially mediated in  $\text{Si}_{1-x}\text{Ge}_x$  (confirmed for 10% [Wil01] and 18% Ge [Kuo95b]), and that the properties of the BI pair remain unchanged with Ge content, the increase in self-diffusion should increase the effective B diffusivity.

Similar structure (Fig. 2-22) to that of Kuo et al. [Kuo95a] was used in an experiment of Zangenberg et al. [Zan03] to investigate the diffusion of B and P in MBE grown  $\text{Si}_{1-x}\text{Ge}_x$ . The  $\text{Si}_{1-x}\text{Ge}_x$  layers were grown on the (100) Czochralski Si wafers, using the graded buffer layer to prevent the dislocation growth towards the surface. TEM verified that samples before and after annealing had dislocation density under  $10^6 \text{ cm}^{-2}$ , and that no dislocations formed at the pseudomorphic layer interfaces, confirming that dislocations had minimal influence on dopant diffusion. The samples used in the study of B diffusion were annealed at temperatures between 800 and 925 °C, with Ge contents of 0%, 1%, 12%, and 24%.

The experimental results were quite unexpected. Despite the previous body of literature on reduction of B diffusion in  $\text{Si}_{1-x}\text{Ge}_x$  alloys, the study found a small difference between B diffusion in relaxed  $\text{Si}_{1-x}\text{Ge}_x$  and the control samples. The extracted parameters for B diffusion in relaxed  $\text{Si}_{1-x}\text{Ge}_x$  are shown in Table 2-1. Even though the measured control diffusivities fit the certain measured values for B diffusion in Si in that temperature range, the extracted activation energy of 2.68 eV is quite different from the values of Fair (3.46 eV) [Fai81] or Haddara et al. (3.75 eV) [Had00].

The other interesting point in this measurement is the change of the B activation energy with increasing Ge content. The addition of 1% Ge in the relaxed  $\text{Si}_{1-x}\text{Ge}_x$  alloy

increases the activation energy of diffusion by  $\sim 0.5\text{eV}$ , which does not change significantly in higher Ge contents, as demonstrated in  $\text{Si}_{0.88}\text{Ge}_{0.12}$  and  $\text{Si}_{0.76}\text{Ge}_{0.24}$ . These values would suggest, provided the properties of the BI pair and self-interstitial diffusion were unchanged by Ge content, that the addition of Ge adds another potential well of about  $0.5\text{eV}$  to the B diffusion mechanism.

Having reviewed all of these experimental data of B diffusion in  $\text{Si}_{1-x}\text{Ge}_x$ , one can notice there is no clean study of B diffusion with a number of samples over various temperatures, like Strohm et al. [Str02] for Ge self-diffusion. The closest to the detailed measurement of B diffusion in relaxed  $\text{Si}_{1-x}\text{Ge}_x$  is the experiment of Zangenberg et al. [Zan03] with a temperature range of  $125^\circ\text{C}$  and a problematic control. Most studies concentrated on one temperature, or one time, or one Ge content.

### 2.7 Modeling Boron Diffusion in $\text{Si}_{1-x}\text{Ge}_x$

The first B diffusion model to be discussed was published by Lever et al [Lev98]. In their experiment B layer was sandwiched between two Ge layers, both of 10% or 3% Ge content. One set of Lever's samples was grown via low pressure CVD (LPCVD) on  $\langle 100 \rangle$  FZ silicon wafers. They used B wells with concentrations of  $3 \times 10^{18}$ ,  $6 \times 10^{18}$ , and  $1.5 \times 10^{19} \text{ cm}^{-3}$ . Initially, a 100 nm thick silicon buffer layer was grown on a wafer. It was followed by growth of undoped 40 nm thick  $\text{Si}_{0.9}\text{Ge}_{0.1}$  layer, a 250 nm thick B well, another 40 nm, and finally capped with 100 nm undoped Si. In another set of Lever's samples, a silicon buffer layer was grown on a Czochralski silicon wafer. It was followed by a 80 nm thick undoped  $\text{Si}_{0.97}\text{Ge}_{0.03}$  layer, 200 nm thick B well with concentration of  $10^{19}$  or  $4 \times 10^{19} \text{ cm}^{-3}$ , another 80 nm  $\text{Si}_{0.97}\text{Ge}_{0.03}$  layer, and capped with a silicon layer. All samples were capped with 40 nm  $\text{SiO}_2$  and 160 nm  $\text{Si}_3\text{N}_4$ , to ensure the inert surface

condition. Anneals were performed at 850°C for times of 4, 24 or 96 hours. Fig. 2-23 shows some of the resulting profiles.

In their simulations, Lever et al. considered B diffusion as perturbed by Ge content. This simplification disregards possibility that B activation depends on Ge content. Influence of strain was also neglected, as study by Kuo et al [Kuo95a] showed it to be small. Change in bandgap was considered to be linear with Ge content. Vacancy mediated diffusion of B was also neglected, which also limits this model to lower Ge content. Higher Ge content might have significant vacancy self-diffusion component, which could influence B diffusion, as well as  $f_I$ .

The B flux equation (Eq. 2-10) consists of three terms. The first term is Fick's law term for diffusion of boron, denoted as  $C_B$ . Second term is impurity related electric field diffusivity enhancement. Third term is result of energy bandgap variation due to Ge content. Diffusivity is described as sum diffusivity coming from interaction with neutral,  $D_1$  and ionized,  $D_2$  point defects (Eq 2-11), with factor beta as ratio of those two. The last equation (Eq 2-12) is the Arrhenius expression for diffusivity as a function of temperature.

$$J_B = -D_B^0 \Psi \left( \frac{\partial c_B}{\partial x} + \frac{c_B}{n+p} \frac{\partial (N_A - N_D)}{\partial x} + \frac{2c_B n}{n+p} \frac{\partial \ln(n_i)}{\partial x} \right) \quad (2-10)$$

$$D_B^0 \Psi = D_1 + D_2 \frac{p}{n_i} = (D_1 + D_2) \left( \frac{1 + \beta \frac{p}{n_i}}{1 + \beta} \right), \beta = \frac{D_2}{D_1} \quad (2-11)$$

$$D_B^0 = k \cdot \exp\left(-\frac{3.5}{kT}\right) \quad (2-12)$$

$$\frac{C_B}{C_{B\_act}} = 1 + \frac{C_{Ge}}{s} \Rightarrow C_{B\_act} = C_B \frac{s}{s + C_{Ge}} \quad (2-13)$$

The pairing between Ge and B is assumed to form a GeB cluster, immobile, but electrically active. The rest of B is available for diffusion ( $C_{B\_act}$ ), as described by Eq. 2-13. The fitting parameters of the model are  $b$ ,  $k$  and  $s$ . Although the parameters have been individually fitted for each annealing condition, they do not vary significantly. The good features of this model include: simplicity, few parameters, and good fit to several Ge contents with the same value of  $s$ . This model has been implemented in FLOOPS, and used as an initial guess in experiment design.

Table 2-1. Extracted B diffusivity prefactor ( $D_0$ ) and activation energy ( $E^a$ ) from experiment of Zangenberg et al. [Zan03]

Ge [%]	Temp range [°C]	$D_0$ [cm <sup>2</sup> /s]	$E^a$ [eV]
0	800-900	$3.4(2.3) \times 10^{-4}$	2.68(7)
1	800-925	$3.4(2.0) \times 10^{-2}$	3.13(6)
12	800-925	$2.4(2.4) \times 10^{-1}$	3.30(10)
24	800-925	$5.7(7.0) \times 10^{-2}$	3.18(13)

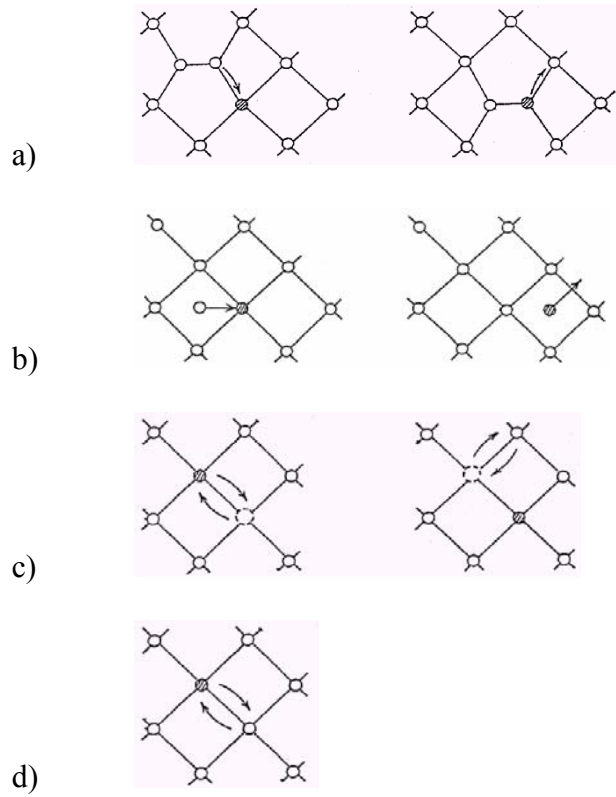


Figure 2-1. Diffusion mechanisms in silicon: a) interstitialcy diffusion, b) kick-out, c) vacancy diffusion, and d) concerted exchange [Fah89a]

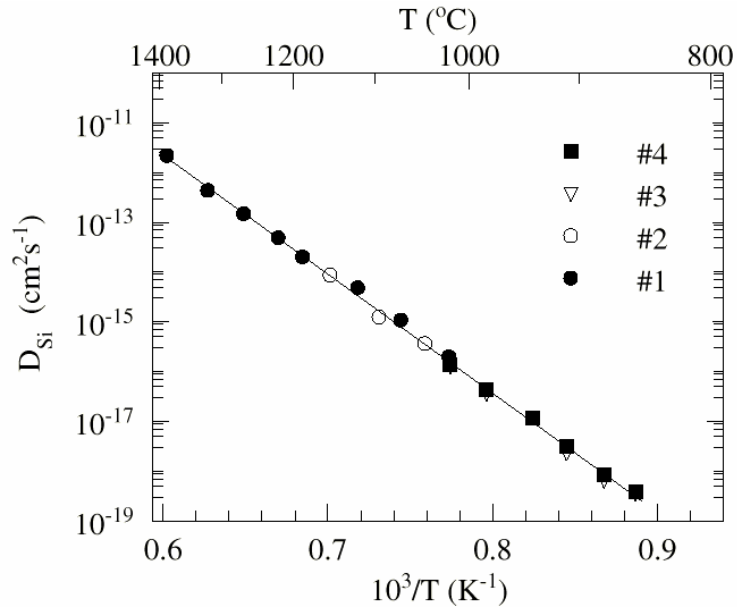


Figure 2-2. Self-diffusion in Si as measured by Bracht [Bra98], with symbols denoting different samples

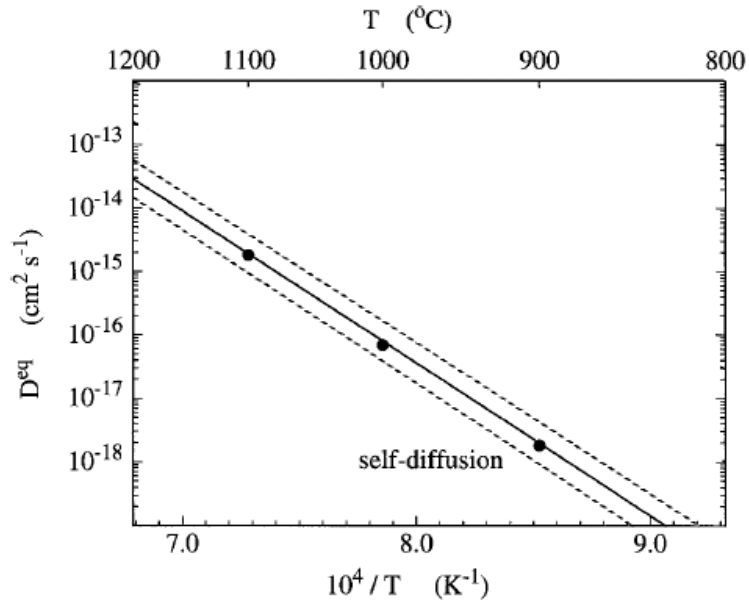


Figure 2-3. Self-diffusion in Si as measured by Ural et al. [Ura99b]. Dots represent measured diffusivities, solid line is the best fit expression for self-diffusion. Dashed lines represent bounds of self-diffusion as reported by Bracht [Bra98], showing good agreement between measurements.

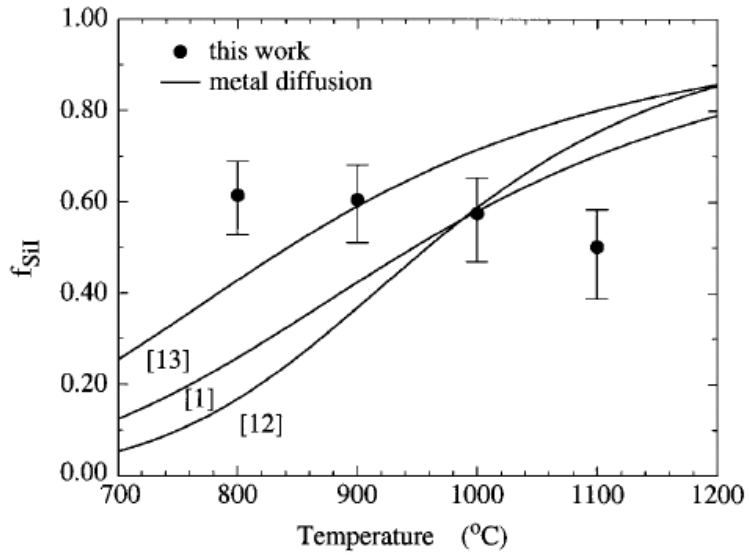


Figure 2-4. Interstitial fraction,  $f_{SiI}$  of the self-diffusion from Ural et al. [Ura99b]. The lines represent predictions from several metal diffusion experiments.

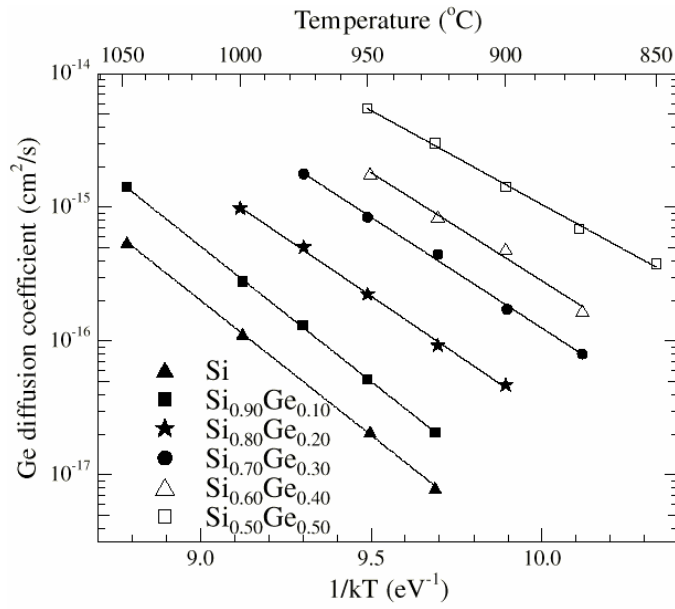


Figure 2-5. Germanium diffusivities for various temperatures and Ge contents, after Zangenberg et al [Zan01]

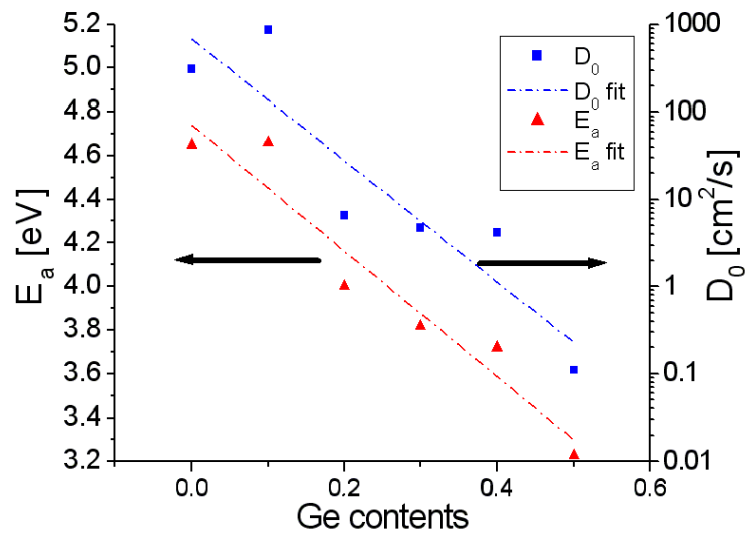


Figure 2-6. Activation energies and prefactors for various Ge contents, after Zangenberg

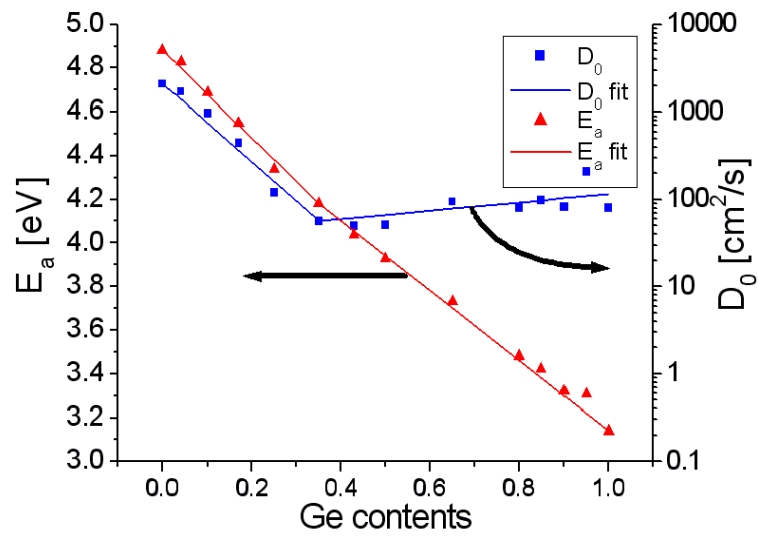


Figure 2-7. Activation energies and prefactors for various Ge contents, after Strohm

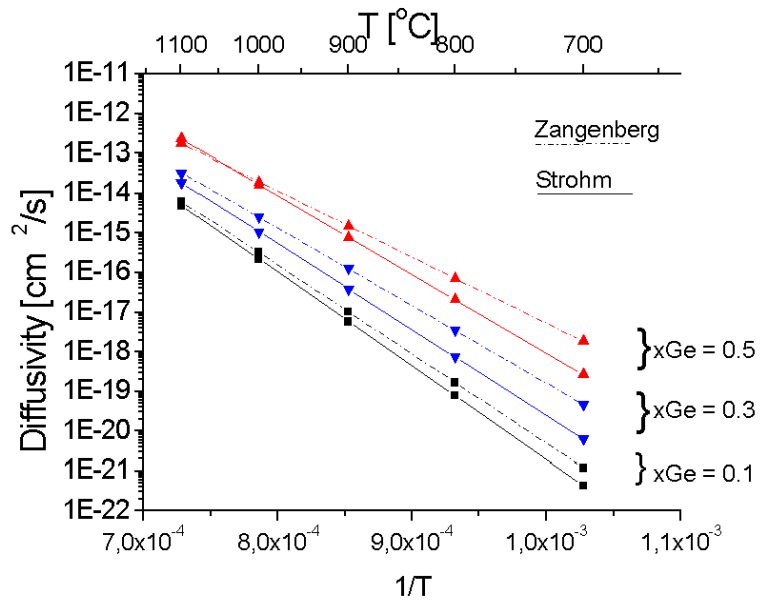


Figure 2-8. Comparing diffusivities of Ge in  $\text{Si}_{1-x}\text{Ge}_x$  as measured by Zangenberg and Strohm

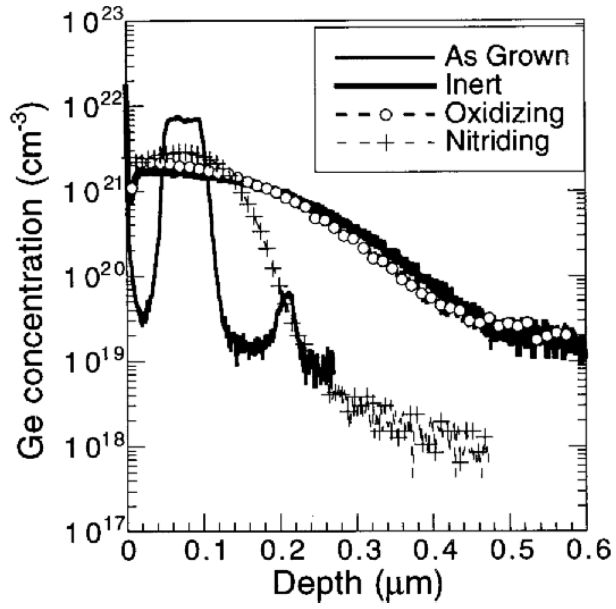
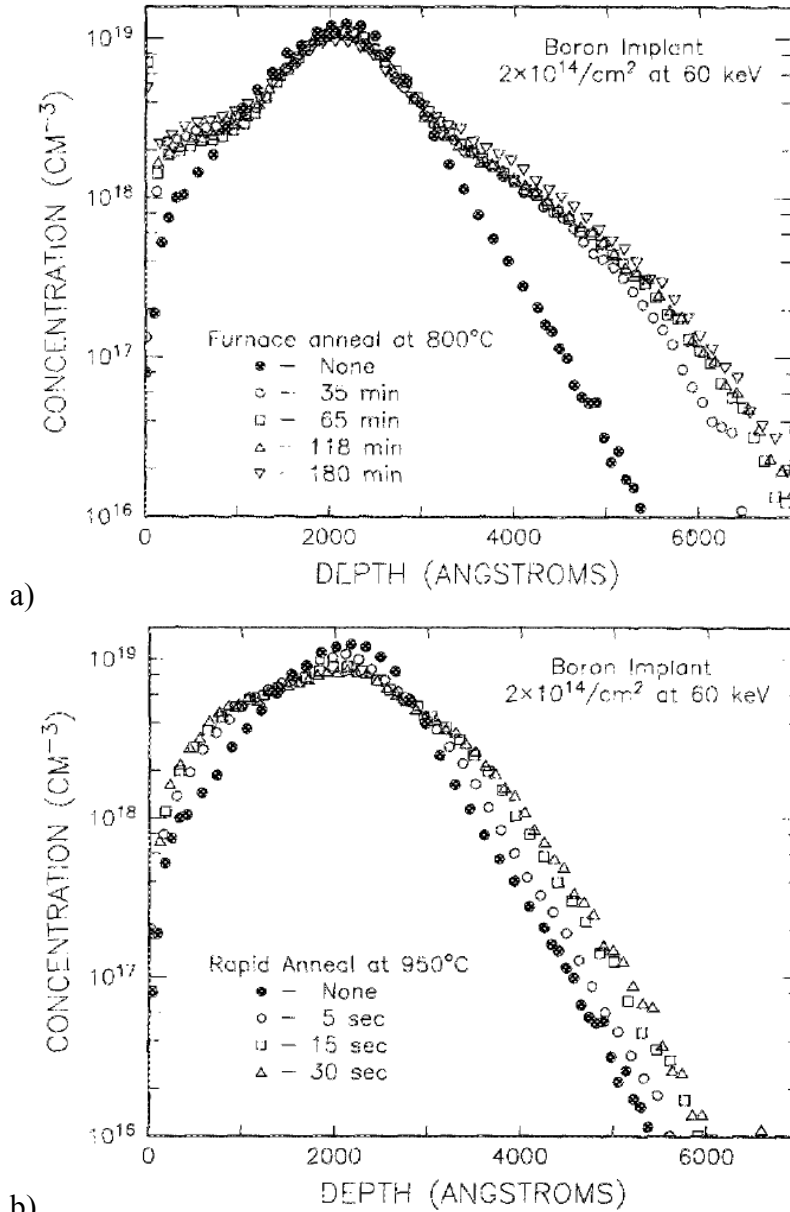


Figure 2-9. Comparison of Ge diffusion with respect to ambient and consequential interstitial or vacancy supersaturation [Gri01]



b) Figure 2-10. B profiles after an implant of  $2 \times 10^{14}$  at 60keV, annealed at a) 800°C and b) 950°C [Mic87]

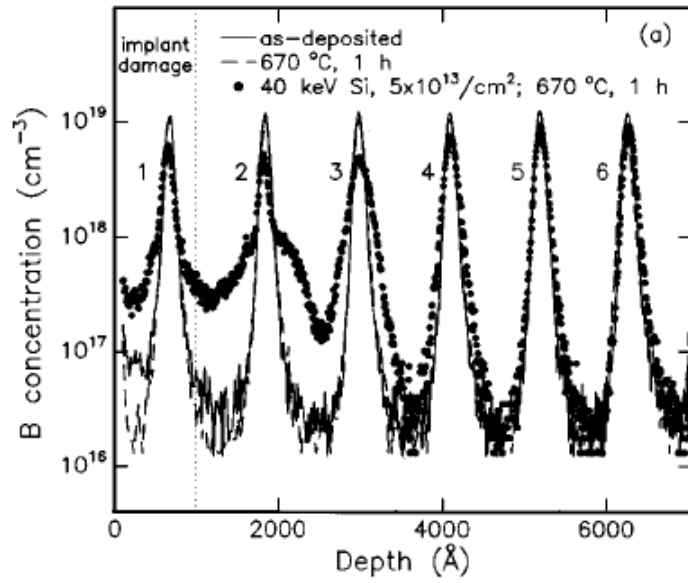
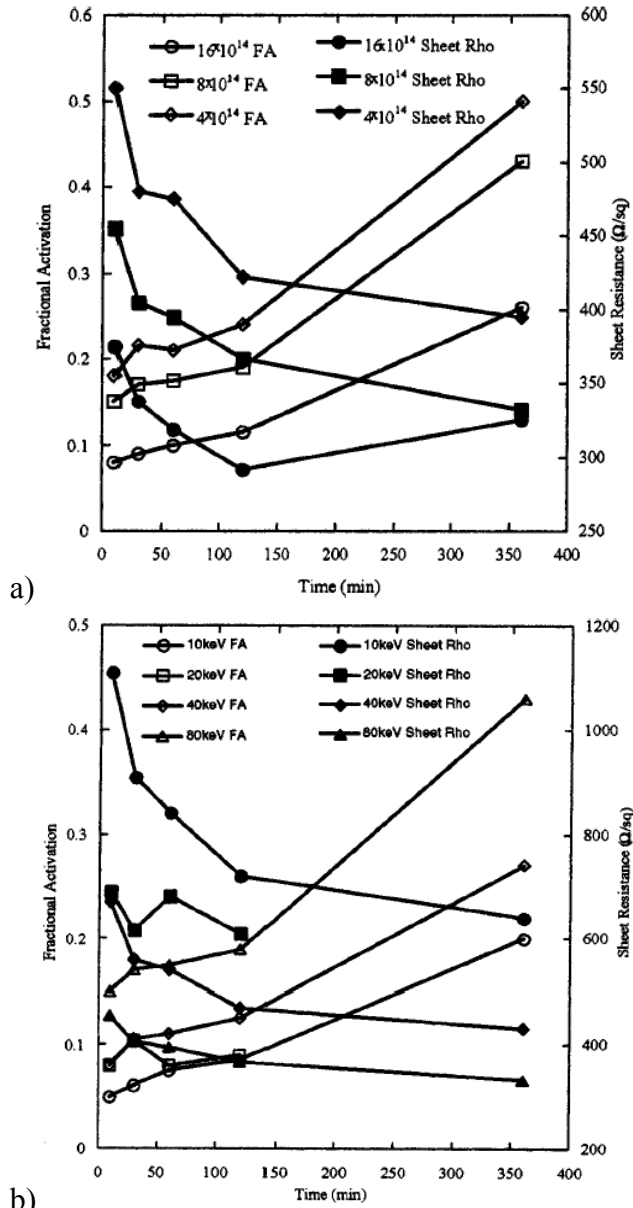


Figure 2-11. B profiles, as-grown and after 1h at 670 $^{\circ}\text{C}$  [Sto95]



b) Figure 2-12. Fractional activation and sheet resistance of samples annealed at 750°C for:  
 a) varying B dose at 80keV, and b)  $4 \times 10^{14} \text{ cm}^{-2}$  at varying energy [Lil02]

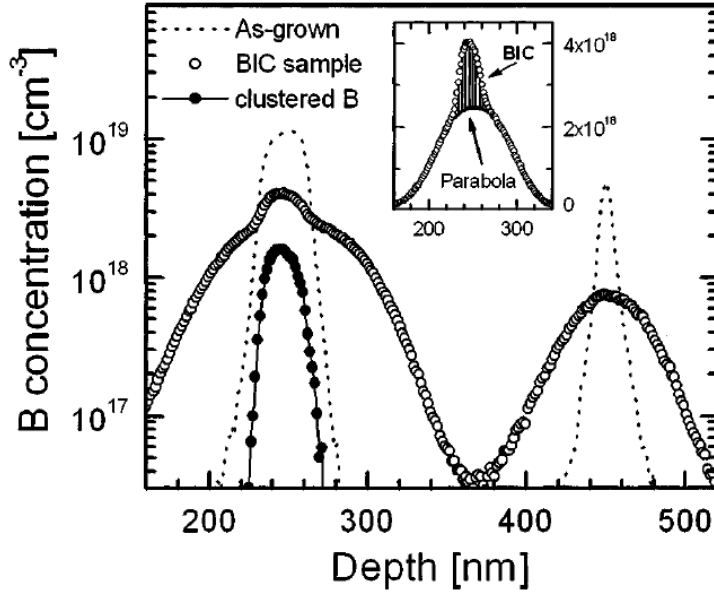


Figure 2-13. B profiles used in experiment by Mirabella et al. showing the as-grown, annealed for 2 min at 815°C, as well as illustrating the methodology for determining the active fraction [Mir03]

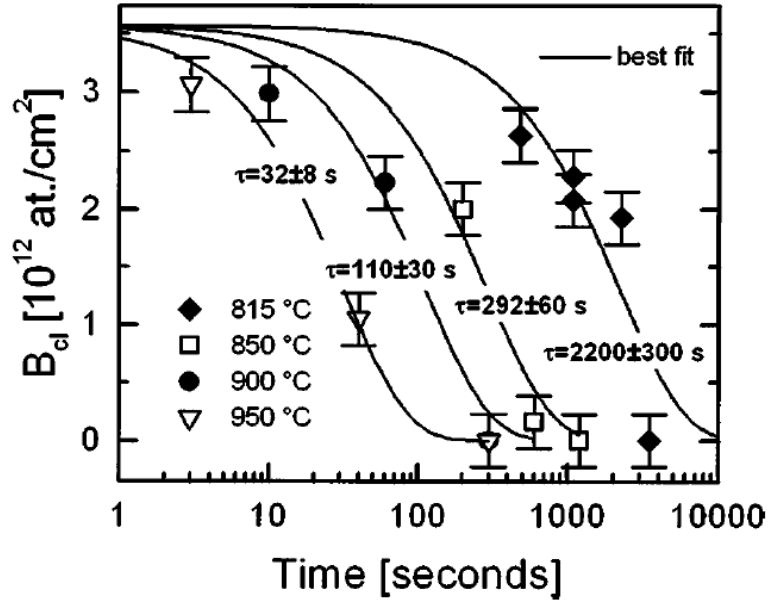


Figure 2-14. Time evolution of the clustered B dose during annealing at 815 to 950 °C, with extracted time constants. [Mir03]

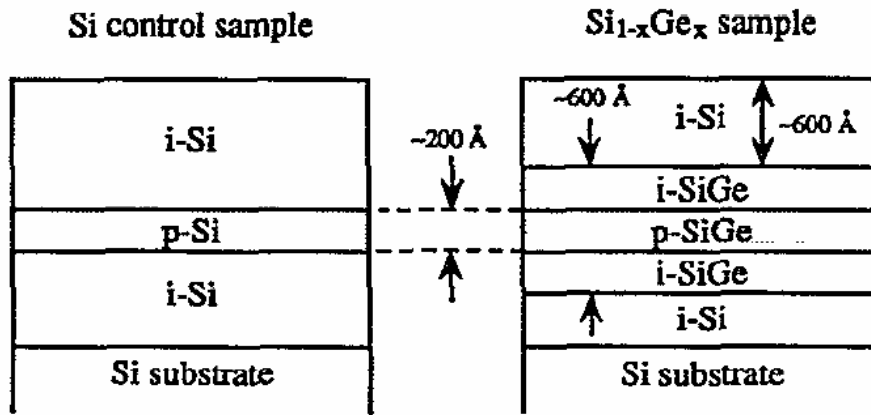


Figure 2-15. Structure used by Kuo et al. [Kuo93] with a B marker layer in the  $\text{Si}_{0.83}\text{Ge}_{0.17}$  strained layer

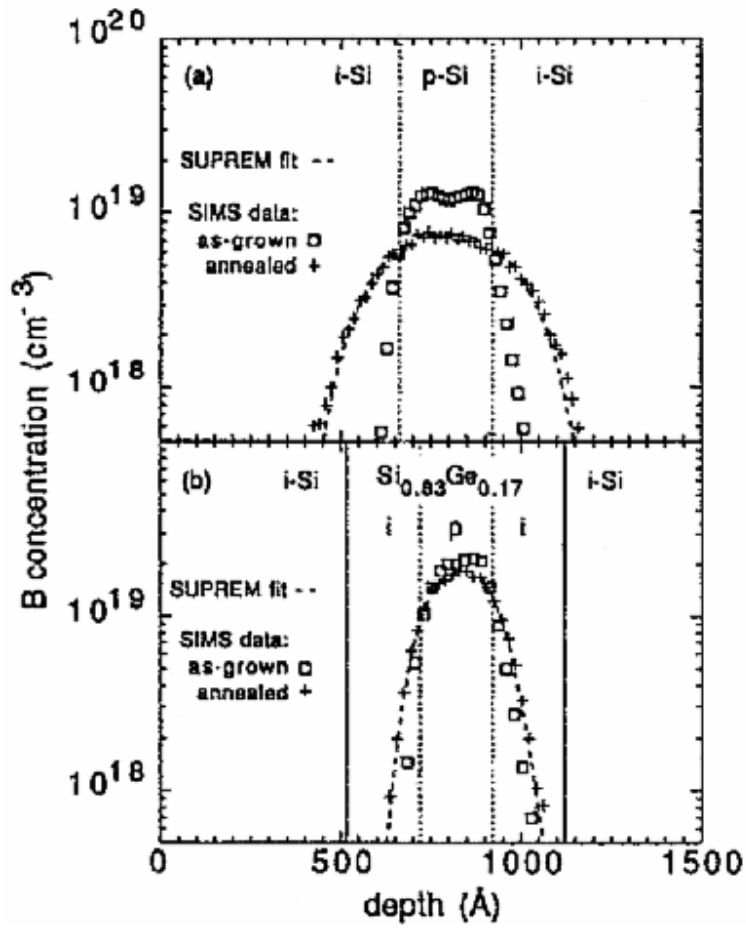


Figure 2-16. Diffused B profiles after 30 minute anneal at 860°C in a) Si and b) Si<sub>0.83</sub>Ge<sub>0.17</sub> [Kuo93]

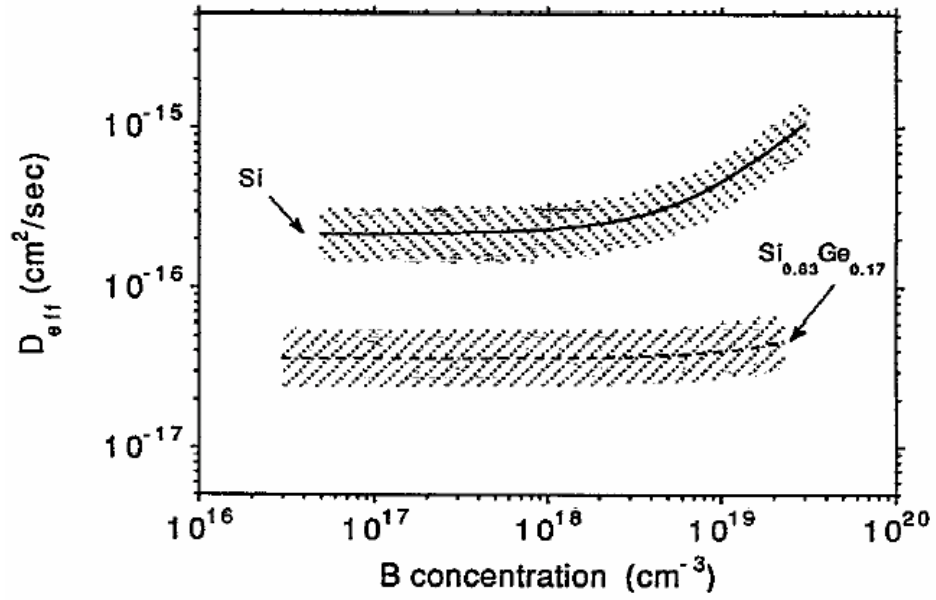


Figure 2-17. Effective B diffusivity as a function of B concentration [Kuo93]

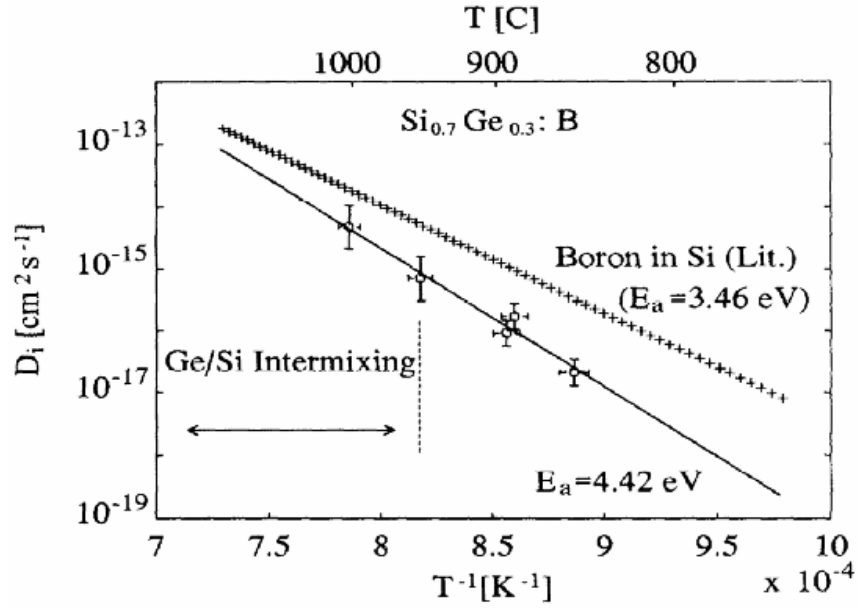


Figure 2-18. Diffusivity of B in  $\text{Si}_{0.7}\text{Ge}_{0.3}$  layer [Mor93]

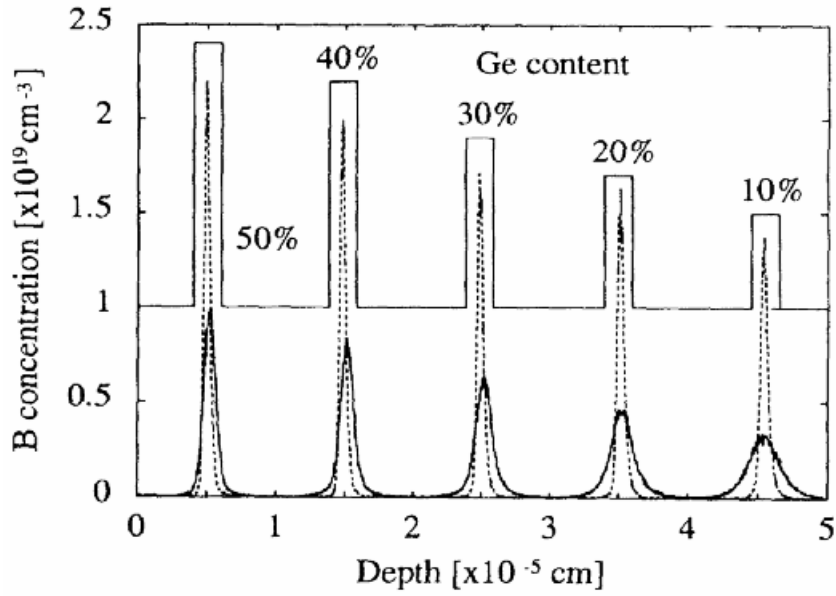


Figure 2-19. B profiles in multi-layer structure before (dashed line) and after (solid line) annealing at 975°C [Mor93]

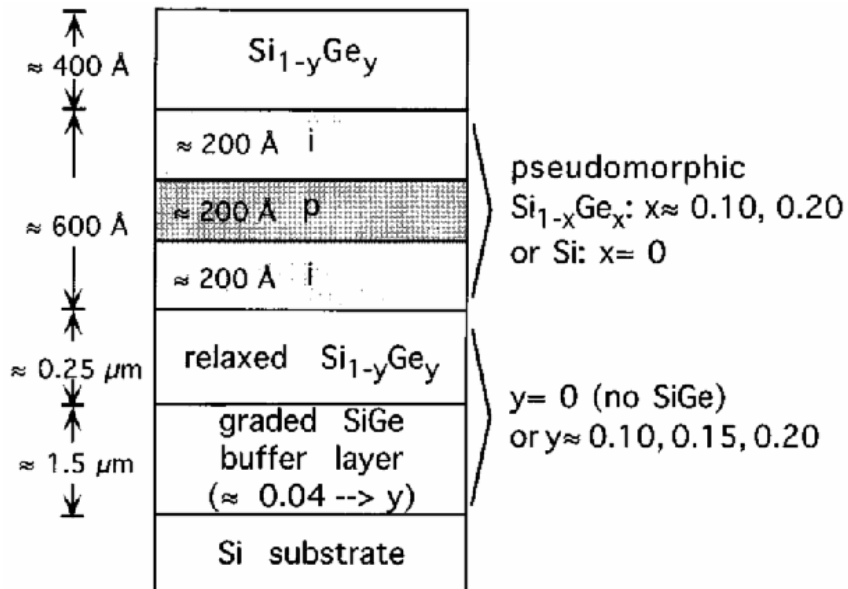


Figure 2-20. Illustration of a structure used by Kuo et al. [Kuo95a] showing relaxed  $\text{Si}_{1-y}\text{Ge}_y$  and pseudomorphic  $\text{Si}_{1-x}\text{Ge}_x$

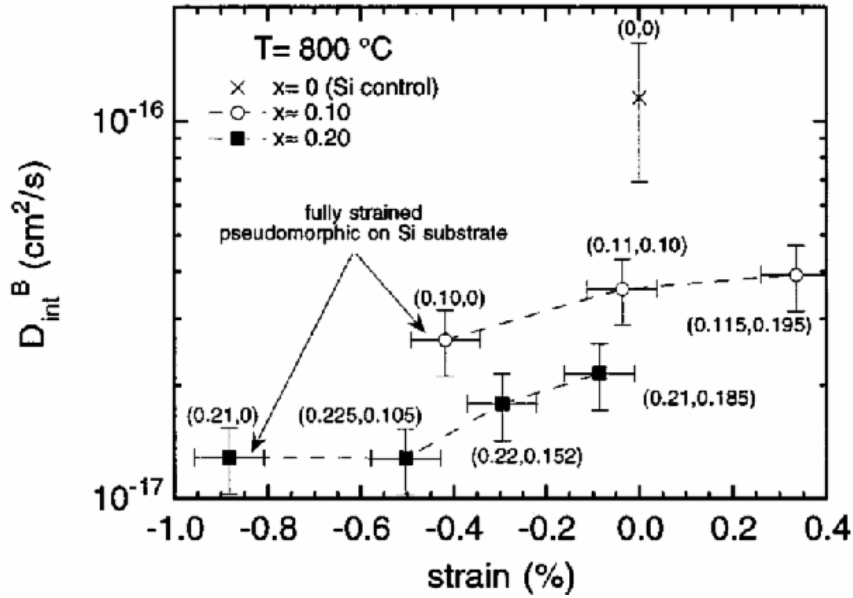


Figure 2-21. B diffusivity at  $800^\circ\text{C}$  as a function of strain, with the numbers in the parenthesis are (x,y) Ge content. Positive strain represents biaxial tension and negative strain biaxial compression. [Kuo95a]

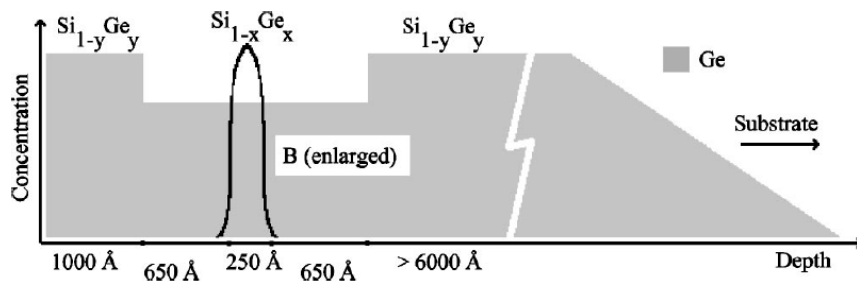


Figure 2-22. Schematic description of the structure used by Zangenberg et al. [Zan03] to measure B diffusion in  $\text{Si}_{1-x}\text{Ge}_x$

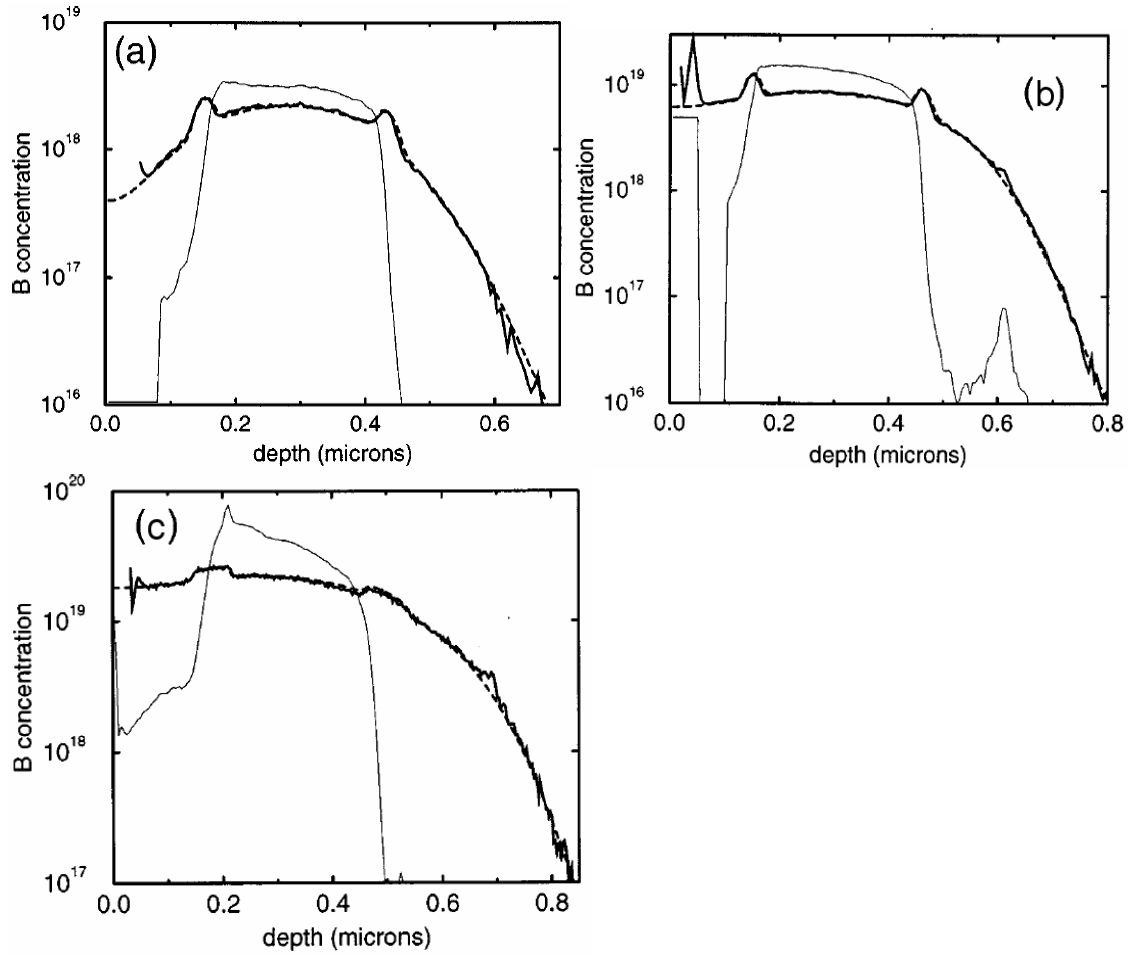


Figure 2-23. B profiles before (thin line) and after (thick)  $850^\circ\text{C}$  annealing of a given B well concentration. Figure a) B well with a concentration of  $3 \times 10^{18} \text{ cm}^{-3}$ , sandwiched in  $\text{Si}_{0.9}\text{Ge}_{0.1}$  layers, annealed for 96 hours. Figure b) B well with a concentration of  $1.5 \times 10^{19} \text{ cm}^{-3}$ , sandwiched in  $\text{Si}_{0.9}\text{Ge}_{0.1}$  layers, annealed for 96 hours. Figure c) B well with a concentration of  $4 \times 10^{19} \text{ cm}^{-3}$ , sandwiched in  $\text{Si}_{0.97}\text{Ge}_{0.03}$  layers, annealed for 24 hours. [Lev98]

## CHAPTER 3 BORON CLUSTERING IN SILICON

### Overview

This chapter discusses the behavior of boron-interstitial clusters (BIC) and its influence on activation of B in silicon. Experimental evidence shows that the previous model and its behavior with respect to annealing ambient do not capture the observed cluster dissolution phenomena. The most recent set of ab-initio calculated formation energies is utilized in attempt to capture this phenomenon, which is achieved with certain changes within the ab-initio energetics.

The cluster formation is examined in the experiment of Jones et al. [Jon96a], which indicates that the formation is a rapid process and is completely prevented by preamorphization. Assuming the inability of silicon interstitials entering the amorphous layer significantly reduces the percentage of boron tied in the clusters. Additional, small changes of the cluster properties further reduce the formation probability of the clusters, thus matching the experimentally observed behavior.

### **3.1 Boron-interstitial Cluster Dissolution**

#### **3.1.1 Introduction**

Ion implantation is the preferred method of introducing dopants due to the precision of implanted dose, control and repeatability. Future technology nodes will require highly doped shallow junctions processed with a low thermal budget. Such conditions emphasize the role of point defects generated by the implantation process. Recombination of point defects and dopant activation take place during annealing post

implantation. For nonamorphizing implants, the annealing step can form extended defects and dislocation loops, which are responsible for enhanced diffusion [Eag94][Jon96b]. Besides effects on dopant diffusion, high interstitial concentrations are also known to deactivate boron, through the formation of boron-interstitial clusters (BIC)[Sto95].

Ab initio studies provided information on the stability of some clusters, used in several implementations of BIC models in Monte Carlo [Cat98] and continuum process simulators [Pel97][Lil97]. It is unclear if boron will cluster in an interstitial supersaturation lower than that found in ion implantation, and if measurement methods would be able to distinguish such a presumably low concentration of clustered boron from the noise of the active boron profile. Specifically, characterization of low cluster densities is difficult, as low cluster densities are not detectable as spikes in the profile acquired by secondary ion mass spectrometry (SIMS) profiles and could be below detection limit of spreading resistance or Hall effect measurements. The behavior of BICs during dissolution, with respect to interstitial supersaturation, has not been verified experimentally. The model proposed by Pelaz [Pel99] suggests that break up of the clusters requires an interstitial to drive the process along an interstitial lean path. This theory says that the boron is driven to cluster in a large interstitial supersaturation, but a lower supersaturation might provide excess interstitials that will speed cluster dissolution and boron reactivation. Notwithstanding, experimental evidence suggests that BICs can serve as a source of interstitials for transient enhanced diffusion (TED), by dissolution of boron clusters in later stages of annealing [Sol00].

To test the theory of BIC cluster dissolution through interstitial lean path, implants of boron were performed to achieve peak boron concentration on the order of  $10^{19} \text{ cm}^{-3}$ .

Annealing is performed in two steps. Boron interstitial clusters form during first anneal step and deactivate a significant part of the dose. The second anneal is used to determine the influence of annealing ambient on cluster formation or dissolution. Clustering effects are investigated via SIMS and Hall effect measurements.

### 3.1.2 Experimental

Czochralski <100> n-type silicon wafers were implanted with boron. Three implant conditions with nominal boron peak concentrations of  $10^{19} \text{ cm}^{-3}$  were investigated. Implant doses and energies were  $1 \times 10^{14} \text{ cm}^{-2}$  at 5 keV,  $2 \times 10^{14} \text{ cm}^{-2}$  at 10 keV and  $4 \times 10^{14} \text{ cm}^{-2}$  at 20keV, respectively. The first anneal step was performed at 750°C for 30 minutes in inert N<sub>2</sub> ambient. To investigate the influence of ambient on B cluster dissolution, subsequent anneals were done in inert (N<sub>2</sub> flow) or oxidizing (dry O<sub>2</sub>) ambient at 850°C for 10, 20, 30 and 60 minutes. Oxidation of silicon is known to inject interstitials [Hu74], allowing investigation of BICs in a low supersaturated interstitial environment.

Samples were analyzed by SIMS, Hall effect and ellipsometry measurements. Boron depth profiles were measured by CAMECA IMS-3f instrument using O<sub>2</sub><sup>+</sup> primary ion beam and magnetic sector analyzer. Raster size and analyzed area were 200 μm and 60 μm in diameter, respectively. Samples were biased at 4.5 kV with an effective impact energy of 5.5 keV. The Woollam EC110 ellipsometer was used for oxide thickness measurements, showing no difference between initial condition and inert annealed samples. Oxide thickness measurement of samples annealed in oxidizing ambient was used in aligning SIMS profiles, due to the consumption of silicon. Measured oxide thickness agreed well with standard predictions at these temperatures. The active dose was measured using a MMR Technologies Inc. Hall-van der Pauw system. Measurements

were performed using a magnetic field of 300 mT with the current ranging from 1  $\mu\text{A}$  to 1 mA at room temperature. Square shaped samples with 14 mm sides had 1 mm diameter e-beam deposited Al contacts placed symmetrically near the corners. Factors contributing to the inaccuracy of the measurement include nonuniform dopant distribution and heavy to light hole ratio. Assuming measured profiles were steep enough to neglect the influence of deeper layers with lower dopant concentration and higher mobility, we chose the value of 0.7 for the Hall mobility factor [Sas88].

### **3.1.3 Results and Discussion**

First annealing step provides the initial condition with BICs of similar peak concentrations for studied implant conditions (Fig. 3-1). During this anneal excess interstitials generated by the implantation process interact with boron forming BICs. These clustered boron samples are referred to as the initial condition from this point on.

Fig. 3-2 shows boron profiles at critical stages of thermal processing for each of the studied implant conditions. Comparison of oxidized and inert annealed profiles show oxidation enhanced diffusion for the boron as expected for an interstitial diffusing species [Pac90]. Direct comparison of the clustered fraction is difficult from the SIMS results because of the extra diffusion. Although the shallowest implant exhibits the highest diffusion enhancement, we do not believe the distance to the surface to be significant. Different diffusion enhancements may be a consequence of a difference in the initial clustered dose, as oxidation is known to create enhancements uniformly deep in the bulk [Gri85]. The surface influence in these samples is mostly through segregation and outdiffusion of boron, resulting in dose loss (Table I). Dose loss is most apparent in

lowest implant dose/energy sample, since it has the shallowest boron profile in presented sample set (Fig. 3-2c).

Hall effect measurements during various stages of annealing are shown in Fig. 3-3. The initial anneal deactivates a large fraction of the dose, creating the initial clustered concentration that establishes our initial condition. Subsequent annealing activates the boron by dissolving the clusters, with inert anneals consistently having a higher active dose than oxidizing anneals. Considering dose loss and reactivation effects are mixed in the Hall effect measurement, defining activation as ratio of active to retained dose (integrated SIMS profile) is used to distinguish them. Activation fractions for known boron profiles are presented in Fig. 3-4. Increase of activation by 15-40% for inert annealed over oxidized annealed samples confirms the trend demonstrated by the Hall effect measurement. That leads to the conclusion that boron clusters dissolve slower in the oxidizing ambient than in the inert ambient.

Provided that one of the dominant BICs has a self-interstitial release reaction during dissolution, its dissolution rate would be diminished or annulled with the increase in the interstitial concentration. Since the oxidation induced interstitial injection reduces reactivation (Fig. 3-3) when compared to the inert ambient anneal, which leads to the conclusion that one of the significant clusters has an interstitial release reaction during dissolution.

Examining the time dependence of the reactivation shows disagreement with the idea of one dominant BIC. In the course of the second stage anneal, one can observe the initial increase in activation in almost all samples irrespective of the annealing ambient. After the initial increase, active dose in oxidizing ambient stays constant, while inert

ambient continues to reactivate B at longer anneal times. Supposing the reactivation processes occurring under oxidation are also occurring in inert ambient as well, one could consider inert reactivation as a superposition of oxidizing and an additional long-term reactivation. This would indicate there are at least two clusters holding a significant B dose. The one responsible for the short time reactivation would be rather insensitive to the ambient. On the other hand, the long-term reactivation would be coming from a cluster whose dissolution is affected by interstitial injection.

### 3.1.4 Modeling

In attempt to model the oxidation behavior we utilized the energetics published by Liu et al. [Liu00] The model is implemented in model description language ALAGATOR, assuming diffusion limited reaction rates, and simulated using the process simulator FLOOPS [FLO02]. Implanted ion and damage profiles are generated by UT-Marlowe [UTM00]. Boron clustering and cluster dissolution paths are shown in Fig. 3-5a. The clustering process is different from previously described model [Pel99]. During high interstitial supersaturation, BICs grow towards B and  $Si_{Int}$  rich, which later release interstitials to form B rich,  $Si_{Int}$  poor clusters. However, there are two clusters,  $B_3I$  and  $B_2I_3$ , containing the majority of the B dose, as opposed to exclusively  $B_4I$  [Pel99]. Regarding the dissolution paths, they would indicate opposite reaction to oxidizing ambient than seen in experiment. Oxidation injected interstitials would be captured by  $B_3I$  enhancing the transition towards  $B_3I_2$ . This is the rate limiting step, since the migration energy of a BI is lower than that of  $Si_{Int}$ , and  $B_3I_2$  can subsequently dissolve with the release of BI solely.

Simulation of the two-step anneal used in the experiment resulted in Fig. 3-5b and shows the simulated activation during second anneal step. One can observe a good fit to

clustered condition after the first anneal step. The reactivation during second anneal step is rather insensitive to oxidizing ambient. This is the consequence of similar  $B_2I_3$  and  $B_3I$  doses after the first anneal step, as  $B_2I_3$  can provide more than sufficient number of interstitials available for  $B_3I$  reactivation.

In order for a given BIC to dissolve slower under oxidation, it would have to release an interstitial along its path to B substitutional. Then the interstitial injection would be able to slow down that reaction, as observed in experiment. Therefore, we propose that the ambient sensitive BIC,  $B_mI_n$ , would have at least as many Si interstitials as B atoms ( $n \geq m$ ). We modified the energetics in an attempt to model the oxidation behavior using  $B_4I_4$  and  $B_2I_3$  as the two dominant clusters. The resulting cluster formation and dissolution paths using the modified energetics are shown in Fig. 3-6a. In this proposed model,  $B_2I_3$  provides the reactivation at short times (less than 10 minutes) and is insensitive to oxidation. On the other hand,  $B_4I_4$  dissolution is affected by interstitial injection and provides reactivation at longer times. Simulation of the two-step anneal resulted in active dose plot shown in Fig. 3-6b. One can observe a good match to the initial clustered condition. The model also shows appropriate behavior under oxidation, which is the first such model according to the literature. Two-stage reactivation is also visible, as described previously.

## **3.2 Boron Cluster Formation and Preamorphization**

### **3.2.1 Experiment and Findings**

One of the frequently applied methods for increasing activation of B implants is preamorphization. There are multiple benefits and some disadvantages to this method. Important benefits include: reduction in boron clustering, high activation at very low temperatures during the solid phase regrowth, and reduction of the junction depth by

reduction of the channeling tail. The main disadvantage is the formation of extended defects in the EOR region, which is detrimental to the electrical characteristics of the *pn* junction.

In an investigation of B clustering Jones et al. [Jon96a] implanted a Si dose of  $5 \times 10^{15} \text{ cm}^{-2}$  at energy of 146 keV, at liquid nitrogen temperatures. The implanted material contained three B marker layers, grown via MBE, as seen in Fig. 3-7.

The Si implant at 146 keV produced an amorphous layer 0.324  $\mu\text{m}$  thick, having the damage peak concentration coincide with the middle marker layer. Upon annealing at 800°C, the excess interstitials in the damaged region interact with B in the marker layers beneath the amorphous/crystalline (*a/c*) interface. This can be observed at longer annealing times as the immobile B spikes, at the position of the B peak, as seen in Fig. 3-8. The center B marker layer is almost completely immobile during the 3 minutes of annealing. At that time the shallowest peak is diffused out showing no signs of clustering, while the deepest marker layer exhibits an apparent clustering peak. The difference between the outer two peaks is interesting since they are almost the same distance from the *a/c* interface. Assuming the damage is concentrated in the region just beneath the *a/c* interface, the shallowest and the deepest marker layers should observe the same interstitial supersaturations. This assumption is partially validated from the similarity in the observed profile broadening shown in Fig. 3-8. Although the deepest marker layer has higher peak concentrations during the anneal when compared to the shallowest marker layer, it still experiences similar diffusion enhancement, i.e. interstitial supersaturation. The apparent clustering peak revealed at longer annealing times indicates the difference in the material structure, between deepest marker layer in the crystalline silicon and the

shallowest marker layers in amorphous silicon, might be responsible for the existence of the BICs.

The question then becomes if it is a material structure, or just an observable consequence of the different interstitial supersaturations each of the marker layers experiences at short times. Even though the regrowth of the 0.15  $\mu\text{m}$  between the shallowest and middle marker layer takes less than 0.25 seconds (according to [Ols88]), the supersaturation could drop by a factor of 2 or more during that time [Cow99]. The delay of the *a/c* interface reaching the shallowest marker layer facilitates avoiding the initial high interstitial supersaturations forming BICs in the middle marker layer, allowing only the lower interstitial concentration reaching the shallowest marker layer, and could also be contributing to the reduction in the BIC formation.

### **3.2.2 Modeling**

A UT-Marlowe simulation used to verify that the assumed distribution of excess interstitials following an amorphizing implant is shown in Fig. 3-9. The excess interstitial profiles obtained from the UT-Marlowe implant simulation show that the damage is not concentrated solely around the middle marker layer and limited to the region just beneath the *a/c* interface. Rather, there are excess interstitials that could provide the interstitials and boron in a sufficient proximity for cluster formation in the deepest marker layer.

Assuming that the silicon and boron interstitials are not able to enter the amorphous layers inserts a delay in the cluster formation of the shallowest B marker layer.

Presuming that the boron cluster formation is fast, the delay could prevent the BIC formation since most of the available Si interstitials would already be tied in clusters, either BICs or self-interstitial clusters. The delay would also mean that SMICs could be

dissolved by the time the *a/c* interface reaches the shallowest marker layer, thus the interstitial supersaturation would be significantly reduced. The reduction of the interstitial supersaturation affects the BIC formation in two ways, through reduction of self-interstitials and boron interstitials, again limiting the BIC formation.

To test this hypothesis, an additional equation was used to calculate the amorphous layer depth in the simulation. The self-interstitial and boron interstitial diffusivities were annulled in the region above the *a/c* interface, thus disabling their diffusion and their reactions to any other species. This forms a reflecting interface boundary at the position of the *a/c* interface, as it moves towards the surface. The *a/c* interface depth equation (Eq. 3-1) uses the regrowth velocity measured by Olson & Roth [Ols88] in units of  $\mu\text{m/s}$ . The diffusivity of self-interstitial and boron interstitials were limited to the crystalline material, as shown in the Eq. 3-2 and 3-3, with the reaction term omitted for brevity.

$$\frac{\partial(aSi\_depth)}{\partial t} = -3.1 \cdot 10^{12} \cdot \exp\left(\frac{-2.7eV}{kT}\right) \quad (3-1)$$

$$\frac{\partial Int}{\partial t} = D_{Int} \cdot (x > aSi\_depth) \cdot \frac{\partial^2 Int}{\partial x^2} + reaction\_terms \quad (3-2)$$

$$\frac{\partial BI}{\partial t} = D_{BI} \cdot (x > aSi\_depth) \cdot \frac{\partial^2 BI}{\partial x^2} + reaction\_terms \quad (3-3)$$

The following simulation results illustrate the influence of spatial separation between the boron profile and the excess interstitials. The case chosen for this demonstration is the annealing a boron dose of  $4 \times 10^{14} \text{ cm}^{-2}$  implanted at 20keV. Figure 3-10 shows the simulated doses of pertinent boron and interstitial clusters during a 30 minute anneal at 750°C, with boron implant performed without a preamorphization. Figure 3-11 shows the same boron implant, with a silicon preamorphization of  $1 \times 10^{15}$

cm<sup>-2</sup> implanted at 100keV, annealed under the same conditions. One of the benefits of the preamorphization is the smaller amount of excess interstitials remaining in the EOR region, as is apparent in this case, with excess interstitial dose of  $\sim 8 \times 10^{13}$  cm<sup>-2</sup>. In order to be able to compare the results, the excess interstitial dose in the preamorphized case was *ad hoc* increased by a factor of six, matching the excess interstitials available in the case without preamorphization.

There are several important values indicating the dominant processes in these simulations, namely  $S_{mic}$ ,  $C_{311}$  and  $B_{sub}$ . Initial  $S_{mic}$  dose is the initial dose of trapped interstitials that evolve into  $\{311\}$ 's during the course of the anneal. Without boron present, most of the excess interstitials in  $S_{mic}$ 's are captured by  $\{311\}$ 's.

In the case of boron implant into crystalline silicon (Fig. 3-10), only  $\sim 15\%$  of excess interstitials from  $S_{mic}$ 's are captured by  $\{311\}$ 's. The rest is trapped in various BIC configurations, reducing the substitutional boron dose to  $\sim 18\%$ . Displacing the excess interstitials by a preamorphization Si implant changes all of these values (Fig. 3-11). As the boron is relatively far away from the  $S_{mic}$  profile, most of the excess interstitial dose in the EOR region is captured in a form of a  $\{311\}$  defect. Interstitial supersaturation supported by the  $\{311\}$  defects eventually forms some BICs, still leaving  $>85\%$  boron in the substitutional position after the 30 minutes 750°C anneal. This demonstrates the increase in the substitutional boron dose by a factor of four using preamorphization with the equivalent excess interstitial dose, solely by spatial separation of the boron and excess interstitial regions.

Considering the actual preamorphization damage of a Si  $1 \times 10^{15}$  cm<sup>-2</sup> 100keV implant performed at liquid nitrogen temperatures, simulated excess interstitial dose is

quite lower than that of the B implant. Simulated doses (Fig. 3-12) show a certain insensitivity of the clustering process to the EOR trapped interstitial dose, as the boron substitutional dose drops to ~90%. This may not be unreasonable when compared to the previous case (Fig. 3-11) having artificially increased excess interstitial dose, as the {311} supported interstitial supersaturation does not depend on the defect density, size or trapped interstitial dose. Therefore, the boron profile should experience roughly the same interstitial supersaturation irrespective of the {311} dose, prior to its complete dissolution.

This confirms the displacement of the excess interstitial makes a difference between 18% activation (Fig. 3-10) in non-preamorphized case versus over 85% activation (Fig. 3-11, 3-12) in the preamorphized case. Coupled with the lower amount of excess interstitials in the realistic preamorphized case, such as a Si  $1 \times 10^{15} \text{ cm}^{-2}$  implant at 100keV with liquid nitrogen cooling, the activation can rise over 90% as seen in the Fig. 3-12.

Even though the previously described blocking of the interstitial and boron interstitial pair diffusion into the amorphous layer significantly reduces the clustered portion of the profile, it does not yield good fits to the profiles in Fig. 3-8. The simulated profiles for the annealing of 5 seconds, 30 seconds and 3 minutes at 800°C are shown in Fig. 3-13, 3-14, and 3-15, respectively. The SIMS profiles in these figures are the SIMS profiles from Fig. 3-8. In these figures, the  $B_{sub}$  represents the substitutional portion of boron profile, the only species assumed to be electrically active. The  $Total\_B$  profile represents all boron, irrespective of its configuration or position in the crystal lattice. The clustered boron concentration is not plotted for clarity, since it is inferred as  $Total\_B - B_{sub}$ .

One can notice that the shallowest and the deepest B marker peak magnitude are very similar throughout the simulation, in contrast to the SIMS profiles. This is interesting, particularly considering the different portions of the profile in a clustered state, visible as the different  $B_{sub}$  peak concentrations in Fig. 3-15. The time dependence is not captured well, as the shallowest and the deepest marker layers do not diffuse as seen in the SIMS. Considering the activation of boron in the shallowest peak drops only 14% from the full activation, this makes the significant reduction in diffusion enhancement interesting.

Presuming the formation of BICs is still too strong in the regrown amorphous layer, the model parameters were adjusted. The binding energy of the small clusters was reduced without affecting equilibrium diffusion, in an attempt to reduce their concentrations. This effectively prevents small BICs from serving as trapping and nucleation sites for larger BICs. The results from the simulations using the modified BIC model parameters are shown in Fig. 3-16, 3-17, and 3-18.

In these figures, one can observe the fairly good match for the middle B marker layer. At longer annealing times, it would seem that the clustered peak does not release enough mobile boron to retain the diffused tails around the clustered peak. The shallowest and the deepest marker layers have a similar peak concentration at shorter times despite the different clustered portions. Peak concentrations differ at longer times, revealing a clustered peak in the deepest marker layer that is not present in the shallowest marker layer. The shallowest marker layer does form clusters, but since the clustered dose dropped to around 1.7%, they are not visible in the profile.

The binding energies of the small BICs that were reduced to facilitate the reduction of clustering in regrown material did not significantly affect the other parameters of the model. That is due to the fact that the reactivation properties are the consequence of the dissolving cluster, in this case  $B_4I_4$ . The changes did seem to accelerate the  $B_2I_3$  dissolution, which was compensated by increasing its binding energies without the adverse effects on either clustering and reactivation simulations, or the simulations of BIC clustering in amorphous material. The overall increase in activation is partially due to the change in the formulation of interstitial supersaturation supported by {311}'s (C311 BindI) to match enhanced diffusion with the interstitial equilibrium concentration (Int Cstar) values used in the Liu et al. [Liu00][Win99], and partially due to the change in the model parameters. Two figures (Fig. 3-19, 3-20) compare the reactivation during second annealing stage at 850°C, in inert ambient, between the model presented earlier in the chapter and the changes introduced to capture the behavior in regrown silicon.

### 3.3 Conclusion

Boron interstitial clusters formed by a 750°C anneal after implantation deactivated the majority of implanted boron. These samples allow a study of the reactivation rate in two different ambient conditions. The oxidizing ambient shows consistently lower activation at a slower rate when compared to the inert ambient, which strongly demonstrates that the presence of excess interstitials slows cluster dissolution. This conclusion is contrary to the accepted BIC model, though it is supported by experimental evidence [Sol00] suggesting that BIC dissolution involves the release of silicon interstitials.

To model the oxidation behavior, we utilized the energetics published by Liu et al. [Liu00], with some modifications. The model implemented in the description language

ALAGATOR, and simulated using the process simulator FLOOPS [FLO02] captured the reactivation behavior, correctly distinguishing the reaction to the ambient atmosphere. An implementation of the reflective boundary at the *a/c* interface reduces the simulated clustered portion of the B implanted into amorphous silicon, as seen in the work of Jones et al. [Jon96a]. However, the reductions in binding energies of small BICs were necessary to model the clustering behavior in the crystalline, versus amorphous silicon.

Table 3-1. Retained boron dose [ $\text{cm}^{-2}$ ] in different processing steps. First anneal step is  $750^{\circ}\text{C}$ , 30 min in inert ambient. Second anneal step is  $850^{\circ}\text{C}$ , 60 min in respective ambient. Dose loss in lowest implanted dose sample is comparable to active dose measured by Hall effect measurement.

Implanted dose [ $\text{cm}^{-2}$ ]	First anneal step [ $\text{cm}^{-2}$ ]	Second anneal step	
		Inert [ $\text{cm}^{-2}$ ]	Oxidizing [ $\text{cm}^{-2}$ ]
$4 \times 10^{14}$	$3.69 \times 10^{14}$	$3.58 \times 10^{14}$	$3.33 \times 10^{14}$
$2 \times 10^{14}$	$1.75 \times 10^{14}$	$1.58 \times 10^{14}$	$1.25 \times 10^{14}$
$10^{14}$	$7.48 \times 10^{13}$	$7.01 \times 10^{13}$	$4.48 \times 10^{13}$

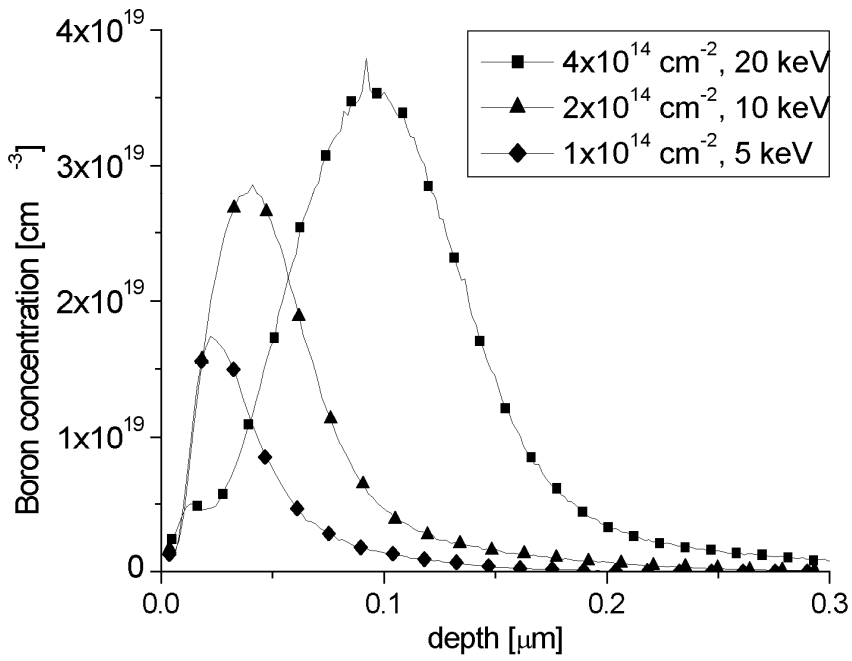


Figure 3-1. Secondary ion mass spectrometry (SIMS) measured boron profiles of investigated implant conditions (B implant  $1 \times 10^{14} \text{ cm}^{-2}$  at 5 keV,  $2 \times 10^{14} \text{ cm}^{-2}$  at 10 keV and  $4 \times 10^{14} \text{ cm}^{-2}$  at 20keV) after first anneal step, 750°C for 30 minutes in inert ambient.

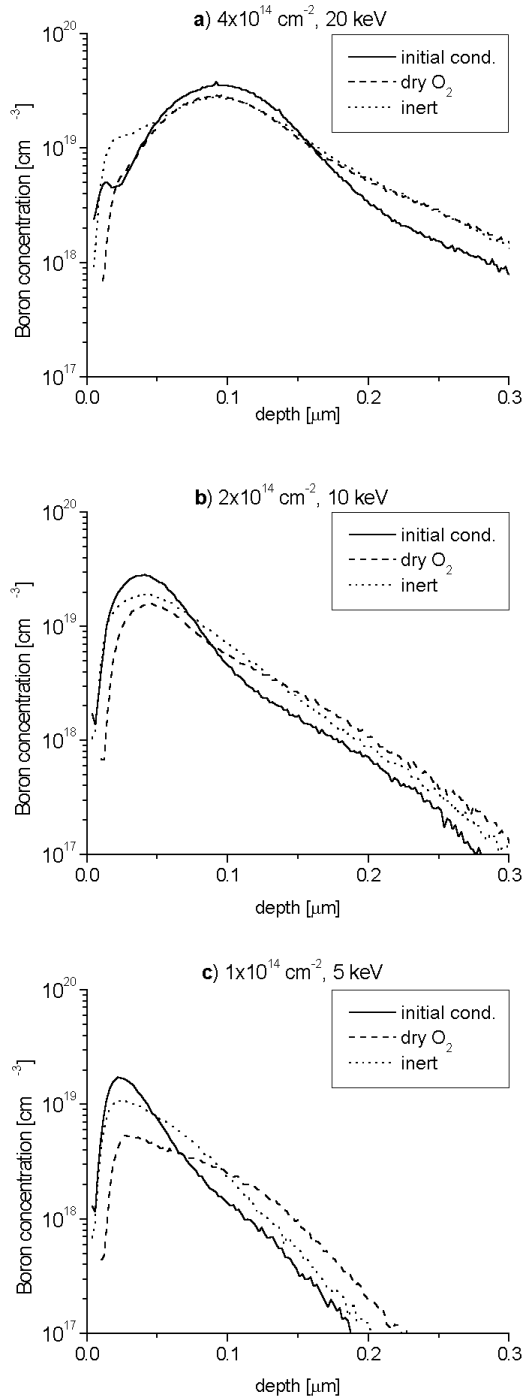


Figure 3-2. Secondary ion mass spectrometry (SIMS) measured boron profiles. Initial condition is after 750°C, 30 minutes inert anneal. Subsequent anneal is 850°C, 60 minutes in respective ambient. Figure parts a), b) and c) shows the result for a 4x10<sup>14</sup> cm<sup>-2</sup>/ 20keV, a 2x10<sup>14</sup> cm<sup>-2</sup>/ 10keV, and a 1x10<sup>14</sup> cm<sup>-2</sup>/ 5keV B implant, respectively. These conditions are chosen because the peak concentrations and initial clustered concentrations are similar.

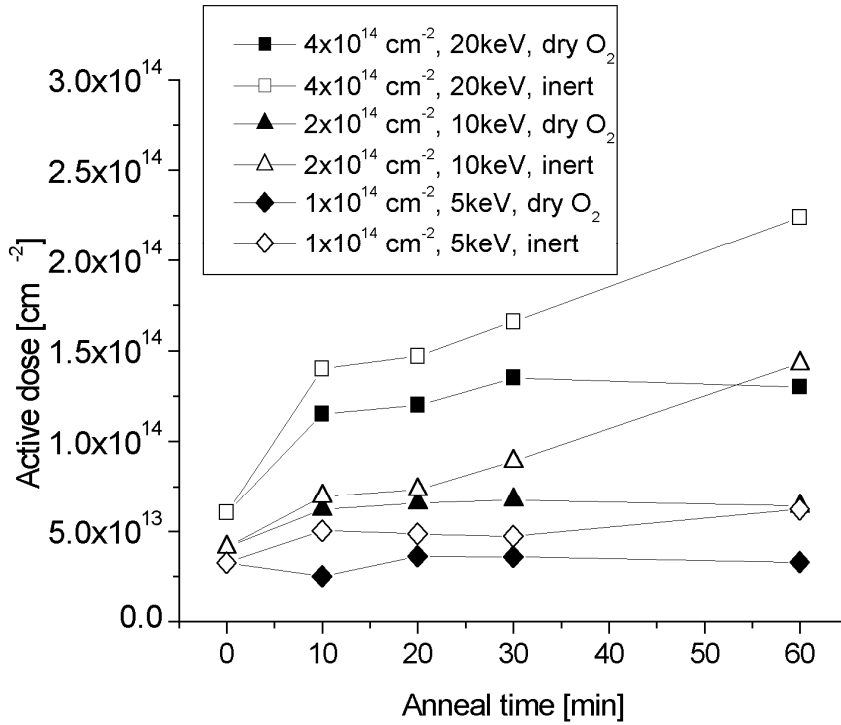


Figure 3-3. Active dose measured by Hall-van der Pauw method, during the annealing at 850°C. The time zero measurement corresponds to the condition after a 750°C, 30 minutes inert anneal.

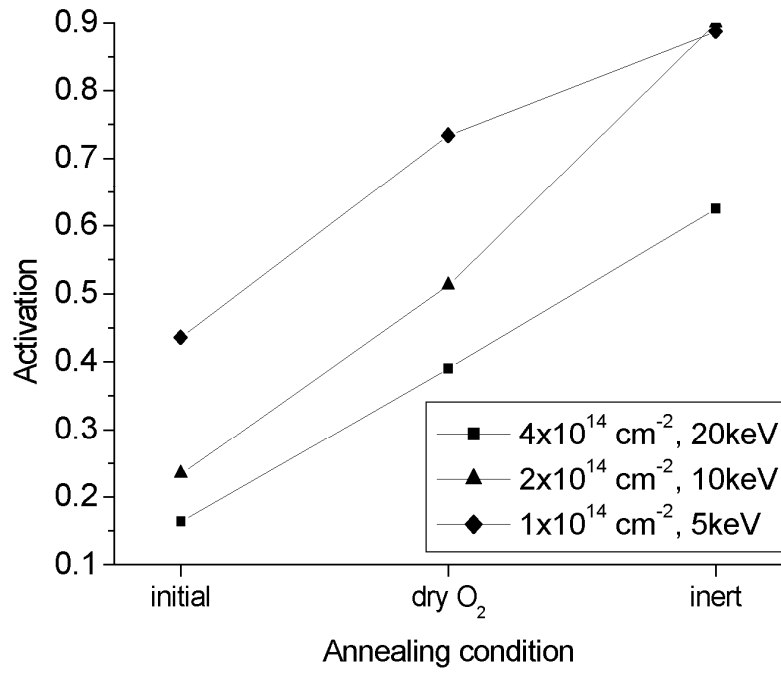


Figure 3-4. Active fraction, the ratio of active to retained dose (integrated SIMS profile), compared for the different annealing ambient at the end of the 850°C, 60 minutes anneal. The initial condition is after a 750°C, 30 minutes inert anneal.

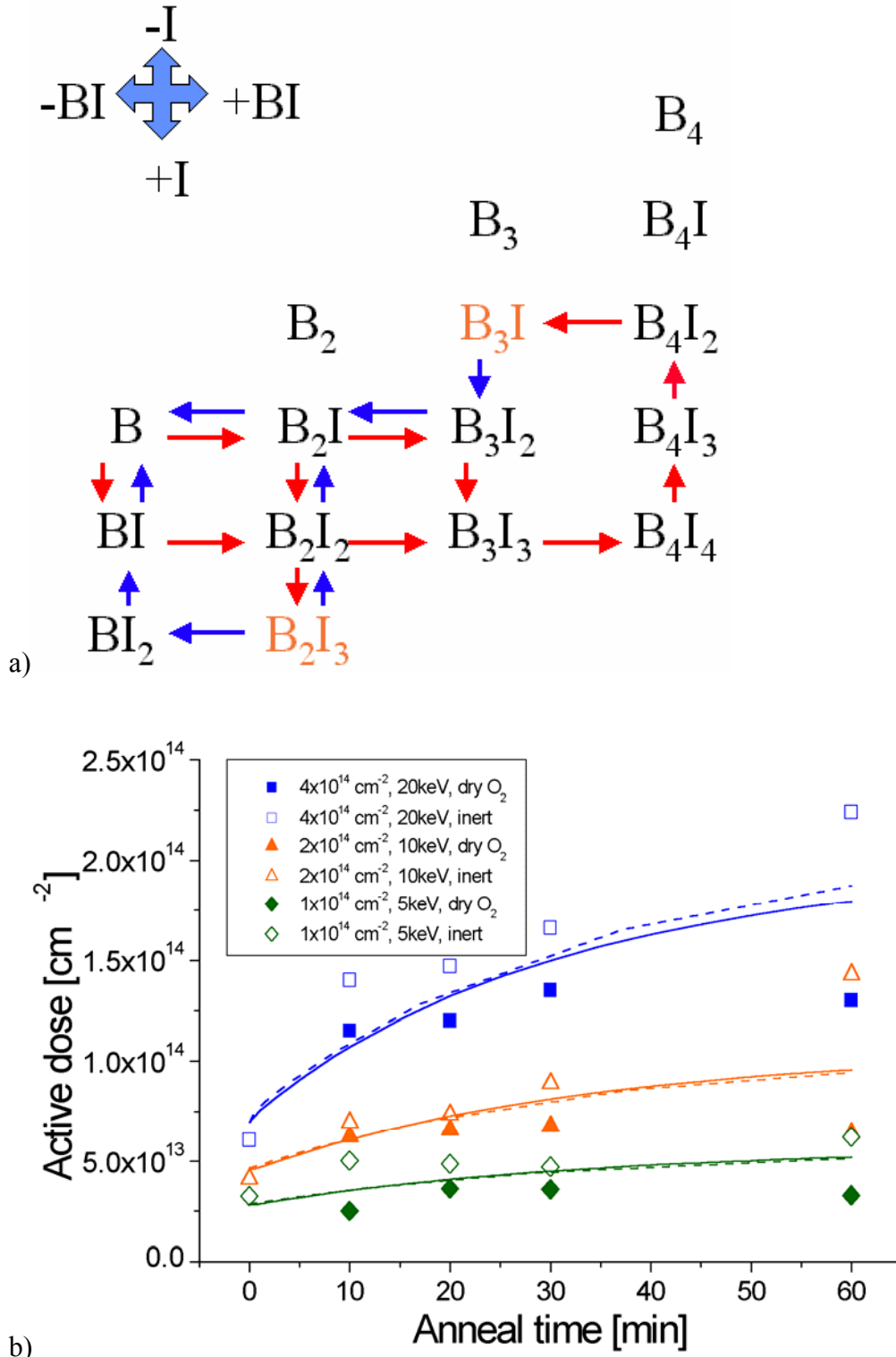


Figure 3-5. Major cluster formation and dissolution paths of Liu et al. [Liu00] with  $B_3I$  and  $B_2I_3$  containing most of the B clustered dose in figure a) and simulation of B clustering and dissolution during thermal processing used in experiment in figure b)

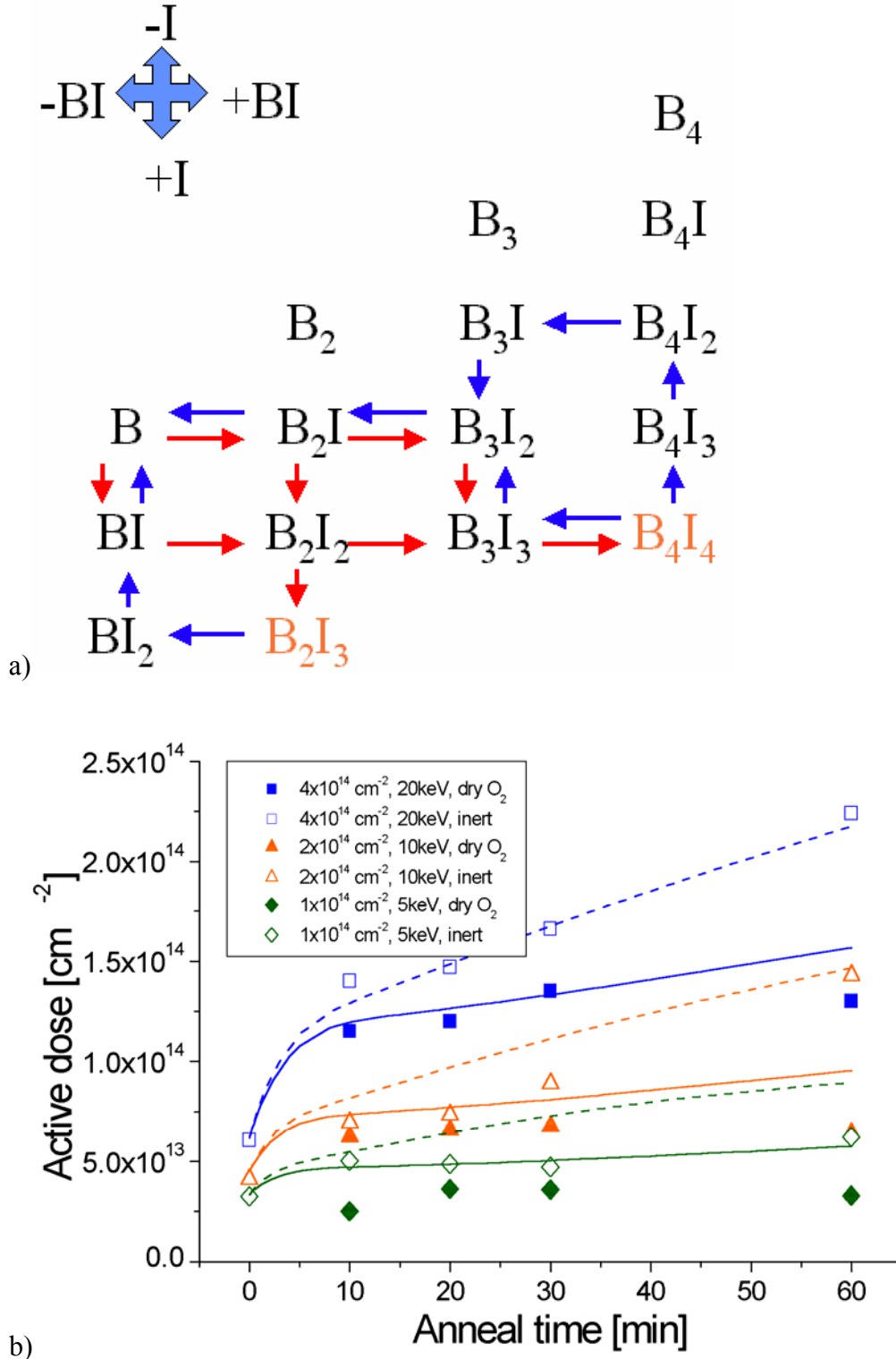


Figure 3-6. Cluster formation and dissolution paths of modified Liu et al. [Liu00] energetics, with  $B_4I_4$  and  $B_2I_3$  containing most of B clustered dose, are shown in figure a), with simulation of B clustering and dissolution (modified energetics) during thermal processing used in experiment is shown in figure b)

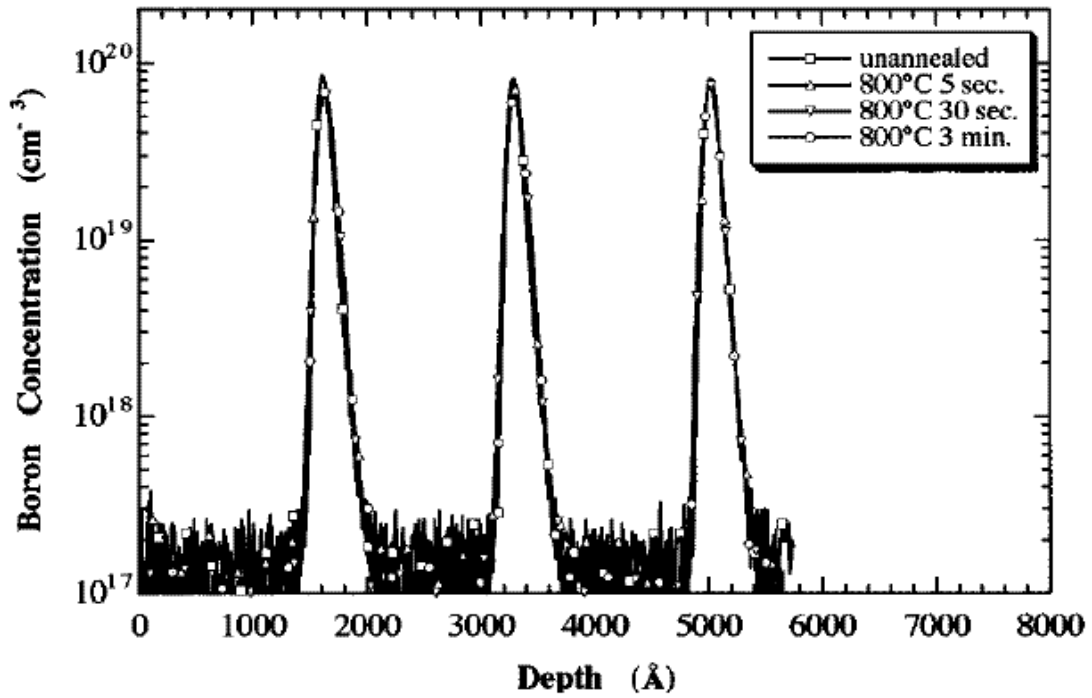


Figure 3-7. Boron profiles of material used in the study of Jones et al. [Jon96a], unimplanted and annealed in inert ambient at 800°C

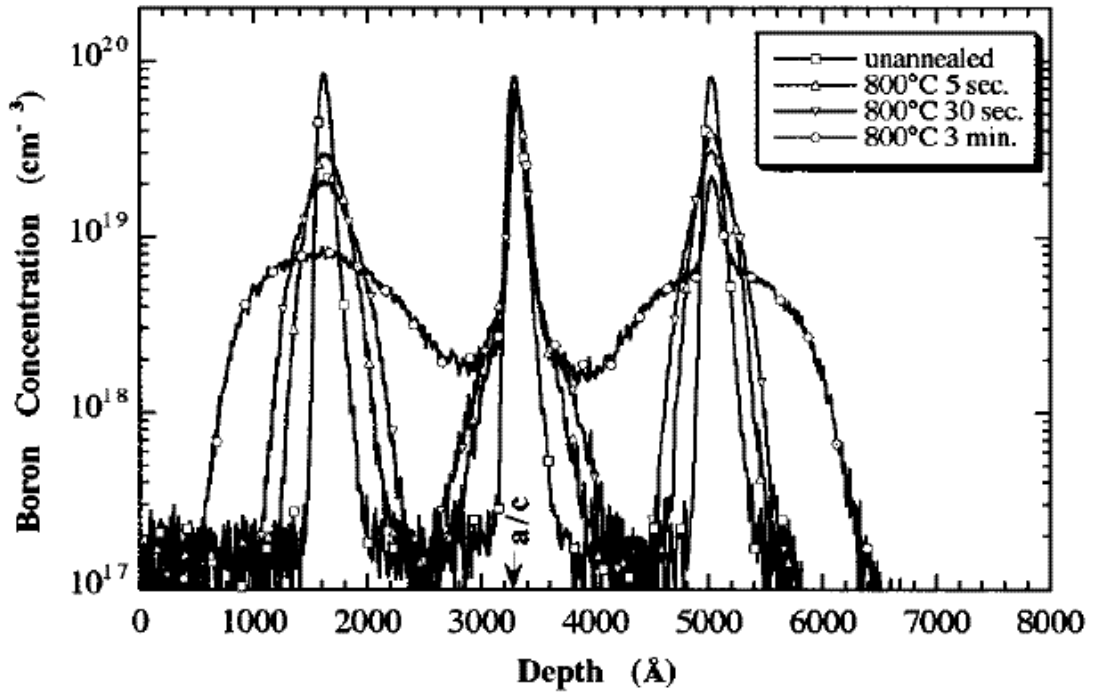


Figure 3-8. Boron profiles after a  $5 \times 10^{15}$  Si implant at 146keV, annealed in inert ambient at 800°C [Jon96a]

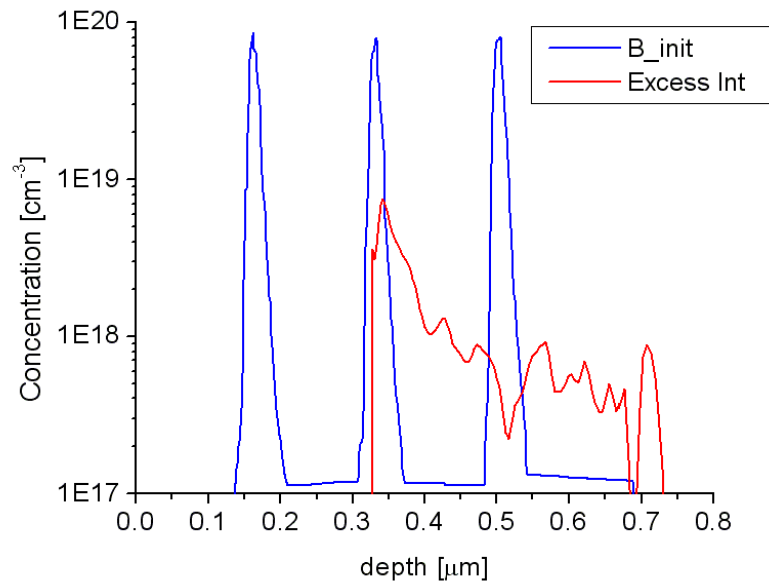


Figure 3-9. Boron marker layers and excess interstitial damage following a 146keV Si implant shows proximity of deepest marker layer to the damage

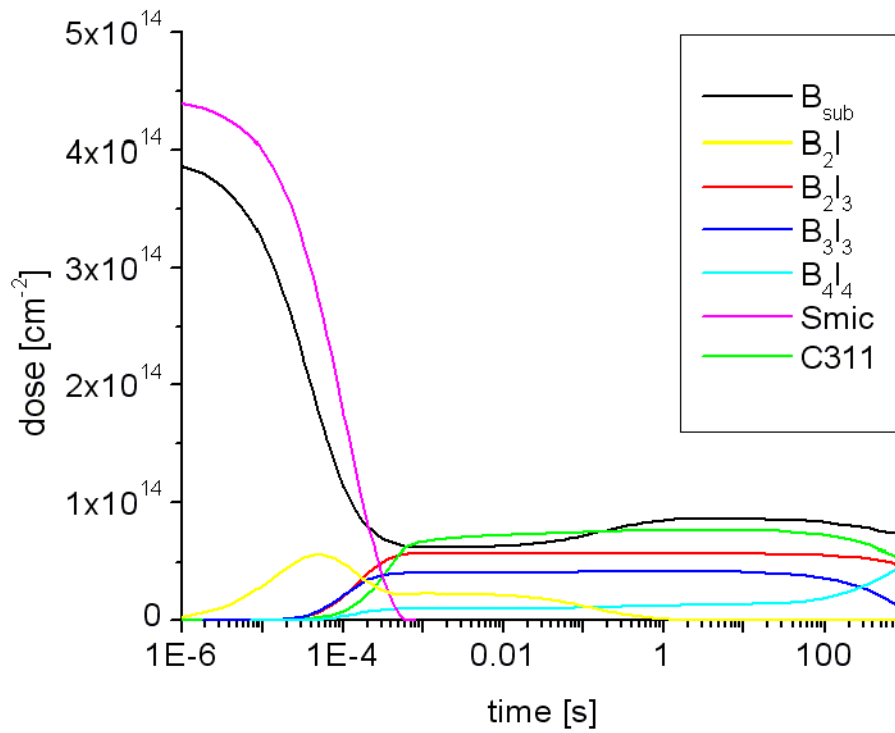


Figure 3-10. Doses of important clusters in a simulation of a B  $4 \times 10^{14}$  20keV implant into crystalline Si, during a 30 minutes 750°C anneal, resulting in activation  $\sim 18\%$

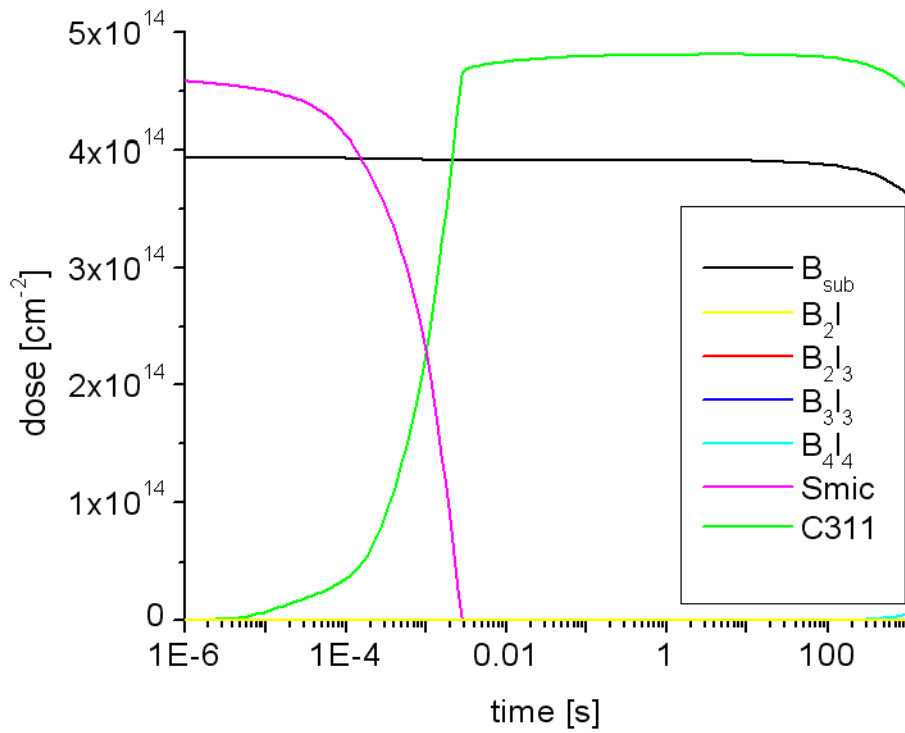


Figure 3-11. Doses of important clusters in a simulation of a  $B 4 \times 10^{14}$  20keV implant into preamorphized Si (with excess interstitial dose increased by a factor of 6), during a 30 minutes 750°C anneal, resulting in activation >85%

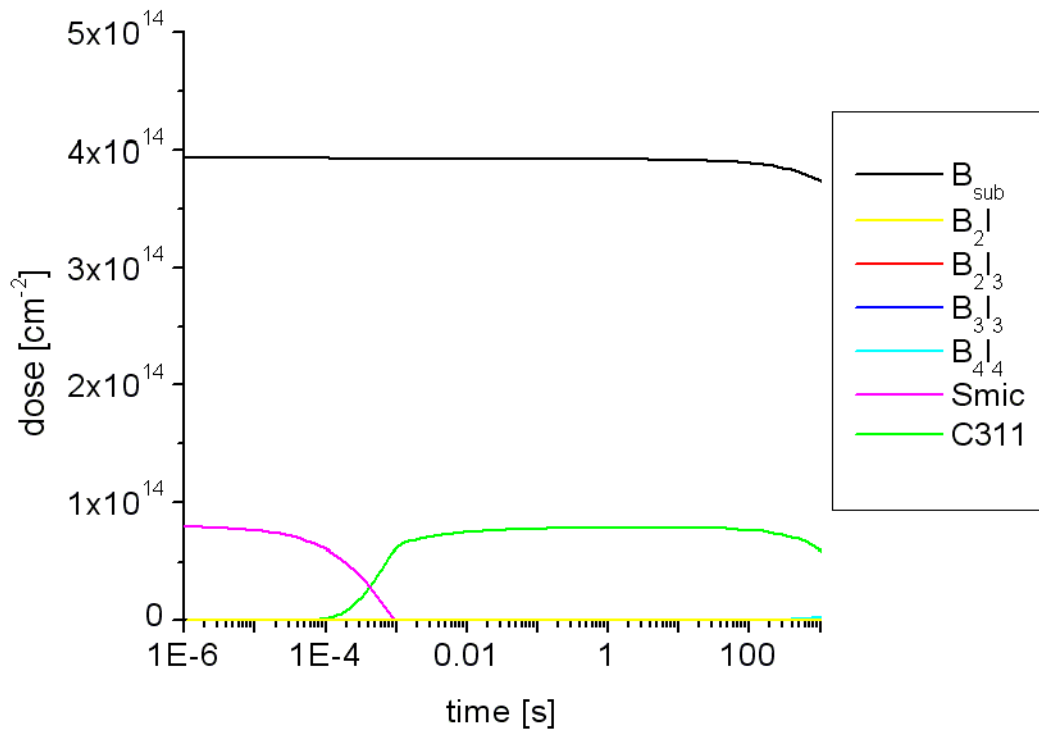


Figure 3-12. Doses of important clusters in a simulation of a B  $4 \times 10^{14}$  20keV implant into preamorphized Si (at liquid nitrogen temperatures), during a 30 minutes 750°C anneal, resulting in activation >90%

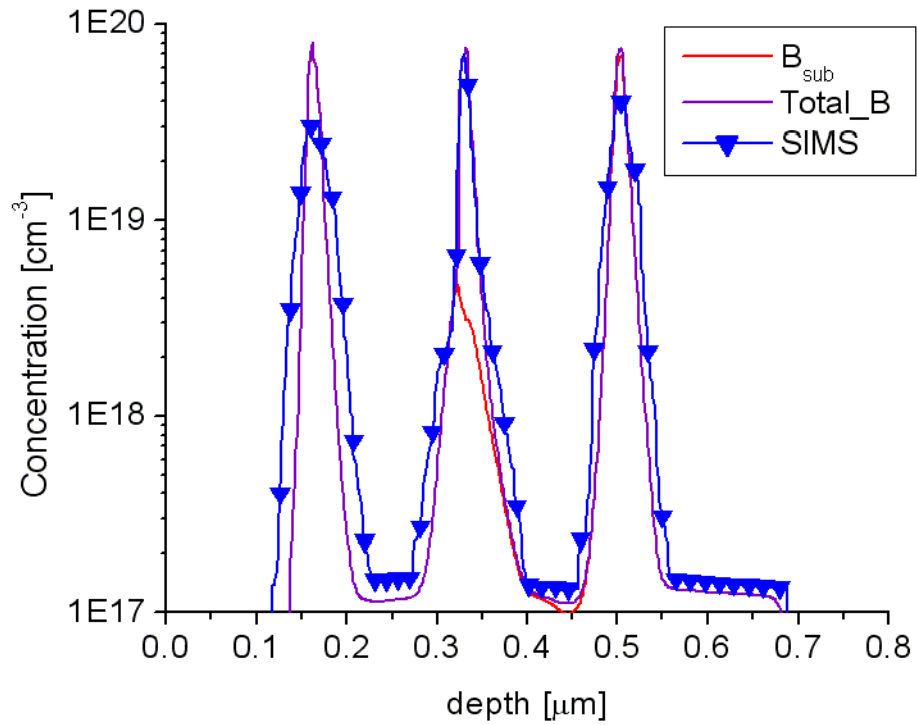


Figure 3-13. Simulated boron profiles after 5 seconds at 800°C, following a Si implant of  $5 \times 10^{15} \text{ cm}^{-2}$  at 146keV. Diffusion of self-interstitials and BI pairs are annulled in the amorphous material.

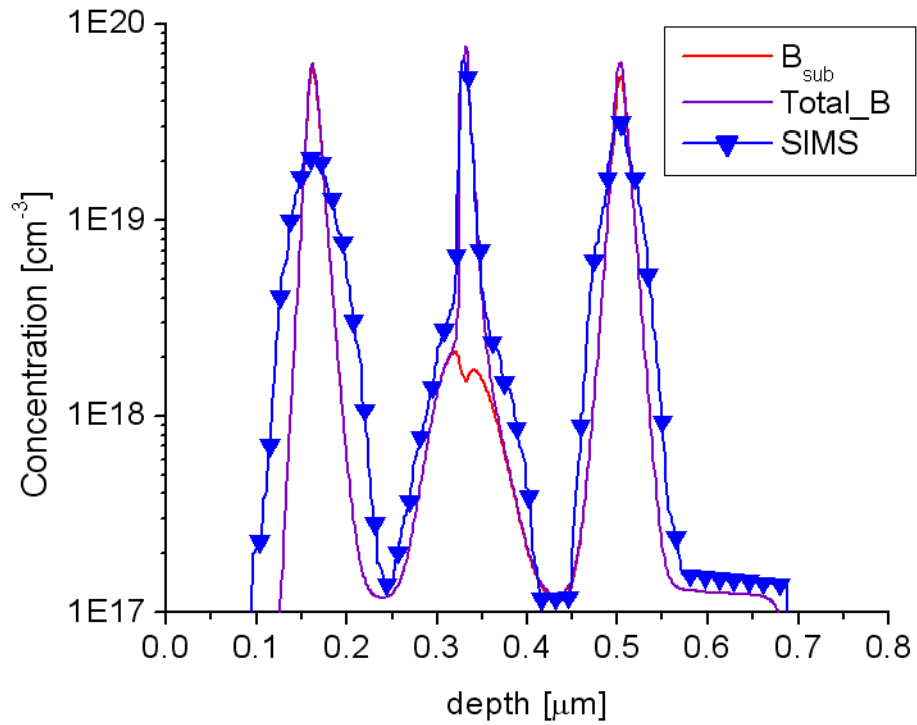


Figure 3-14. Simulated boron profiles after 30 seconds at 800°C, following a Si implant of  $5 \times 10^{15} \text{ cm}^{-2}$  at 146keV. Diffusion of self-interstitials and BI pairs are annulled in the amorphous material.

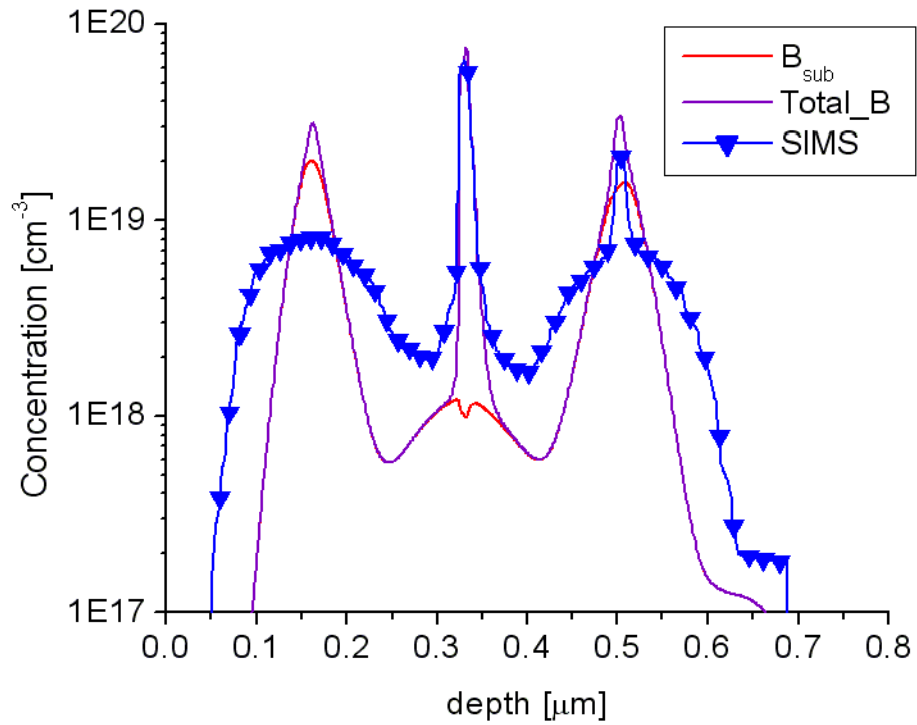


Figure 3-15. Simulated boron profiles after 3 minutes at 800°C, following a Si implant of  $5 \times 10^{15} \text{ cm}^{-2}$  at 146keV. Diffusion of self-interstitials and BI pairs are annulled in the amorphous material.

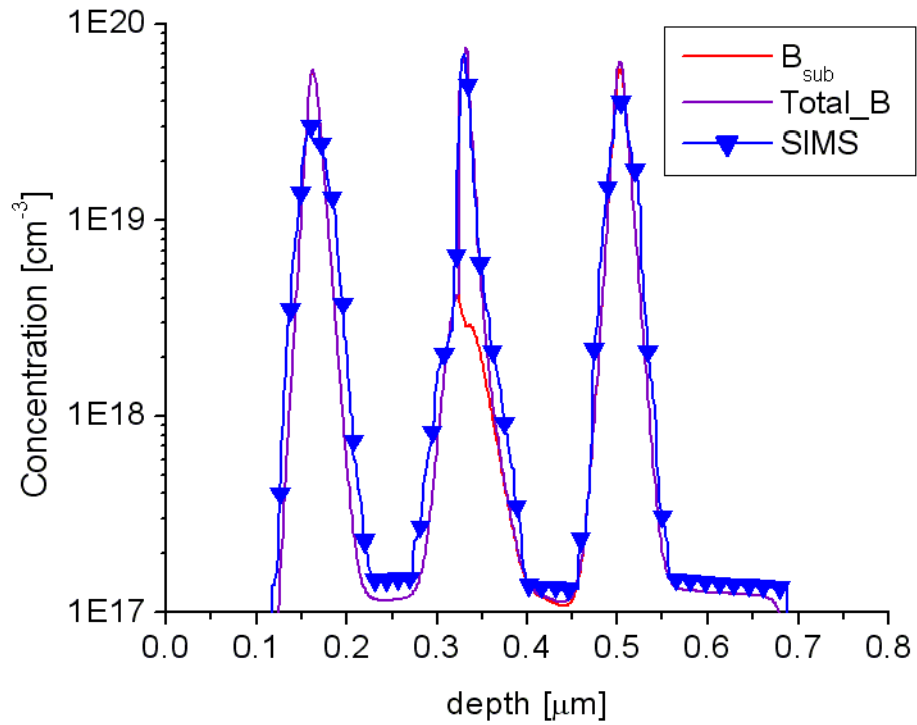


Figure 3-16. Simulated boron profiles after 5 seconds at 800°C, following a Si implant of  $5 \times 10^{15} \text{ cm}^{-2}$  at 146keV. Diffusion of self-interstitials and BI pairs are annulled in the amorphous material, and the binding energies of small BICs are reduced.

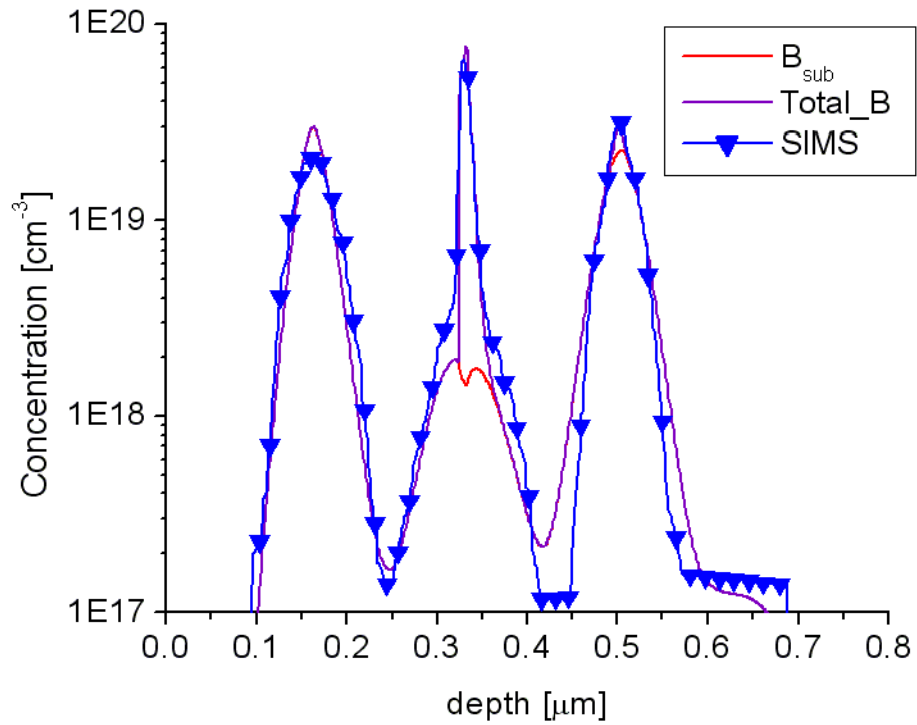


Figure 3-17. Simulated boron profiles after 30 seconds at 800°C, following a Si implant of  $5 \times 10^{15} \text{ cm}^{-2}$  at 146keV. Diffusion of self-interstitials and BI pairs are annulled in the amorphous material, and the binding energies of small BICs are reduced.

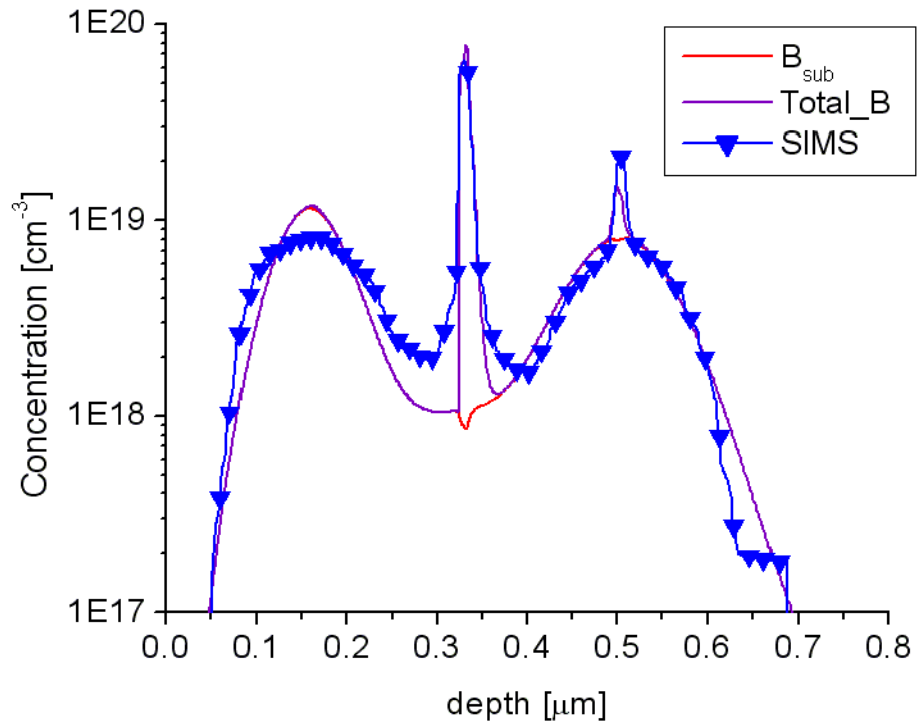


Figure 3-18. Simulated boron profiles after 3 minutes at 800°C, following a Si implant of  $5 \times 10^{15} \text{ cm}^{-2}$  at 146keV. Diffusion of self-interstitials and BI pairs are annulled in the amorphous material, and the binding energies of small BICs are reduced.

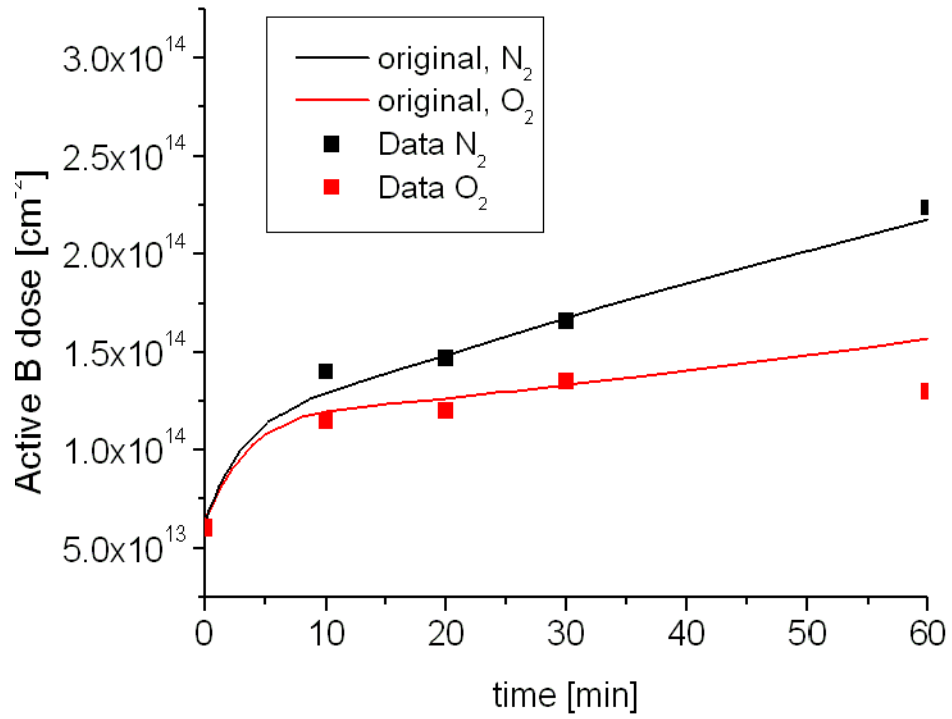


Figure 3-19. Simulated clustered doses in BIC experiment for B implant  $4 \times 10^{14}$  @ 20keV, model presented earlier in the chapter

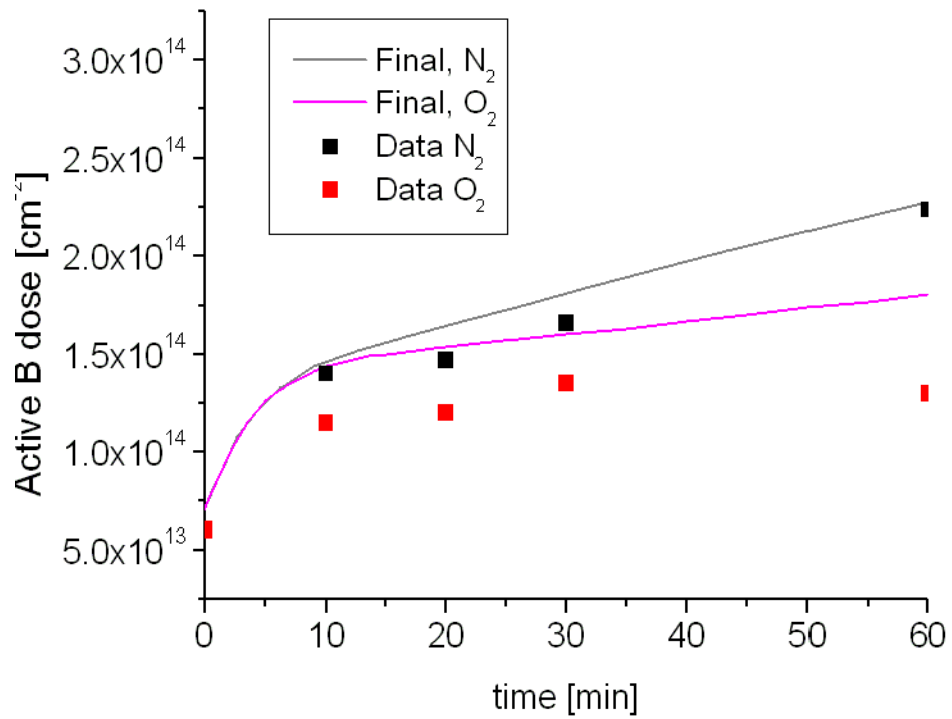


Figure 3-20. Simulated clustered doses in BIC experiment for B implant  $4 \times 10^{14}$  @ 20keV, model parameters adjusted to cover regrowth behavior [Jon96a]

## CHAPTER 4 BORON CAPTURE AT THE OXIDE/SILICON INTERFACE AND END-OF-RANGE DISLOCATION LOOPS

### Overview

This chapter discusses the phenomena of B diffusion near the oxide/silicon interface and end-of-range (EOR) dislocation loops under the interstitial supersaturation. The oxide/silicon interface traps the mobile BI pairs, thus providing an additional mechanism for removal of excess interstitials from the bulk and effectively reducing the diffusion enhancement. This chapter also discusses the experimentally observed segregation of B in the vicinity of EOR loops that is modeled through a trapping mechanism along the circumference of the loop.

### **4.1 B Interaction with Oxide/silicon Interface Under TED**

This section discusses an experiment designed to investigate Ge influence on B diffusion under transient enhanced diffusion (TED) conditions, with emphasis on the control samples. The following section focuses on the experimental phenomena observed in samples receiving no Ge implant, pertinent simulations and conclusions about interaction of B and oxide/silicon interface.

#### **4.1.1 Experimental Conditions**

Four float-zone (FZ) n-type Si <100> wafers, resistivity 70-130  $\Omega\text{cm}$ , were preamorphized by silicon implant with a dose of  $1 \times 10^{15} \text{ cm}^{-2}$  at an energy of 100keV. The Si preamorphization implant (PAI) provides an amorphous layer 0.23  $\mu\text{m}$  thick, as measured by cross-section transmission electron microscopy (XTEM). The implant was

performed at liquid nitrogen temperatures to ensure the surface layers would experience the TED. During the annealing following an implant under room temperature conditions, a loop layer could form at the amorphous/crystalline (*a/c*) interface, capturing the interstitials released from EOR damage and preventing the backflow of interstitials to the surface [Cha96]. Following the Si PAI, one wafer was implanted with Ge dose of  $4 \times 10^{15} \text{ cm}^{-2}$  at 30keV, hereon out referred to as sample A. The control wafer (sample D) received an additional Si implant with  $1 \times 10^{15} \text{ cm}^{-2}$  at 30 keV, ensuring amorphization in the near surface region. Finally, all the wafers received the same B implant, with dose of  $2 \times 10^{14} \text{ cm}^{-2}$  at 10 keV. Since the Si PAI and the final B implant are identical for all wafers, the Ge implant dose is the only variable in the implant sequence. The full implant sequence is listed in table 4-1.

The dopant profiles, their relative positions as well as the initial *a/c* interface position are illustrated in Fig. 4-1. The following figure (Fig. 4-2) shows amorphous layer depth as determined by XTEM, courtesy of Antonio Saavedra. These images confirm that the two-step amorphization formed a continuous amorphous layer extending from the surface, as opposed to a buried amorphous layer.

Anneals were performed at temperatures of 700 and 825°C in inert N<sub>2</sub> ambient. An AG Associates Heat Pulse 210T Rapid Thermal Annealer (RTA) was utilized for anneals shorter than 15 minutes, with a 125°C/s ramp up rate. Anneals exceeding 15 minutes were conducted in a Thermolyne quartz tube furnace.

Sample A, which received the  $4 \times 10^{15} \text{ cm}^{-2}$  Ge implant, was subjected to the annealing conditions at the same time as the control samples. Fig. 4-3 and 4-4 show the B profiles during the 700°C and 825°C anneals, respectively. The interesting feature of

these figures is the increase in the profile peak. The increase and the shift of the peak seem to occur closer to surface and also closer to the Ge implanted region. The time dependence suggests the phenomena is associated with TED, as the increase stops approximately at the same time as the control sample profiles cease motion. One could, therefore, presume a  $\text{Ge}_x\text{B}_y\text{I}_z$  cluster might be responsible for such a behavior.

Before delving into that hypothesis too much, there are additional measurements one must take into account.

At a later stage of the experiment, the active dose measurements via Hall effect consistently failed to get the expected carrier type on Ge implanted samples. Several Hall-van der Pauw measurements are listed in table 4-2, to illustrate the situation.

Having the n-type silicon formed by Si PAI, Ge and B implant required an explanation. One possibility was that the EOR damage in the depletion region, known to serve as recombination centers, could be increasing the leakage current into the bulk. The electrons in the bulk can offset the measurement, even yielding incorrect carrier type. Hence the measurement is conducted at  $\sim 100\text{K}$  to prevent carriers from populating mid-bandgap traps [Jai03] and subsequently recombining. In this particular case, the carrier type detected remained unchanged. The possibility of surface contamination was discounted based on the fact that the carrier type in the control samples was consistently detected as holes. Since samples A and D were handled in the same manner, annealed in the same furnace/RTA, mostly at the same time, it would be difficult to expect only one set of samples to get contaminated in the process.

The last two rows in the table show the net electrons present even after a very large thermal budget, unexpected considering the SIMS profiles of smaller thermal. At this

point, the implant provider hinted that the implant was not specifically a  $^{74}\text{Ge}$  isotope. Furthermore, that the mass spectrometry aperture was open wide to let three Ge isotopes ( $^{70}\text{Ge}$ ,  $^{72}\text{Ge}$ , and  $^{74}\text{Ge}$ ) from the source reach the target. Providing the next element in atomic weight is  $^{75}\text{As}$ , a donor in silicon, this suggested there might be a slight problem with the experiment.

Figure 4-5 shows the As presence in all the samples implanted with Ge. The samples designated to receive  $4 \times 10^{15}$ ,  $1.2 \times 10^{15}$ , and  $4 \times 10^{14} \text{ cm}^{-2}$  doses of Ge, also received the  $3.3 \times 10^{14}$ ,  $5.75 \times 10^{13}$  and  $2.15 \times 10^{13} \text{ cm}^{-2}$  doses of As. Having the As projected range and distribution similar to that of Ge would suggest the contamination from the source, or non-discriminant mass spectrometry.

The evolution of the B profiles for the experimental control (no Ge implant), sample D, during the  $700^\circ\text{C}$  and  $825^\circ\text{C}$  anneals are shown in Fig. 4-6 and 4-7. The as-implanted condition was added to the figures for comparison. It is evident that the profiles exhibit profile broadening consistent with TED. Also, there appears to be no immobile portion of the B profile, generally associated with the presence of boron-interstitial clusters (BICs). This further asserts that the experimental conditions allow for the investigation of Ge and B interaction, without an eventual interference from other clustering processes. Other interesting features of these profiles include the slight motion of the profile peak towards the surface, and the B surface spike. While the assumed reflective boundary at the surface might account for some of the profile peak shift, one would not expect a significant dip to still exist between the surface and the profile peak by the time the depth of the peak shift is observed. As for the B surface spike in the secondary ion mass spectrometry (SIMS) measurement, it is presumed to be due to the

transition between the oxide and the silicon matrix. It is considered to be an artifact and not related to the possibility of B presence in the thin native oxide or at the interface.

However, looking at the figures 4-6 and 4-7, one can observe the steady increase of the surface spike width with annealing time. All the SIMS measurements were performed under the same conditions, so the artifact should not change on that account.

Interestingly, this does not occur with the Ge implanted samples (Fig. 4-3 and 4-4). In sample A, the B surface spike width does not increase with annealing time.

The surface spike raises the question of the dose conservation, and the possible need to normalize the measured profiles, both for comparison between the measured and simulated profiles. Table 4-3 compares the total dose measured by SIMS to the dose when the surface spike (first 7nm) is ignored, and provides the ratio between the two. Taking the “artifact only” presumption would imply the SIMS dose error would result in a standard deviation of 11.1%, as opposed to the 2.95% when assuming the surface spike is actually B. The trend of dose decreasing with annealing time when ignoring surface spike is another argument against the “artifact only” assumption, as no such trend exists when entire profile is integrated. Again, these differences do not occur in sample A to that extent, as shown in table 4-4.

#### **4.1.2 Simulations**

Initial simulations of control sample anneals (Fig 4-8) indicated a problematic mismatch in the profile shape, peak magnitude, junction depth and surface spike. This would suggest the bulk enhancement factor and surface phenomena might not be properly modeled.

The profile broadening appears excessive, reducing the peak magnitude and spreading the profile more into the bulk. The convoluted profile is the simulated B profile

convoluted with an exponential function with a decay length of 3nm. The decay length was extracted from the slope of the surface peak, presuming it due to the almost a  $\delta$ -function of B at the interface or in the native oxide layer. It is interesting to note the simulation fails to match the surface spike for the longer anneal times, although the surface concentration of B in silicon is not very far off the measured values. Also, if the B surface spike were entirely due to the segregation of B into the oxide, it would not be increasing at longer times. After 2 minutes, the concentration of B in the near surface region, presumably at the surface as well, is declining due to diffusion into the bulk. Therefore, one would expect the surface spike to decrease in concentration, or stay the same for longer anneal times.

Leaving aside the surface phenomena for a moment, one might attempt to match the enhanced diffusion by reducing the enhancement factor. That would reduce the effective diffusion of B, possibly providing a better match to the measured profiles. Having reduced the enhancement factor (C311 BindI), previously calibrated on the {311}'s defect dissolution and enhanced diffusion of B marker layers by a factor of 5, the resulting simulated profiles are shown in Fig. 4-9.

The reduction in the enhancement factor does facilitate a better agreement between the simulated and the measured profiles, namely being closer on the diffusion into the bulk. However, it does not match the profile shape or the surface peak much better than in Fig. 4-8. The slight shift of the profile peak towards the surface does not occur in the simulation until the profile between the peak and the surface becomes completely flat. As for the surface peak, these simulations do not match the surface spike at any point in

time. Rather, the surface spike is shallower than measured value for a given concentration.

One might consider the possibility of trapping of B on the surface, or the oxide/silicon interface. The interface trap density of  $2 \times 10^{14} \text{ cm}^{-2}$  was taken from Voung et al. [Vou96], previously used to explain threshold voltage shifts in pMOS devices.

The simulations seem to match the measured profile reasonably well, once the BI pair trapping on the surface is included. This trapping mechanism facilitates the continuous widening of the surface spike, but affects the overall profile shape. The trapping of the BI pair at the interface parallels the same process for self-interstitials, increasing the removal rate of excess interstitials. The additional recombination mechanism for interstitials at the oxide/silicon interface increases the gradient of interstitial towards the surface, assisting the BI pair traps at the interface in shifting the profile peak towards the surface. This is visible when comparing the Fig. 4-9 and 4-10, for diffusion times from 1 to 4 minutes.

Simulating the annealing of sample A and assuming the interaction of Ge and B negligible compared to the electric field effects, results in profiles seen in Fig. 4-11.

#### **4.2 Boron Segregation to the EOR Loops**

An additional experiment was performed to further examine the interaction of B with the oxide/silicon interface and EOR loops. The use of highly doped p-type wafers simplifies the experiment, as there is no need for B implant. The presence of B in the EOR loop layer shows an increase of B concentration in the loop layer, modeled by the capture of BI pair on the EOR loops.

### 4.2.1 Experimental

The wafers used were float-zone (FZ) p-type Si <100> wafers, resistivity  $\sim 0.02$  m $\Omega$ cm, with the concentration of B  $\sim 4 \times 10^{18}$  cm $^{-3}$ . Both of these values were confirmed via four-point probe measurement and SIMS, respectively. Both wafers received a Si  $1 \times 10^{15}$  cm $^{-2}$  implant at 100keV, with liquid nitrogen cooling. The control wafer (samples E1) received an additional Si  $1 \times 10^{15}$  cm $^{-2}$  implant at 30keV to ensure the continuous amorphous layer, while the Ge implanted wafer (samples E2) received a Ge  $4 \times 10^{15}$  cm $^{-2}$  at 30keV. The samples were annealed at 750°C for duration of 1 and 4 hours, and at 825°C for 1 and 4 minutes.

Figures 4-12 and 4-13 show the boron profiles of sample E1 annealed at 750 and 825°C, respectively. The profiles exhibit an increase below 0.2 $\mu$ m, indicative of the B trapping on the EOR loop layer. Also, there is a broadening and an increase in magnitude of the B surface spike, coming from the B trapping at the oxide/silicon interface. The dip in the otherwise flat B profile near the surface is the consequence of the B segregation to the oxide and the oxide/silicon interface.

### 4.2.2 Simulations

The phenomenon observed in the sample E1 is associated with the capture of B at the oxide/silicon interface and the EOR loops. Assuming the characterization of the former from the earlier parts of this chapter is adequate, a capture reaction on the boundaries of the EOR loops is added (after Xia et al. [Xia99]). The reaction rate is assumed to be diffusion limited along the circumference of the loop, as shown in Eq. 4-1 and 4-2. The BI represents the mobile boron-interstitial pair concentration, with  $D_{BI}$  as its

diffusivity. The  $R_{Loop}$  and  $D_{Loop}$  are average radius and the loop density, and the  $B_{Loop}$  is the concentration of B trapped in the loop.

$$k_f = 4 \cdot \pi \cdot a_{Si} \cdot D_{BI} \quad (4-1)$$

$$\frac{\partial B_{Loop}}{\partial t} = k_f \cdot BI \cdot 2 \cdot \pi \cdot R_{Loop} \cdot D_{Loop} \quad (4-2)$$

The simulated and SIMS measured profiles of the sample E1 are compared in the Fig. 4-14 and 4-15.

In the Fig. 4-14 and 4-15, one can observe a relatively good match for the surface spike broadening and the B profile dip near the surface. The capture on the EOR loops has certain discrepancies from the experimental data. From the experimental data, it would seem the capture is symmetric around the loop layer and shallower than predicted by the model. The modeled capture does not have the same symmetry, since the simulated loop density decays more gradually towards the bulk. Therefore, even though the captured B provides a dip and a sharp increase on the shallower side, it is not possible to get the same (Fig. 4-12) or even deeper dip (Fig. 4-13) on the deeper side of the segregated peak. The lower densities of EOR loops capture B preventing the formation of the observable dip in the region deeper than the former  $a/c$  interface. Despite these differences, the capture model does provide a reasonable match.

### 4.3 Conclusions

An experiment is designed to investigate the Ge and B interaction in preamorphized silicon. The Si preamorphization provides the interstitial supersaturation, as well as significantly reduces the formation of BICs, thus simplifying the diffusion of B in the control samples.

Nonetheless, B profiles in the control samples diffused slower than the available models predicted. The simultaneous B dose loss in the bulk and the broadening of the surface spike, usually considered a SIMS measurement artifact, indicated a possibility of B trapping at the oxide/silicon interface. Including an equation to describe the trapping of a BI pair at the interface yielded improved fits, both in the near surface region and the bulk diffusion. These improved fits were achieved without changes to the other models.

Also, the phenomenon of B segregation to EOR loop layer is observed in the Si preamorphized, highly doped p-type wafer. Modeling this phenomenon through a BI pair capture at the circumference of the loop provides a qualitative fit to the experimental data.

Table 4-1. Sample labels and implant sequence, showing Ge implant dose as the only variable in the sequence

Sample	Si implant	Ge implant	B implant
A	$1 \times 10^{15} \text{ cm}^{-2}$ , 100 keV, LN2	$4 \times 10^{15} \text{ cm}^{-2}$ , 30 keV	$2 \times 10^{14} \text{ cm}^{-2}$ , 10 keV
B	$1 \times 10^{15} \text{ cm}^{-2}$ , 100 keV, LN2	$1.2 \times 10^{15} \text{ cm}^{-2}$ , 30 keV	$2 \times 10^{14} \text{ cm}^{-2}$ , 10 keV
C	$1 \times 10^{15} \text{ cm}^{-2}$ , 100 keV, LN2	$4 \times 10^{14} \text{ cm}^{-2}$ , 30 keV	$2 \times 10^{14} \text{ cm}^{-2}$ , 10 keV
D	$1 \times 10^{15} \text{ cm}^{-2}$ , 100 keV, LN2 $1 \times 10^{15} \text{ cm}^{-2}$ , 30 keV	none	$2 \times 10^{14} \text{ cm}^{-2}$ , 10 keV

Table 4-2. Active dose and carrier type measured by Hall-van der Pauw system

Sample	Annealing conditions	Hall temperature [K]	Active dose [ $\text{cm}^{-2}$ ]	Carriers
Ge implanted	15m@700C	300	$1.67 \times 10^{14}$	e-
Ge implanted	15m@700C	100	$3.95 \times 10^{14}$	e-
Ge implanted	4h@700C	300	$8.48 \times 10^{13}$	e-
Ge implanted	4h@700C	100	$1.73 \times 10^{14}$	e-
Control	15m@700C	300	$2.78 \times 10^{14}$	h+
Control	4h@700C	300	$2.23 \times 10^{14}$	h+
Ge implanted	15s@825C	300	$7.13 \times 10^{13}$	e-
Control	15s@825C	300	$1.39 \times 10^{14}$	h+
Ge implanted	8m@825C	300	$3.89 \times 10^{13}$	e-
Control	8m@825C	300	$2.02 \times 10^{14}$	h+
Ge implanted	8m@825C, 20s@1100C	300	$4.56 \times 10^{13}$	e-
Ge implanted	8m@825C, 2h@1100C	300	$3.26 \times 10^{14}$	e-

Table 4-3. Integrated dose from the measured B profiles in the control sample annealed at 825°C, taking full profile (Q<sub>1</sub>) and ignoring the surface spike (Q<sub>2</sub>)

Annealing conditions	SIMS integrated dose Q <sub>1</sub> [cm <sup>-2</sup> ]	SIMS integrated dose Q <sub>2</sub> [cm <sup>-2</sup> ], x>7nm	Ratio (Q <sub>2 reference</sub> /Q <sub>2</sub> )
as-implanted	1.67x10 <sup>14</sup>	1.58x10 <sup>14</sup>	1.03
15s@825C	1.78x10 <sup>14</sup>	1.63x10 <sup>14</sup>	1 (reference)
30s@825C	1.79x10 <sup>14</sup>	1.60x10 <sup>14</sup>	1.02
1m@825C	1.82x10 <sup>14</sup>	1.60x10 <sup>14</sup>	1.02
2m@825C	1.75x10 <sup>14</sup>	1.44x10 <sup>14</sup>	1.13
4m@825C	1.80x10 <sup>14</sup>	1.30x10 <sup>14</sup>	1.25
8m@825C	1.73x10 <sup>14</sup>	1.21x10 <sup>14</sup>	1.34
$\bar{Q}$ [cm <sup>-2</sup> ]	1.77x10 <sup>14</sup>	1.49x10 <sup>14</sup>	
$\sigma$ [cm <sup>-2</sup> ]	5.21x10 <sup>12</sup>	1.65x10 <sup>13</sup>	
$\sigma/\bar{Q}$ [%]	2.95	11.1	

Table 4-4. Integrated dose from the measured B profiles in the  $4 \times 10^{15} \text{ cm}^{-2}$  Ge implanted sample annealed at  $825^\circ\text{C}$ , taking full profile ( $Q_1$ ) and ignoring the surface spike ( $Q_2$ )

Annealing conditions	SIMS integrated dose $Q_1$ [ $\text{cm}^{-2}$ ]	SIMS integrated dose $Q_2$ [ $\text{cm}^{-2}$ ], $x > 7\text{nm}$	Ratio ( $Q_2$ reference/ $Q_2$ )
as-implanted	$1.88 \times 10^{14}$	$1.61 \times 10^{14}$	1.1
15s@825C	$2.03 \times 10^{14}$	$1.77 \times 10^{14}$	1 (reference)
30s@825C	$2.01 \times 10^{14}$	$1.76 \times 10^{14}$	1
1m@825C	$1.87 \times 10^{14}$	$1.65 \times 10^{14}$	1.08
2m@825C	$1.88 \times 10^{14}$	$1.65 \times 10^{14}$	1.07
4m@825C	$1.82 \times 10^{14}$	$1.58 \times 10^{14}$	1.11
8m@825C	$1.88 \times 10^{14}$	$1.66 \times 10^{14}$	1.07
$\bar{Q}$ [ $\text{cm}^{-2}$ ]	$1.91 \times 10^{14}$	$1.67 \times 10^{14}$	
$\sigma$ [ $\text{cm}^{-2}$ ]	$7.81 \times 10^{12}$	$7.23 \times 10^{12}$	
$\sigma/\bar{Q}$ [%]	4.09	4.32	

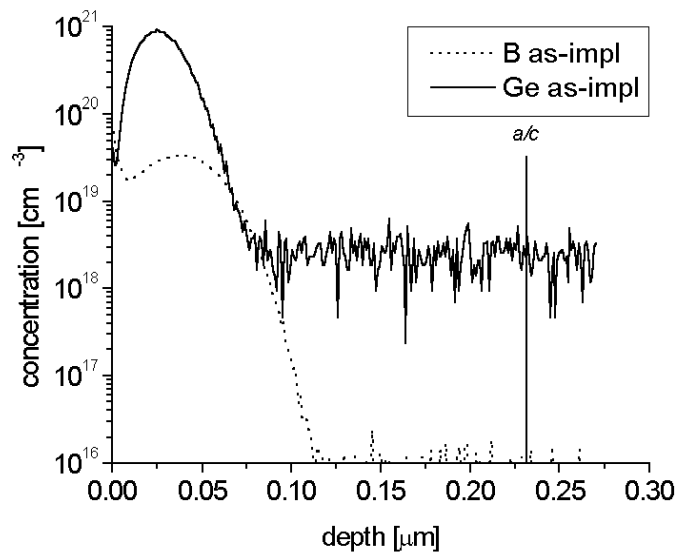


Figure 4-1. Profiles of B and Ge in as-implanted sample A

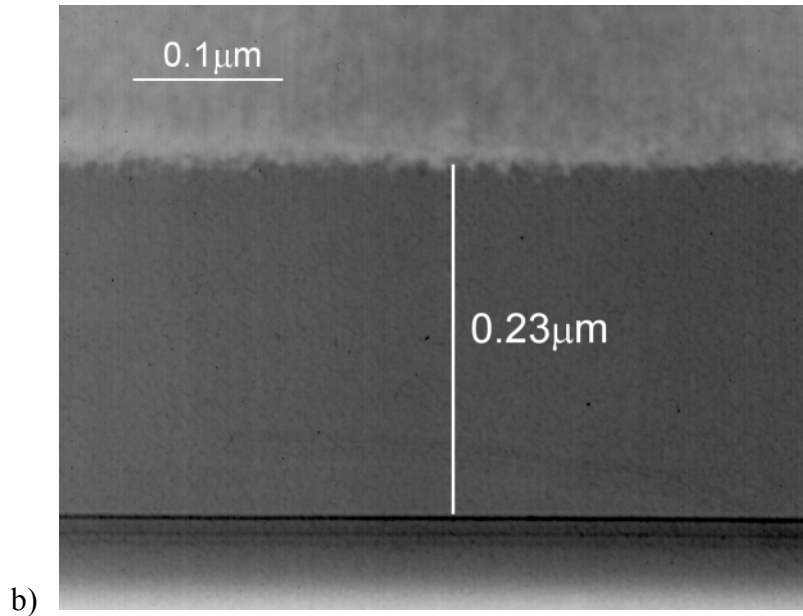
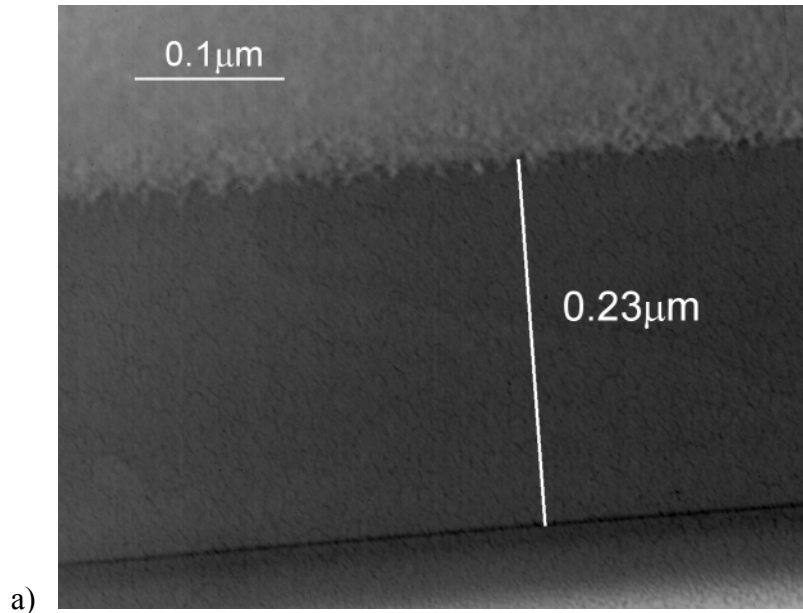
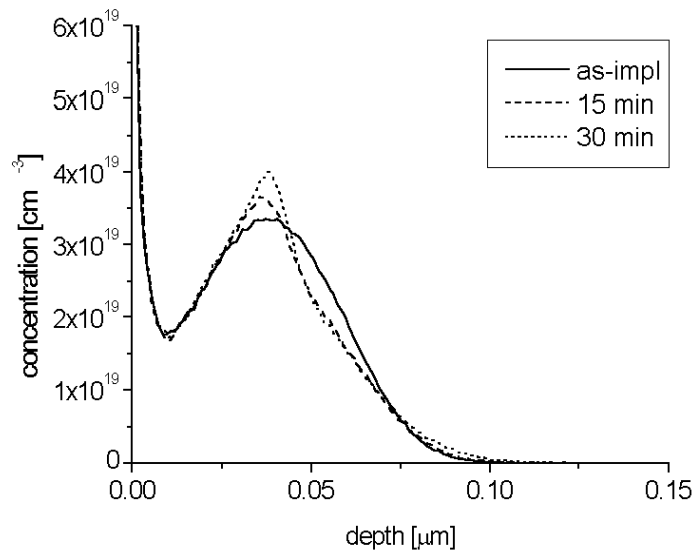
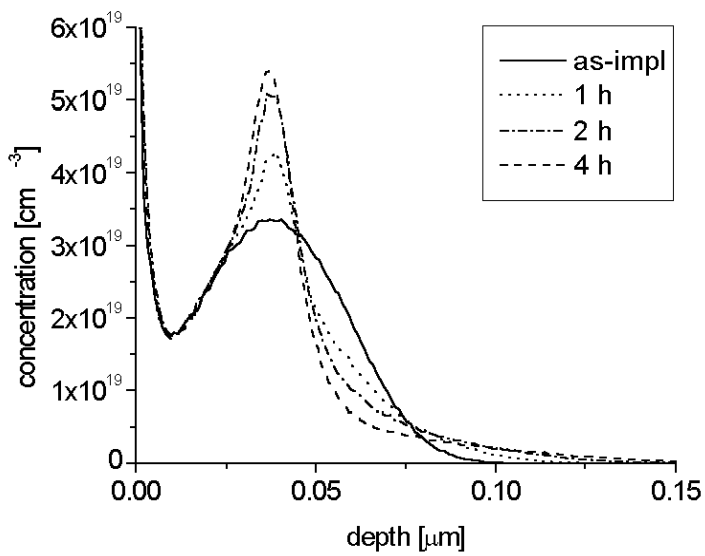


Figure 4-2. Cross-section TEM (XTEM) images of samples (a) A and (b) D under 100000 magnification

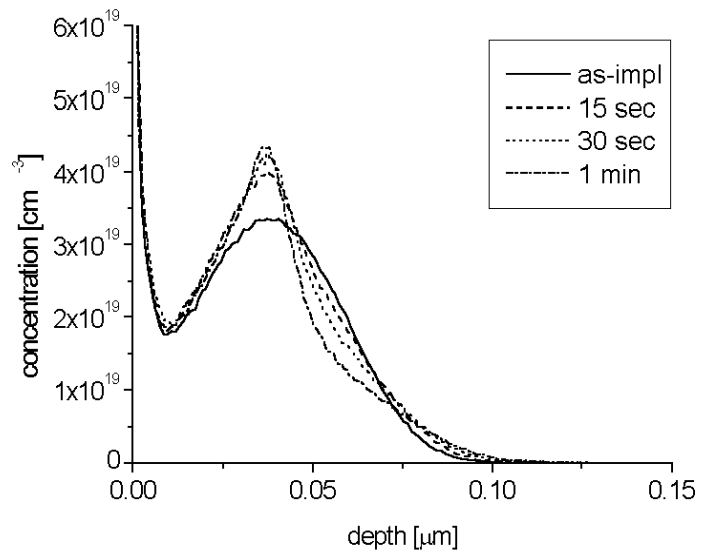


a)

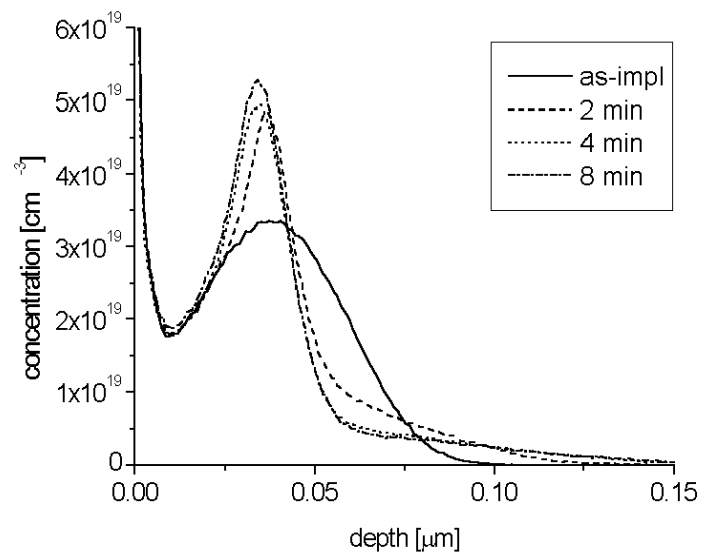


b)

Figure 4-3. B profiles from Ge implanted samples during annealing at 700°C



a)



b)

Figure 4-4. B profiles from Ge implanted samples during annealing at 825°C

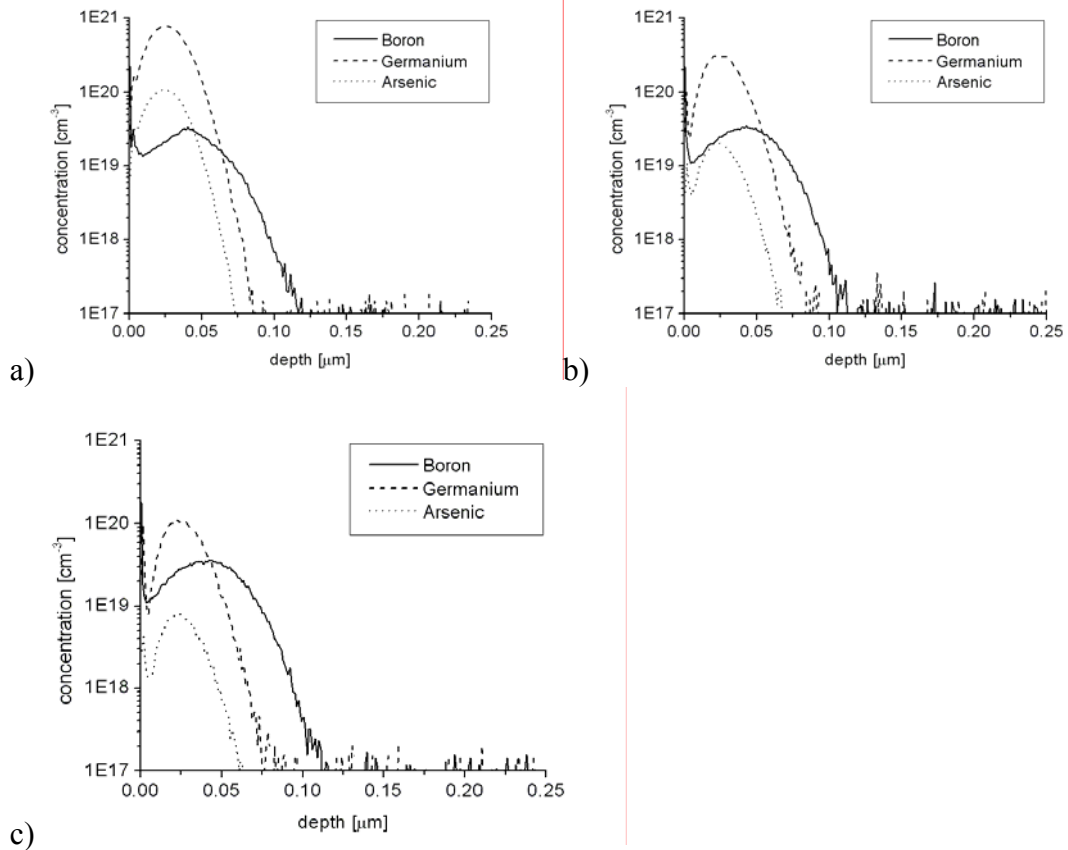
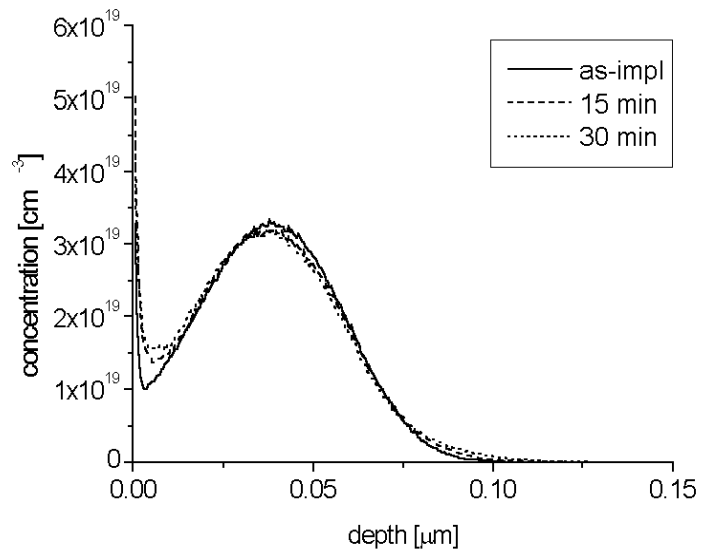
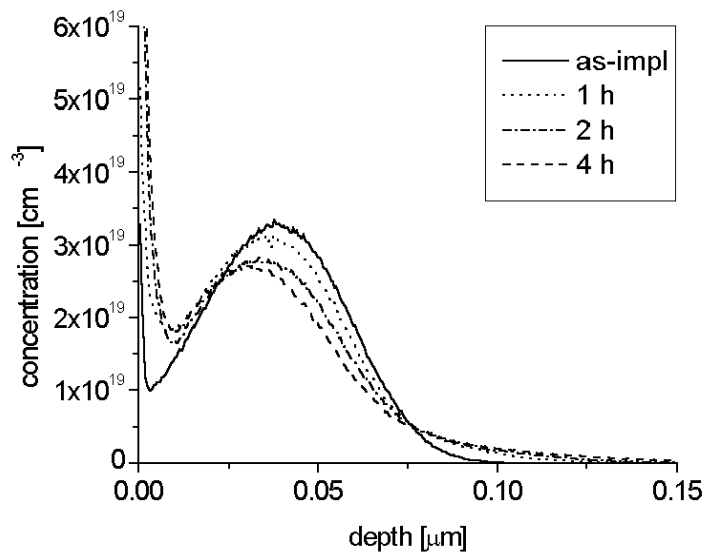


Figure 4-5. SIMS profiles of Ge, As and B in samples: A, with  $4 \times 10^{15} \text{ cm}^{-2}$  Ge (1min@825°C), B with  $1.2 \times 10^{15} \text{ cm}^{-2}$  Ge (as-implanted) and C with  $4 \times 10^{14} \text{ cm}^{-2}$  Ge (as-implanted) per figure a, b, c, respectively

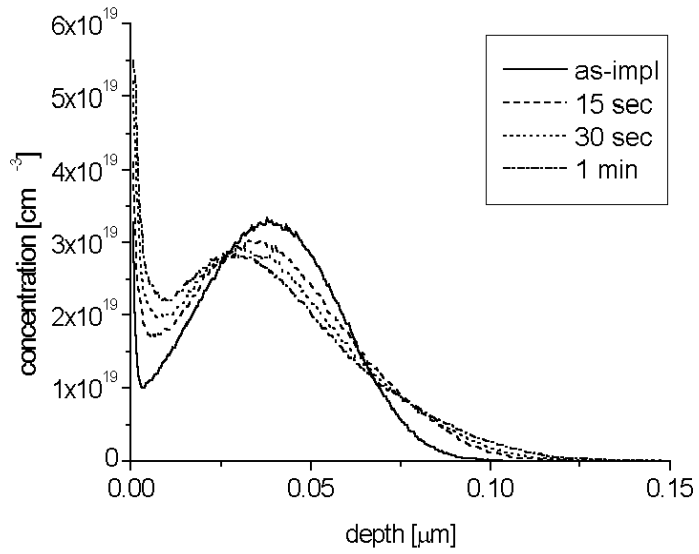


a)

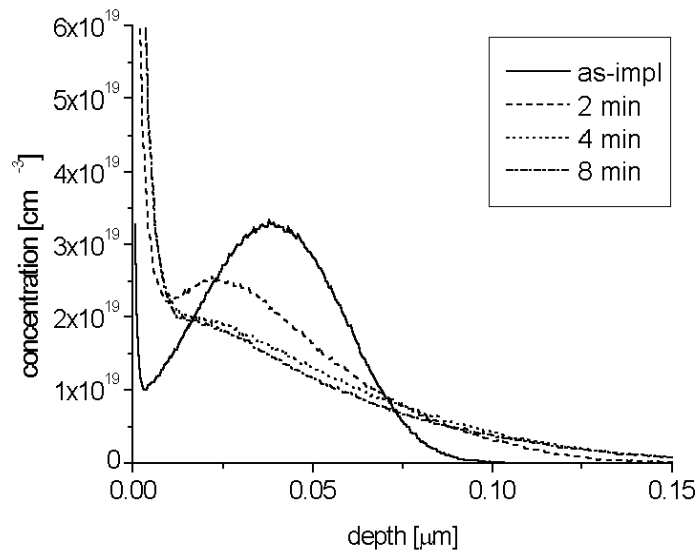


b)

Figure 4-6. B profiles from control sample during annealing at  $700^\circ\text{C}$



a)



b)

Figure 4-7. B profiles from control sample during the annealing at  $825^\circ\text{C}$

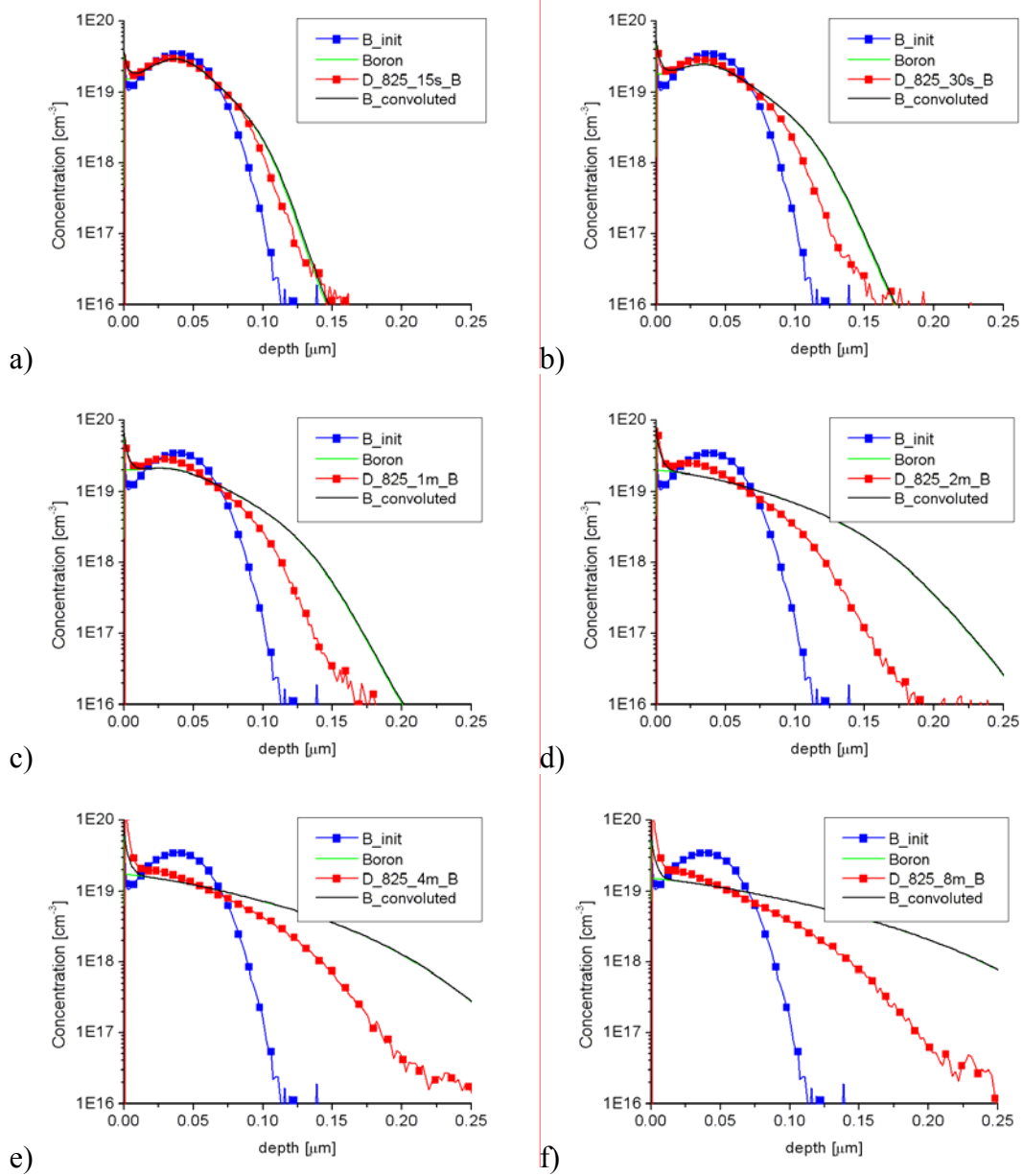


Figure 4-8. Simulated B profiles of control sample during anneals at 825°C

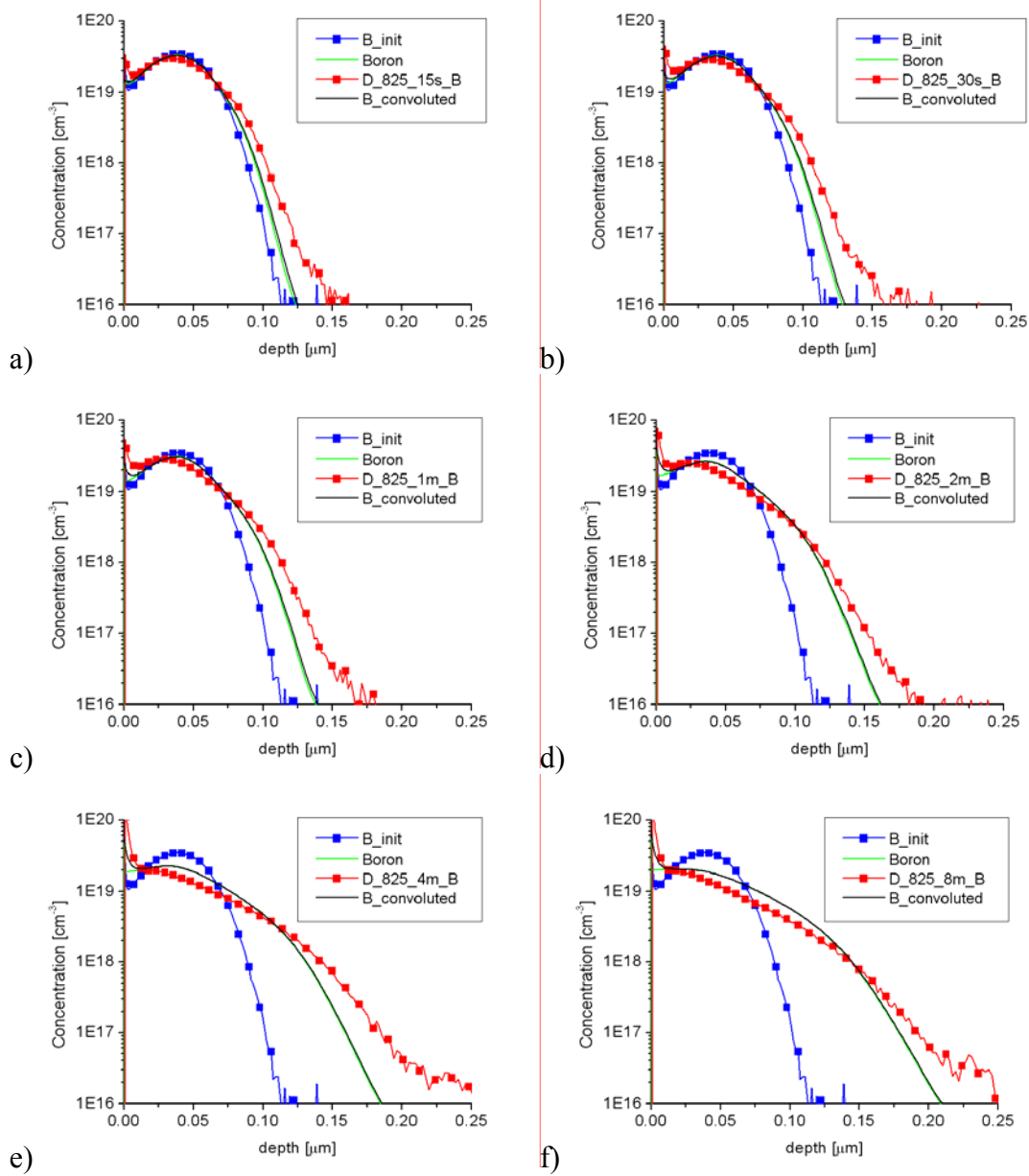


Figure 4-9. Simulated B profiles of control sample during anneals at  $825^{\circ}\text{C}$ , diffusion enhancement factor reduced five times

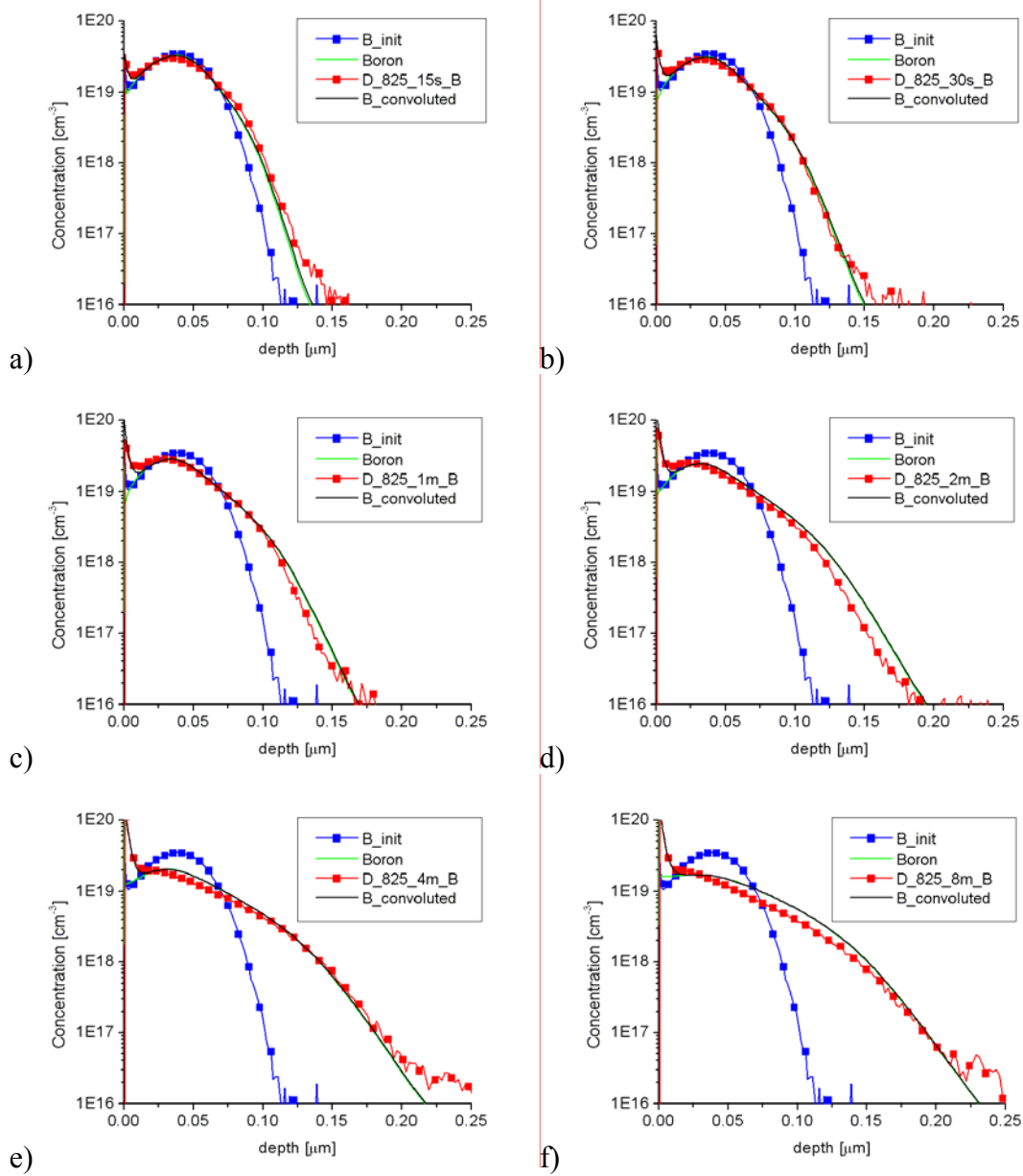


Figure 4-10. Simulated B profiles of control sample during anneals at 825°C, assuming surface trapping of BI

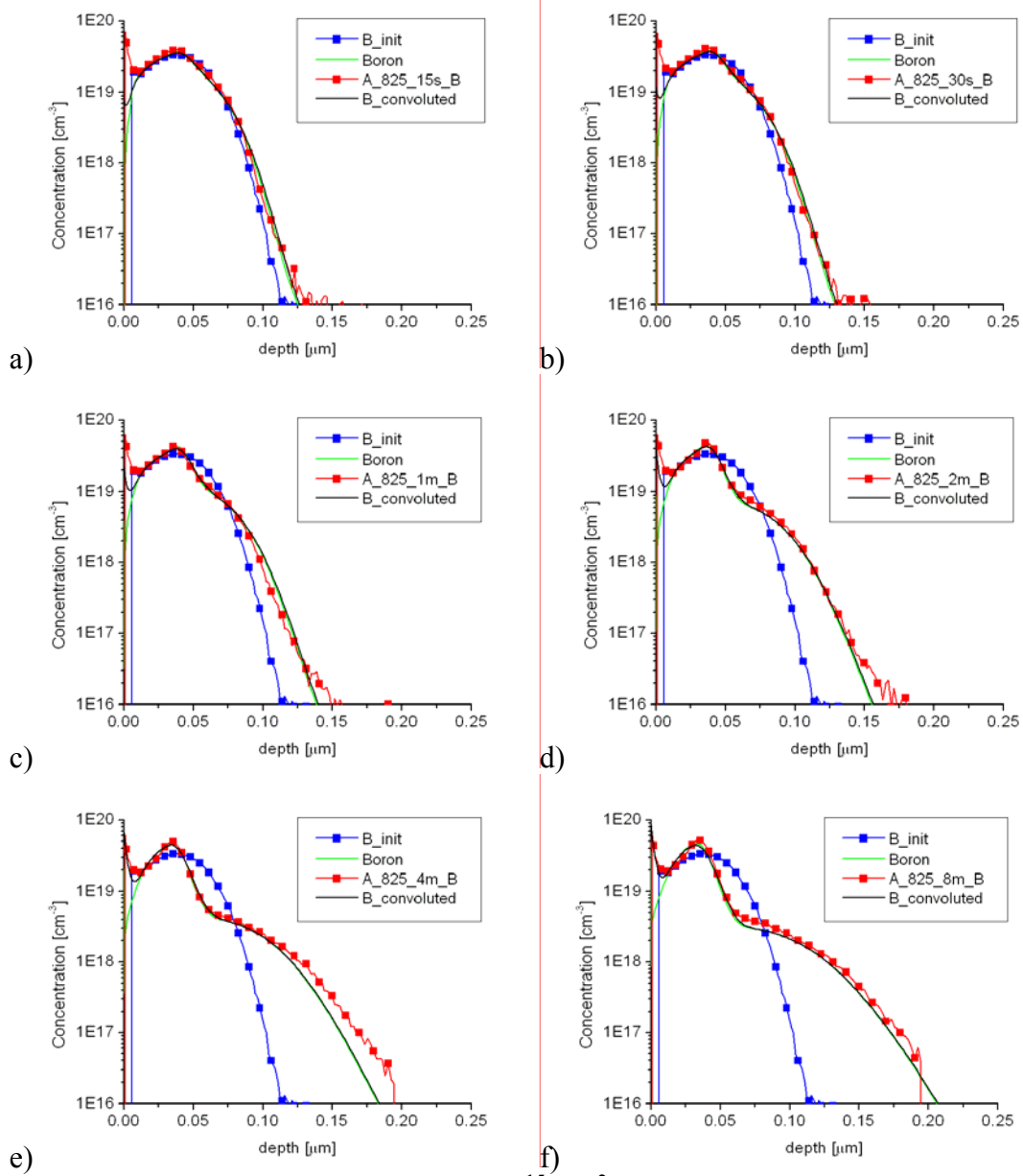


Figure 4-11. Simulated B profiles of  $4 \times 10^{15} \text{ cm}^{-2}$  Ge implanted sample (As contaminated) during anneals at  $825^\circ\text{C}$ , assuming electric field effect dominant

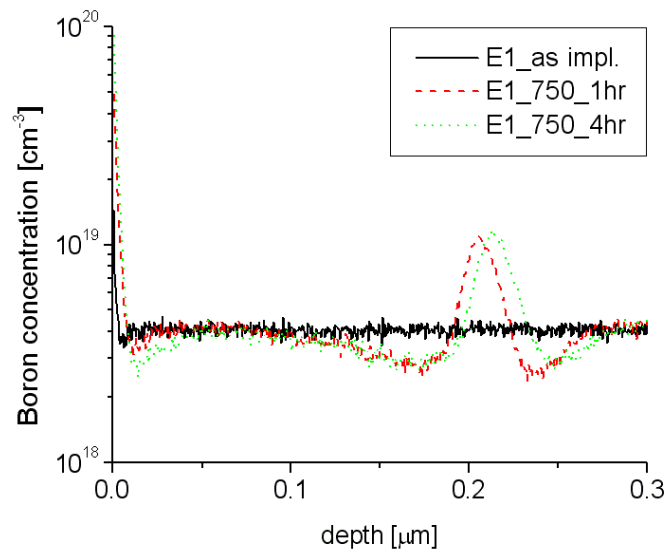


Figure 4-12. B profiles from sample E1 during annealing at 750 °C

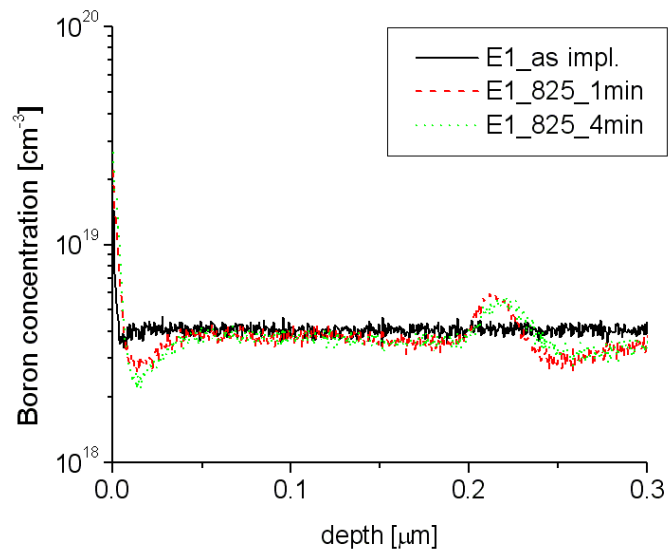
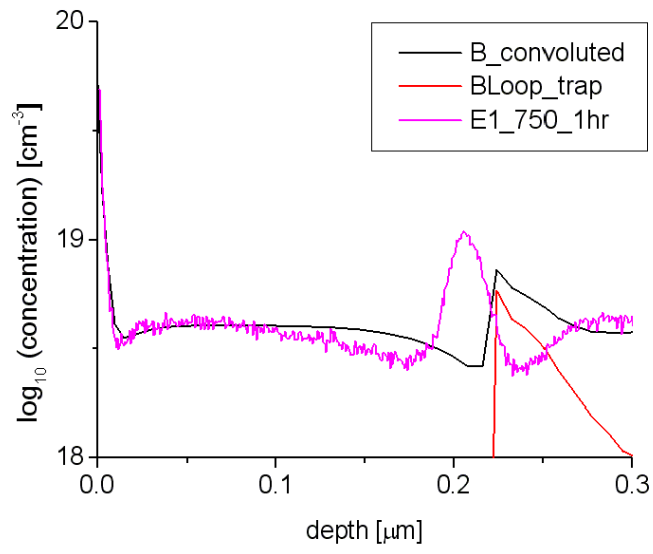
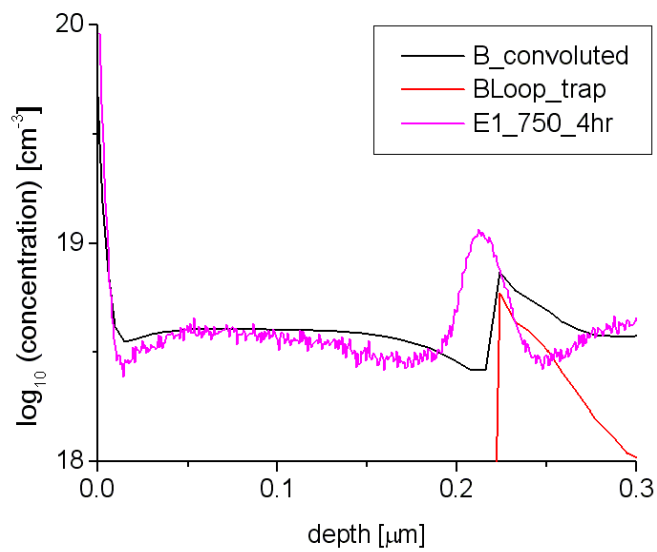


Figure 4-13. B profiles from sample E1 during annealing at 825°C

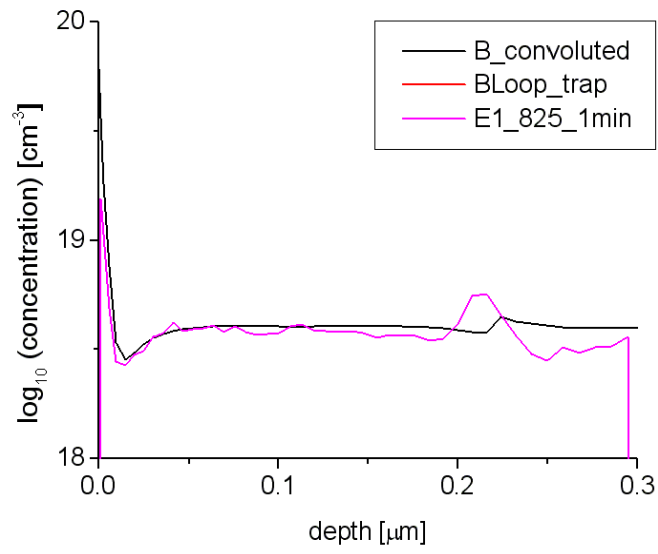


a)

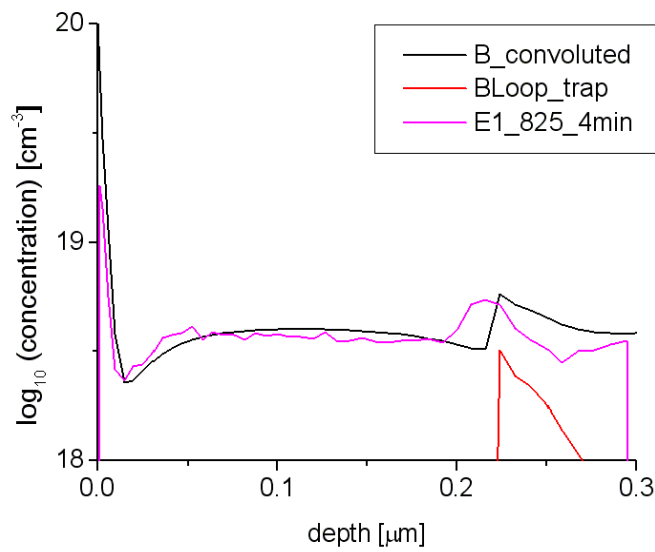


b)

Figure 4-14. Simulated B profiles of B segregation to the loops in sample E1 during annealing at 750°C



a)



b)

Figure 4-15. Simulated B profiles of B segregation to the loops in sample E1 during annealing at 825°C

## CHAPTER 5

### BORON INTERACTION WITH GERMANIUM UNDER INTERSTITIAL SUPERSATURATION

#### Overview

This chapter provides an overview of the earlier model of Lever et al., as well as an experiment used in attempt to extract parameters for the model. The experiment is designed to observe the B and Ge interaction in the high interstitial supersaturation environment to maximize an eventual reaction product. Upon implanting Ge and B, during a subsequent anneal Ge seems to be slowing down B diffusion and retaining higher B concentrations when compared to control samples. Modeling this behavior through Ge-B pairing mechanism provides a reasonable fit to the experimental data.

#### **5.1 Prior Work - Model Implementation**

In an effort to model B diffusion in lower Ge contents, the model of Lever et al. [Lev98] is utilized in the experimental design. However, some changes are required, in order to account for phenomena such as bandgap narrowing and transient enhanced diffusion (TED).

##### **5.1.1 Bandgap Narrowing**

Germanium content can vary as a function of depth, which means the bandgap narrowing is a function of depth as well. This requires a slight change in the potential equation, which treats bandgap,  $E_G$  and intrinsic carrier concentration,  $n_i$  as a function of temperature, but not as a spatial variant. Adding the  $E_G$  and  $n_i$  terms allows for a change with respect to depth, or any other axis. Solving the Poisson equation with a spatially

varying bandgap and considering the Fermi level influence on diffusion accounts for the quasi-electric field effects. Although the bandgap narrowing due to the Ge presence provides some segregation of B into Ge rich layers, it is not enough to account for the experimentally seen increases in B concentration.

Lever et al. followed Kuo [Kuo93], in referencing People's [Peo85] calculation in determining the bandgap change. Their results are in agreement with data of Lang [Lan85], Dutartre [Dut91] and Robbins [Rob92]. In particular, the expressions of Weber et al. [Web89] and Dutartre [Dut91] are employed for the bandgap of relaxed and strained layers, respectively. Conduction and valence band densities of state are assumed not to change significantly.

### 5.1.2 Boron Diffusion in Si and Interaction with Ge

It is well established that B diffuses almost exclusively through interaction with silicon interstitials [See68][Fah85][Fan96][Gos97][Ura99b]. Furthermore, there is a concentration dependence of diffusion, which is modeled as diffusion through the interaction with neutral and charged interstitials. Since the Poisson equation has taken into account the spatial variance of the Ge concentration, its effects on the diffusion of neutral and negatively charged BI pairs are already considered in the Fermi level dependent diffusivity.

$$-J_{BI} = \left( D_{BI0} + D_{BIp} \frac{p}{n_i} \right) \frac{1}{p/n_i} \frac{\partial \left( BI \cdot \frac{p}{n_i} \right)}{\partial x} \quad (5-1)$$

$$-J_{BI} = \left( D_{BI0} + D_{BIp} \frac{p}{n_i} \right) \frac{1}{p/n_i} \left( \frac{\partial BI}{\partial x} + BI \frac{\partial \ln \frac{p}{n_i}}{\partial x} \right) \quad (5-2)$$

$$\frac{\partial \ln P/n_i}{\partial x} = \frac{\partial \ln p}{\partial x} - \frac{\partial \ln n_i}{\partial x} \quad (5-3)$$

Further divergence from the model of Lever et al. includes changes to the clustering reaction. The original model considers B as a diffusing species, which is replaced by a BI pair diffusion. The modified model assumes a reaction is occurring between a BI pair and a Ge atom, such that a GeBI complex is formed. The GeBI complex can then release an interstitial forming a GeB pair. Alternatively, it can release a BI pair returning to the initial Ge configuration. The original work of Lever et al. suggests that GeB pairing occurs as a consequence of microscopic strain relaxation. Due to lack of an alternative explanation of the GeB pairing phenomena that Lever's model describes, this work is continued under the same presumption.



## 5.2 Experiment Design and Considerations

This section discusses the experiment designed to investigate Ge influence on B diffusion under transient enhanced diffusion (TED) conditions. TED conditions are used to accentuate the eventual difference in B diffusion with and without Ge present in the material. In case a difference in the profile evolution is observed, that would discern any doubt of the existence of GeB pair, and might offer some insight into its properties.

In order to investigate the influence of Ge on B diffusion, all other parameters involved should be invariant of experimental conditions. One of the problems in the experiment design is that B is known to form boron-interstitial clusters (BICs) upon

implant into a crystalline silicon and subsequent annealing [Mic87][Sto95]. This should be avoided in order to increase the probability of a B atom reacting with a Ge atom, versus another B atom or silicon self-interstitials. One way to reduce the formation of BICs is to amorphize the surface silicon layer prior to a B implant. The work of Jones et al. [Jon96a] showed BICs do not form in thick amorphous layers, yet B experiences enhanced diffusion.

Germanium is a popular choice as an amorphization species. It is an isovalent chemical element in the silicon lattice; its crystal lattice is 4.2% larger crystal lattice than that of silicon, and it amorphizes silicon at lower implant doses due to its larger mass. Although there are a number of studies on the effect of Ge pre-amorphizing implant (PAI) on B diffusion, these investigations are generally directed towards junction formation and have varying doses of Ge PAI. This allows for investigations of different initial amorphous layer depths and end of range (EOR) damage, which may be influencing the B diffusion behavior and its reaction with Ge. However, this precludes the extraction of parameters that determine the Ge-B interaction.

Considering the goal of this study is to investigate the interaction of Ge and B, initial conditions should be invariant of different Ge and B implant conditions. The amorphous/crystalline (*a/c*) interface should be defined by an implant common for all the samples in the experiment. Using silicon PAI for the formation of the amorphous layers has several benefits. First, the Si PAI creates an amorphous layer without the introduction of dopants. Secondly, the Si PAI allows the *a/c* interface to be positioned independently of the other implants. Thirdly, if the damage profiles of the other implants are contained within the amorphous layer created by the Si PAI step, those implants will not contribute

to the EOR damage. The evolution of the EOR damage and TED during subsequent anneal steps would then solely depend on the Si PAI. Therefore, the Si PAI ensures the independence and invariance of  $a/c$  interface position, EOR damage and TED, with respect to Ge and B implant conditions.

The diffusion enhancement, due to the interstitial supersaturation, is also beneficial for the detection of the product in the reaction described by the Eq. 5-5. For a given interstitial supersaturation, defined as silicon interstitial concentration over the equilibrium interstitial concentration, BI concentration is increased by the same factor (Eq. 5-4). This means more B will be in its mobile form, and available for reaction with Ge, resulting in the increase of the GeBI. Due to the interstitial release in the reaction forming a GeB pair (Eq. 5-6), the increase in the GeBI would not necessarily lead to the increase in a GeB pair concentration.

Initial simulations using the model adopted from Lever et al. [Lev98] indicated the possibility of cluster formation under interstitial supersaturation during TED, without the need for a high Ge content. Hence, an investigation of lower Ge concentrations could be used to verify the existence of the GeB pair. Should the B diffusion depend on Ge implant conditions, it may be possible to probe the binding energy of the cluster by additional anneal steps. Alternatively, it would disprove the existence of a clustering reaction between Ge and B. This would indicate that the diffusion reduction might be caused by other effects, such as strain or interstitial formation energy variation.

### **5.2.1 Experimental Conditions**

Having realized the contamination occurred during the implant (details in Chapter 4.1), the experiment was repeated using new material. The wafers used were float-zone (FZ) p-type Si <100> wafers, with resistivity of 140-180  $\Omega\text{cm}$ . The implant conditions

were identical to the initial experiment from the previous chapter. Specifically, the Si PAI with an implant dose of  $1 \times 10^{15} \text{ cm}^{-2}$  at the energy of 100 keV produced a 0.22  $\mu\text{m}$  thick amorphous layer. Subsequently, one wafer was implanted with Ge dose of  $4 \times 10^{15} \text{ cm}^{-2}$  at 30 keV, labeled sample 2A. The control wafer (sample 2D) received another Si implant with  $1 \times 10^{15} \text{ cm}^{-2}$  at 30 keV, ensuring the continuous amorphous layer. Finally, both wafers received the same B implant, with a dose of  $2 \times 10^{14} \text{ cm}^{-2}$  at the energy of 10 keV. The anneals were performed at the temperature of  $780^\circ\text{C}$  in a RTA furnace under nitrogen flow.

### 5.2.2 Experimental Results

Figure 5-1 shows the as-implanted profiles of the sample 2A (Ge implanted). The amount of As found in the Ge implanted samples were on the order of 0.5%, the same percentage as detected in the Ge standard used for calibration of the SIMS counts. Presuming the Ge standard is not contaminated would lead one to consider the  $^{75}\text{As}$  signal as interference of  $^{74}\text{Ge}+\text{H}$ .

The time dependence of B profile during the  $780^\circ\text{C}$  anneals is shown in Fig. 5-3. Figure 5-3 a) shows B profiles for Ge implanted samples. The profile tail diffuses into the bulk, while the profile peak shifts towards the surface. It is also possible that the profile peak is shifting towards the Ge doped region, to form GeB pair. The profiles in the control samples (Fig 5-3.b) show enhanced diffusion, as a consequence of the  $\{311\}$  defect dissolution in the EOR region. In both these cases, the diffusion enhancement is dropping as one nears the surface, due to the interstitial concentration gradient towards the surface. Figures a) and b) differ mostly in the profile peak and the surface spike. Ge implanted samples seem to shift the profile peak without a significant drop in

concentration, and do not have such a clear increase in the surface spike. Both of these observations could be due to Ge trapping B, retaining a higher B peak concentration, and preventing B from reaching the surface to contribute to the surface spike.

As for the similarities, the junction depth motion in both samples seems parallel. This would indicate a negligible difference in self-interstitial concentration between the Ge implanted and control samples. Therefore, neither Ge diffusing through interaction with interstitials, nor any sort of clustering presents an interstitial sink.

### 5.2.3 Simulations

In attempt to simulate these anneals, one can consider the results of Zangenberg et al. [Zan01]. They reported the increase in activation energy for B diffusion in relaxed  $\text{Si}_{1-x}\text{Ge}_x$  layers of  $\sim 0.5\text{eV}$ , as a weak function of the Ge content. Relating that to the GeB pair, one could infer that the formation energy of GeB pair is similar to the activation energy increase. Based on the similarity of the junction depth during the anneal, the GeBI complex is presumed not to be as significant. Assuming the B diffusion mostly occurs through an interaction with interstitials, forming a BI pair; tying the BI in a GeBI complex would reduce the concentration of the mobile B specie. Macroscopically, it would be observed as the reduction of the effective diffusivity, most notably in the tail region. Since no significant difference in tail diffusion is observed between Ge implanted samples and the control, the concentration of GeBI is assumed to be much lower than that of GeB. This is valid when the binding energy of a BI pair to GeBI is lower than  $2.4\text{eV}$ , and for  $E_{\text{GeB}}^f$  of  $0.5\text{eV}$ , which are the values used in the simulations. The binding energy of the GeBI complex would also be rather difficult to determine, as it is effectively a transient species.

Figures 5-4 and 5-5 show the simulation results for Ge implanted and control samples, respectively. Figure parts a, b, and c correspond to annealing times of 1, 4 and 16 minutes at 780°C.

### **5.3 Constant B Concentration Experiment**

#### **5.3.1 Experimental conditions and results**

To further investigate the properties of the GeB pair, an additional experiment was performed. The wafers used were float-zone (FZ) p-type Si <100> wafers, resistivity  $\sim 0.02 \text{ m}\Omega\text{cm}$ , with the concentration of B  $\sim 4 \times 10^{18} \text{ cm}^{-3}$ . Both of these values were confirmed via four-point probe measurement and SIMS, respectively. The use of highly doped wafers simplifies the experiment, as there is no need for B implant. The implant conditions used were similar to the previous experiments. Both wafers received a Si  $1 \times 10^{15} \text{ cm}^{-2}$  implant at 100keV, with liquid nitrogen cooling. The control wafer (samples E1) received an additional Si implant to ensure the continuous amorphous layer, while the Ge implanted wafer (samples E2) received a  $4 \times 10^{15} \text{ cm}^{-2}$  at 30keV. The samples were annealed under nitrogen flow in Thermolyne quartz tube furnace and AG Associates Heat Pulse 210T Rapid Thermal Annealer (RTA). The anneal times and temperatures were: 750°C for a duration of 1 and 4 hours, and at 825°C for 1 and 4 minutes.

Figures 5-6 and 5-7 show the boron profiles of control samples annealed at 750 and 825°C, respectively. The profiles exhibit an increase below 0.2 $\mu\text{m}$ , indicative of the B trapping on the EOR loop layer. Also, there is a broadening and an increase in magnitude of the B surface spike, coming from the B trapping at the oxide/silicon interface. The dip in the otherwise flat B profile near the surface is the consequence of the B segregation to the oxide and the oxide/silicon interface.

Comparatively, the Ge implanted samples exhibit an increase in the B profile magnitude in the region implanted with Ge, as shown in Fig. 5-8 and 5-9. These samples also show the evidence of B trapping on the EOR loops. Both the increase in the Ge implanted region (upper 50 nm) and the increase in the EOR region is more pronounced at the temperature of 750°C. This could be due to the higher interstitial supersaturation for both regions, as well as the decreasing stability of GeB pair in the Ge implanted region, at the lower annealing temperature. The increase of B concentration in the Ge implanted region confirms there is a mechanism for retaining B in the vicinity of Ge, such as the proposed GeB pair. Wider and higher B surface spike in the control samples, compared to the Ge implanted samples, also serves to confirm the existence of a trapping mechanism which prevents B from reaching the oxide/silicon interface.

A much stronger increase in the B profile at the lower annealing temperature poses several questions. First, would the B profile increase more during an anneal at a lower temperature, such as 600°C? Second, could the increase be forming prior to the regrowth of the amorphous layer? Third, as the increase in the Ge implanted region leaves no B dip around it, could it be that the increase is just a matter of SIMS ionization efficiency as the silicon changes from amorphous to the crystalline phase?

In order to answer these questions, anneals at 560 and 600°C were performed. The times of the 560°C anneals, 45 and 90 minutes, allowed for observation of B profile shortly after the regrowth of the amorphous layer. The resulting B profiles show no difference from the as-implanted condition (Fig. 5-10). Therefore, if the increase of the B profile magnitude in the presence of Ge is a consequence of a change in the SIMS ionization efficiency, it requires a certain time to achieve the proximity between

individual Ge and B atoms in the crystal lattice. Similar conclusions can be drawn from the samples annealed at 600°C (Fig. 5-11), as there is no increase of the B profile in the Ge implanted region up to 90 minutes.

### 5.3.2 Simulations

The phenomena observed in the control samples are associated with the capture of B at the oxide/silicon interface and the EOR loops, as described in chapter 4.

Applying the Ge-B pairing model, described earlier in this chapter, with the same parameter set on the Ge implanted samples provides the simulation results shown in figures 5-12 and 5-13. Simulated profiles at 750°C seem to have the appropriate increase in the B profile, though the increase is closer to the surface in the experimental profiles. The small increase over as-implanted profiles during the anneal at 825°C is overstated in the simulated profiles, and similarly displaced as the 750°C. Therefore, one can conclude the  $E_{GeB}^f \sim 0.5\text{eV}$  is the upper limit of the GeB pair formation energy.

## 5.4 Conclusions

An experiment is designed to investigate the Ge and B interaction in preamorphized silicon. The Si preamorphization provides a common amorphous layer depth, EOR damage distribution, and consequentially, the same interstitial supersaturation in the control and Ge implanted samples, with respect to depth and anneal time. The preamorphization also significantly reduces the formation of BICs, thus simplifying the diffusion of B in the control samples.

Assuming the GeB pair formation energy of 0.5eV, a model was implemented to simulate the implant and annealing conditions yielding reasonable fits to the experimental profiles. In order to confirm the existence of GeB pair, the same set of preamorphizing implants were performed on highly doped p-type wafers. Upon annealing, the control

samples exhibited a drop of B concentration near the surface, appropriately modeled by the BI trapping at the interface. In the same conditions, the Ge implanted samples exhibited an increase of B concentration. As the simulation slightly overstated the increase, one can conclude the upper boundary of the GeB pair formation energy is 0.5eV.

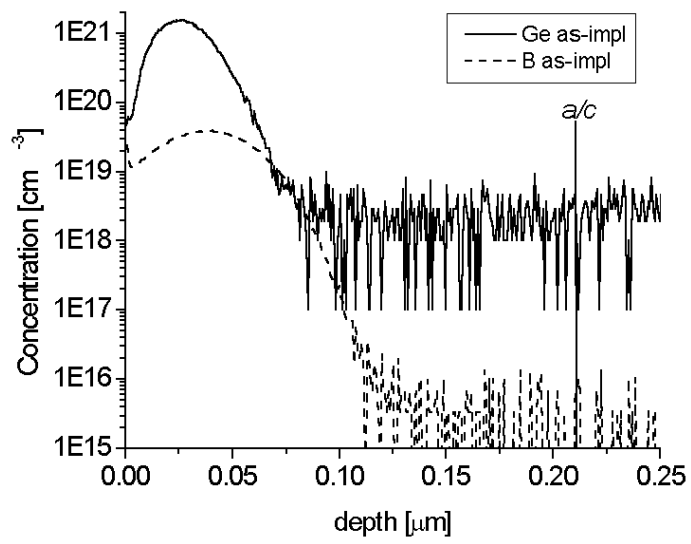


Figure 5-1. Profiles of B and Ge in as-implanted sample 2A

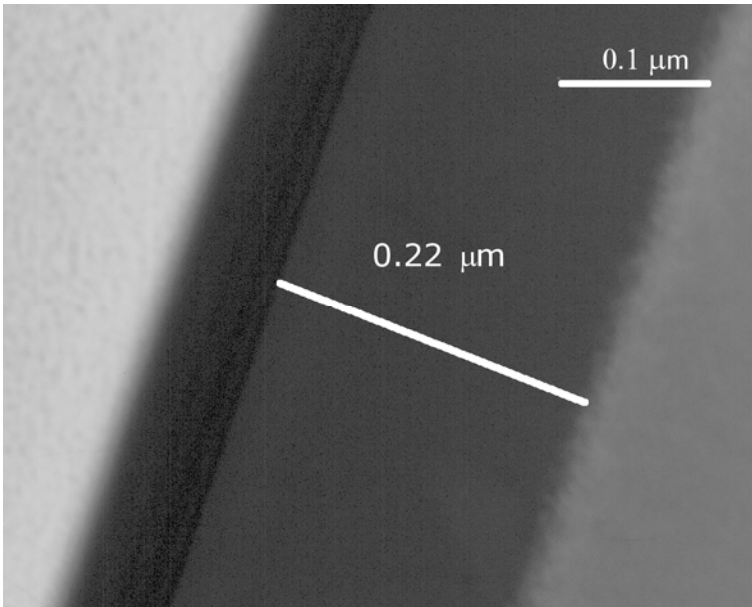
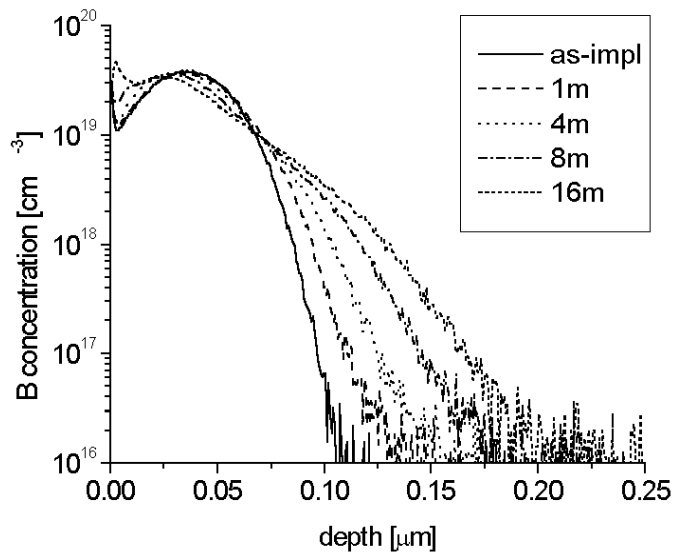
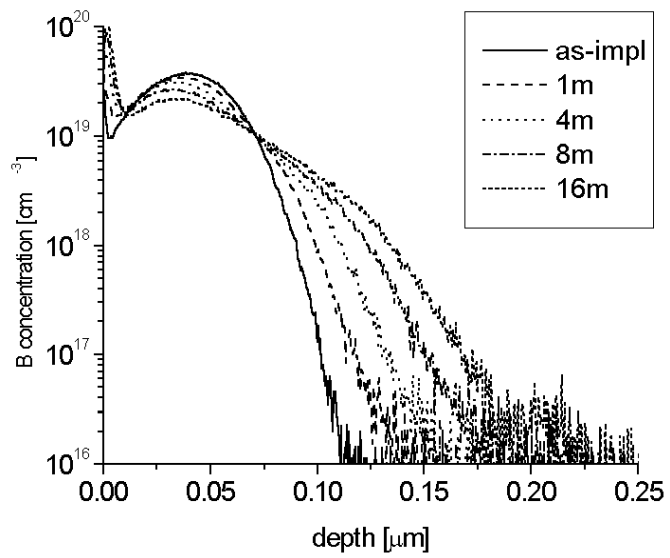


Figure 5-2. Cross-section TEM (XTEM) image of sample 2A under 100000 magnification



a)



b)

Figure 5-3. Boron profiles during the annealing at 780°C for: a) Ge implanted sample, b) control sample

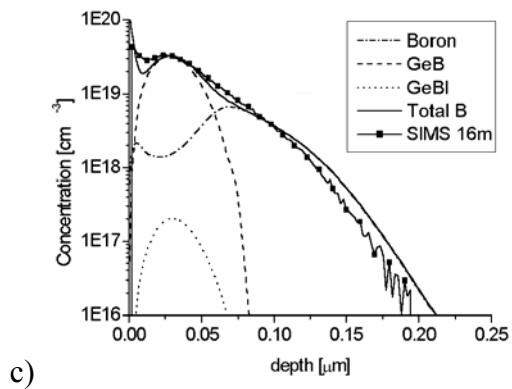
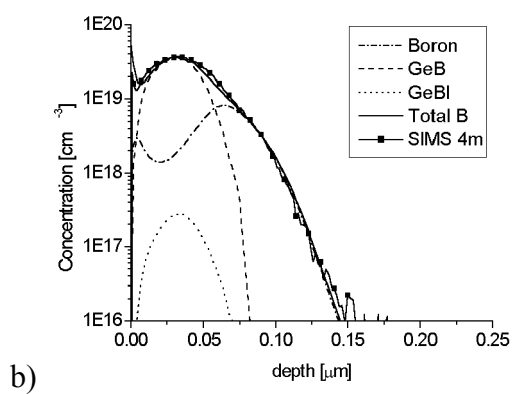
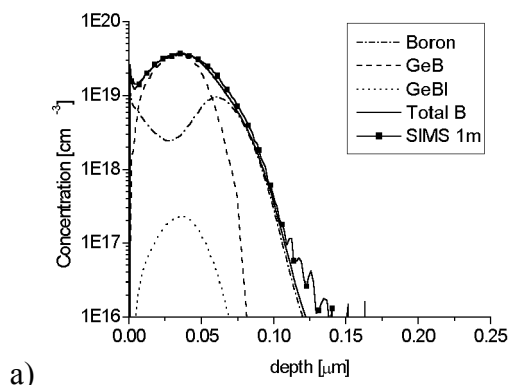


Figure 5-4. Simulated B profiles of Ge implanted sample during anneals at 780°C

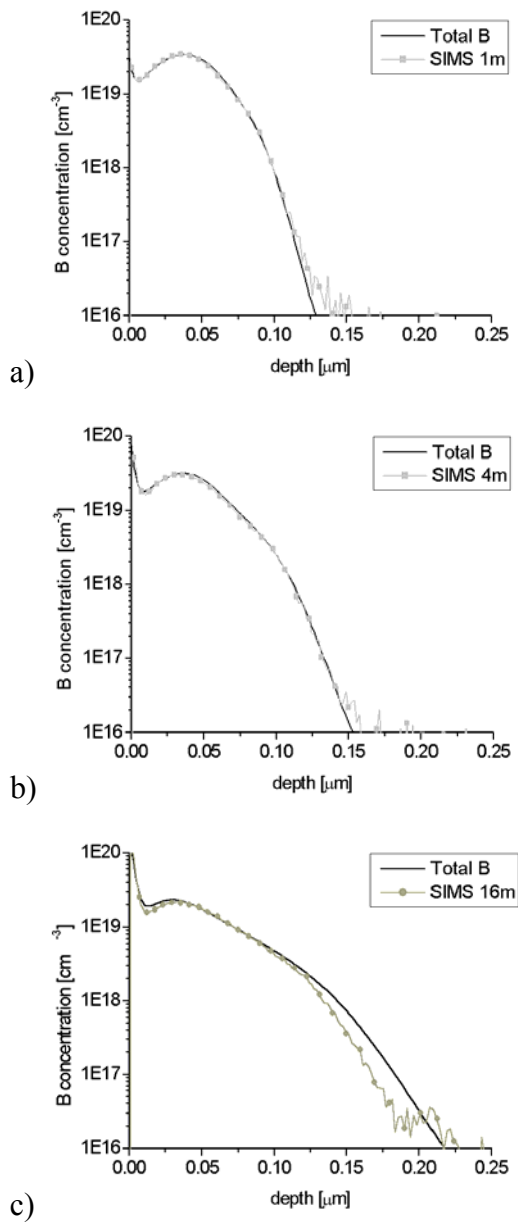


Figure 5-5. Simulated B profiles of control sample during anneals at 780°C

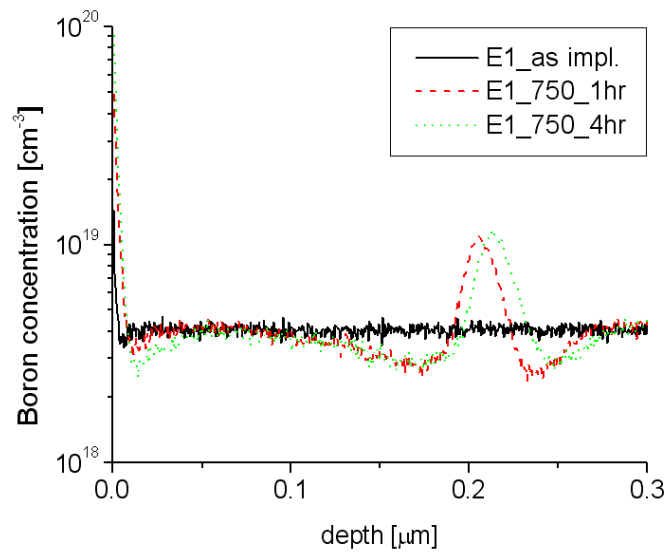


Figure 5-6. B profiles from control sample during annealing at 750 °C

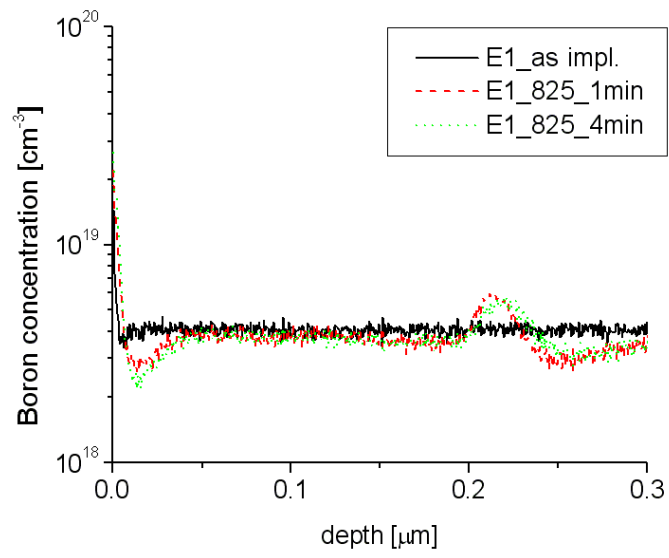


Figure 5-7. B profiles from control sample during annealing at 825°C

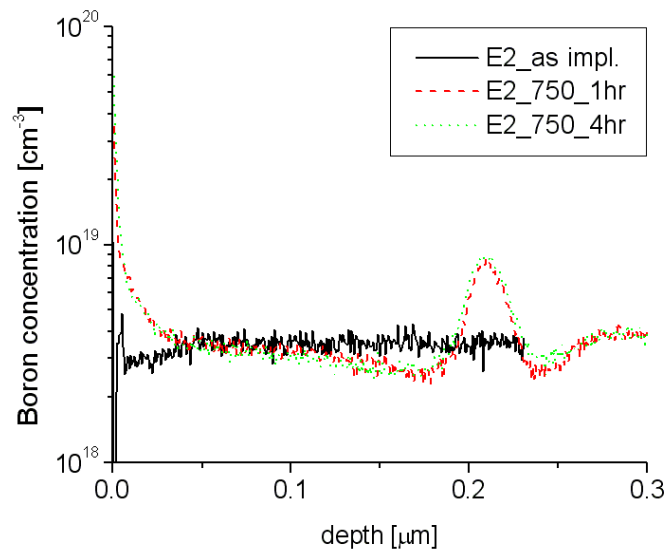


Figure 5-8. B profiles from Ge implanted sample during annealing at 750 °C

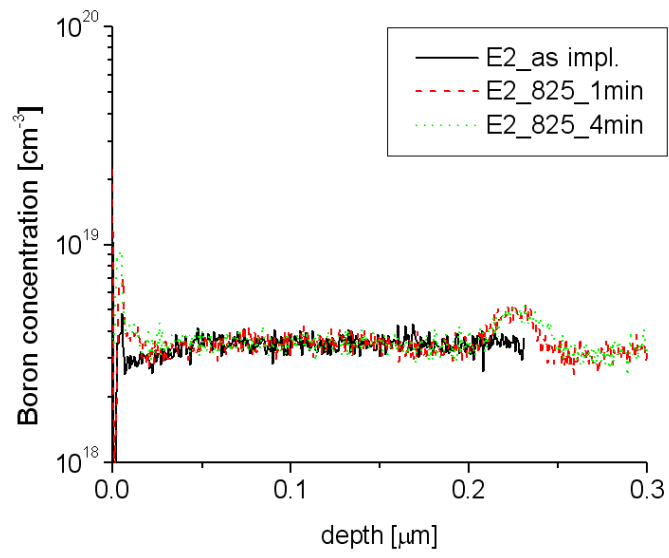


Figure 5-9. B profiles from Ge implanted sample during annealing at 825 °C

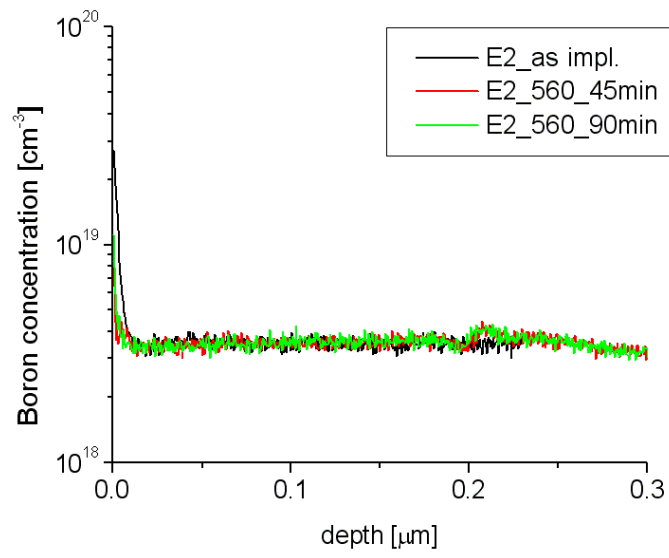


Figure 5-10. B profiles from Ge implanted sample during annealing at 560 °C

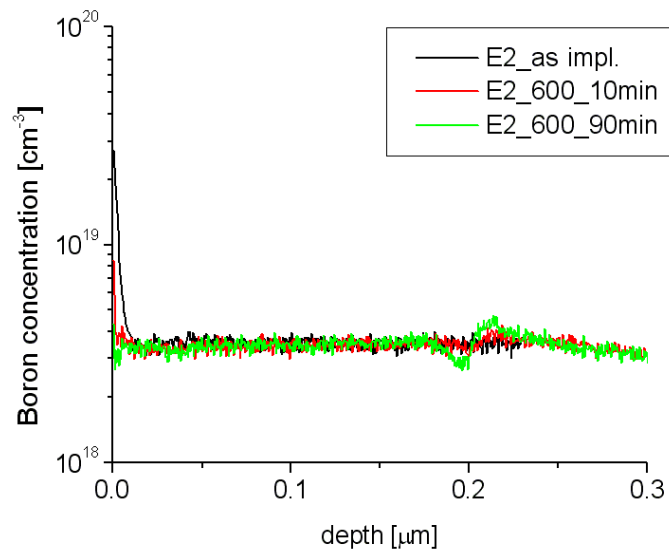
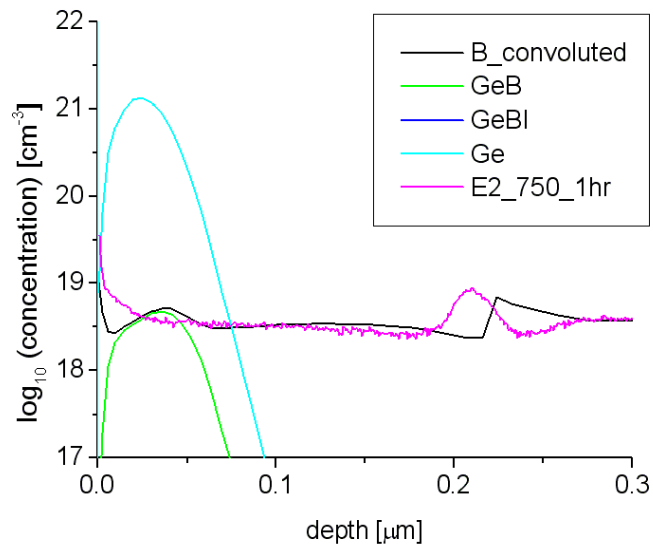
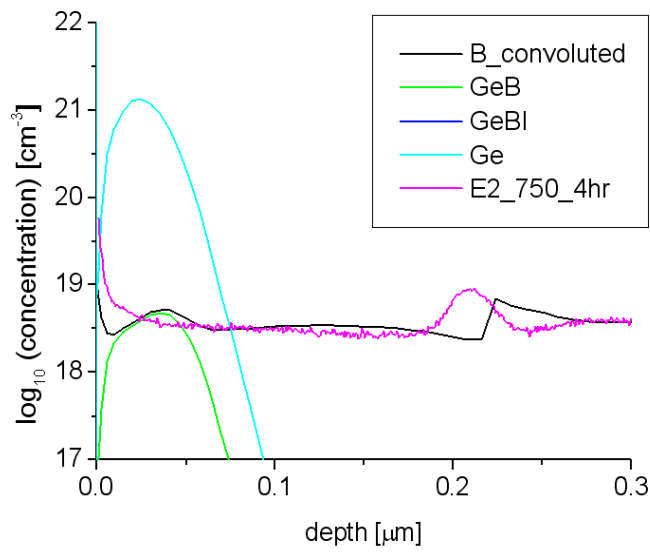


Figure 5-11. B profiles from Ge implanted sample during annealing at 600 °C

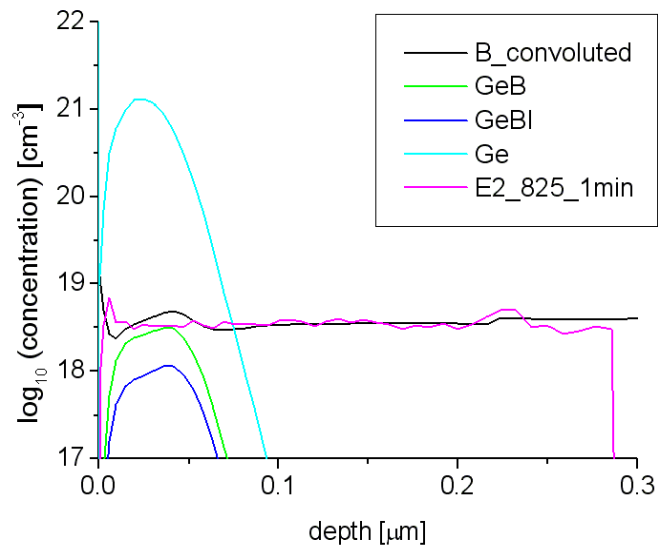


a)

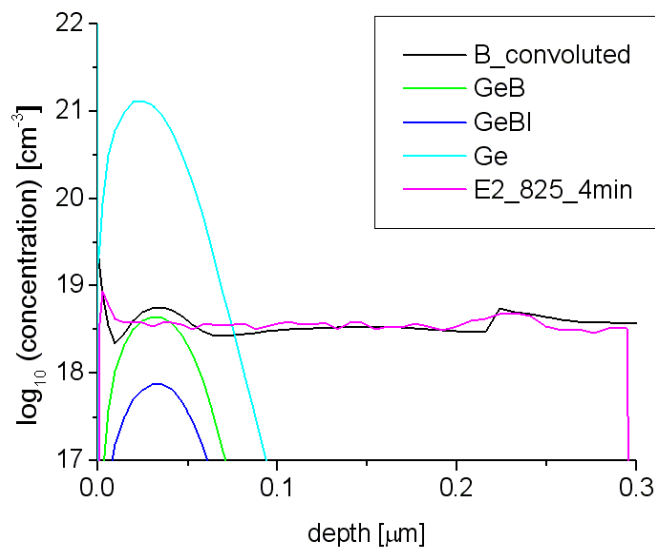


b)

Figure 5-12. Simulated B profiles from Ge implanted samples during annealing at 750°C



a)



b)

Figure 5-13. Simulated B profiles from Ge implanted samples during annealing at 825°C

## CHAPTER 6 SUMMARY AND FUTURE WORK

### 6.1 Summary

The work presented in this dissertation covers phenomena involving the diffusion of boron in silicon. These phenomena include the interaction of B with self-interstitials, Ge atoms and oxide/silicon interface.

The chapter on boron-interstitial clusters (BIC) discusses the formation of BICs in the crystalline and amorphous material. The negligible formation of BICs in the amorphous, and subsequently regrown layer is observed experimentally. Under the same annealing conditions, the B remaining in the crystalline material clustered almost completely with minimal observable diffusion. The model developed to capture the reactivation behavior of B captures several important characteristics of the experimental observation. First, the B marker immediately under the amorphous/crystalline interface clusters completely, with minimal diffusion. Second, the marker layer in the amorphous material experiences the enhanced diffusion without forming a clustering peak. Third, the marker layer removed from the peak of the excess interstitials experiences the enhanced diffusion and forms a small clustering peak.

The chapter also discusses the dissolution of BICs with respect to the annealing ambient. The change from the inert to an oxidizing ambient is demonstrated to reduce dissolution of BICs, thereby slowing the reactivation of B. Additionally, the reactivation appears to have two distinct regimes. The reactivation during the short times appears to be faster than at longer times, and fairly insensitive of ambient. At longer annealing

times, the reactivation depends strongly on ambient. The described features are qualitatively captured in the model describing the reactivation time dependence, its dependence on the annealing ambient, as well as the distinction in the cluster formation between the amorphous and crystalline phase.

The interaction between the Ge and B is examined under the interstitial supersaturation. The silicon preamorphization, the end-of-range damage and its consequential interstitial supersaturation serve to provide a common environment across implant conditions. During the course of this investigation, only the samples having no Ge implant exhibited an interesting dose loss and broadening of the surface spike. The surface spike is generally assumed to be an artifact of the transition between silicon dioxide and silicon matrix, not dependent on B concentration in oxide or silicon. Thus, the monotonic increase of B surface spike with control sample annealing time, combined with the dose loss at longer times, suggested a trapping mechanism at the oxide/silicon interface. The inclusion of an equation describing a trapping process yielded fits to the tail diffusion and surface spike increase, without altering other models or parameters.

The Si preamorphized, Ge implanted samples exhibited no change in the B surface spike, indicating the Ge interaction with B prevented the B diffusion to the surface. The negligible difference in the tail diffusion leads to conclusion that the BI releases its interstitial upon reacting with Ge, forming a GeB pair. Taking an increase in the activation energy of B diffusion as the formation energy of the GeB pair, a model yielded a reasonable fit to the experimental data. An additional experiment showed increase of B concentration above the as-implanted level of the highly doped p-type wafer, thus confirming the existence of the GeB pair.

## 6.2 Future Work

To fully characterize the interaction of B and Ge in silicon, one should investigate the full spectrum of  $\text{Si}_{1-x}\text{Ge}_x$  materials. As the material was not available during the time of this dissertation, an experimental design is presented in this chapter. The experiment aims to separate the influences of strain and the Ge chemical influence.

### 6.2.1 Material Specification – B Marker Layers in Relaxed $\text{Si}_{1-x}\text{Ge}_x$

For this experiment, relaxed  $\text{Si}_{1-x}\text{Ge}_x$  material of  $1\mu\text{m}$  thickness with flat Ge concentration, with  $<1\text{e}6 [\text{cm}^{-2}]$  lattice defects is required. Si capping layer should be around 10 nm. Interface Si cap/SiGe is the origin of the coordinate system.

Germanium contents desired are 0, 5, 10, 20, 30, 40 and 50 % Ge in Si, one wafer per Ge content. Relaxed  $\text{Si}_{1-x}\text{Ge}_x$  layer should be grown on top of a graded layer. Grading of 10 % Ge/ $\mu\text{m}$ , mentioned in the literature, is used in Fig. 6-1a. Ge profile in the  $1\mu\text{m}$  relaxed  $\text{Si}_{1-x}\text{Ge}_x$  material is flat, with four exceptions in 5, 10 and 20 % Ge material. For these Ge contents, four strained layers are desired. Two 10 nm thick compressively strained layers are desired at 430-440 and 560-570 nm depth, with double Ge content of surrounding material. Also, two 10 nm thick tensile strained layers are desired at 460-470 and 530-540 nm depth, with 0% Ge content. The thickness of 10nm is less than the critical thickness of 20% Ge strained layer, according to the Mathews-Blakeslee criterion.

Boron profiles have the same specification for all  $\text{Si}_{1-x}\text{Ge}_x$  wafers. Within the flat part of Ge profiles are three B marker layers (delta doped), positioned at depths of 0.2, 0.5 and 0.8  $\mu\text{m}$ , as illustrated in Fig. 6-1b. Peak concentrations of these markers are  $2\times 10^{19}$ ,  $1\times 10^{18}$  and  $1\times 10^{18} [\text{cm}^{-3}]$ , respectively.

### 6.2.2 Information Expected

This material specification allows the measurement of B diffusivity in intrinsic (deepest B marker) and extrinsic (shallowest B marker) case with respect to Ge content in relaxed  $\text{Si}_{1-x}\text{Ge}_x$ . The middle marker layer diffuses through tensile and compressively strained  $\text{Si}_{1-x}\text{Ge}_x$  layers, which may elucidate the influence of strain, and can be directly compared to the deepest B marker. The strained silicon cap allows for the definitive point defect injection through the oxidizing and nitridizing ambients, useful in determining the fractional interstitial and vacancy diffusivities of B with respect to Ge content.

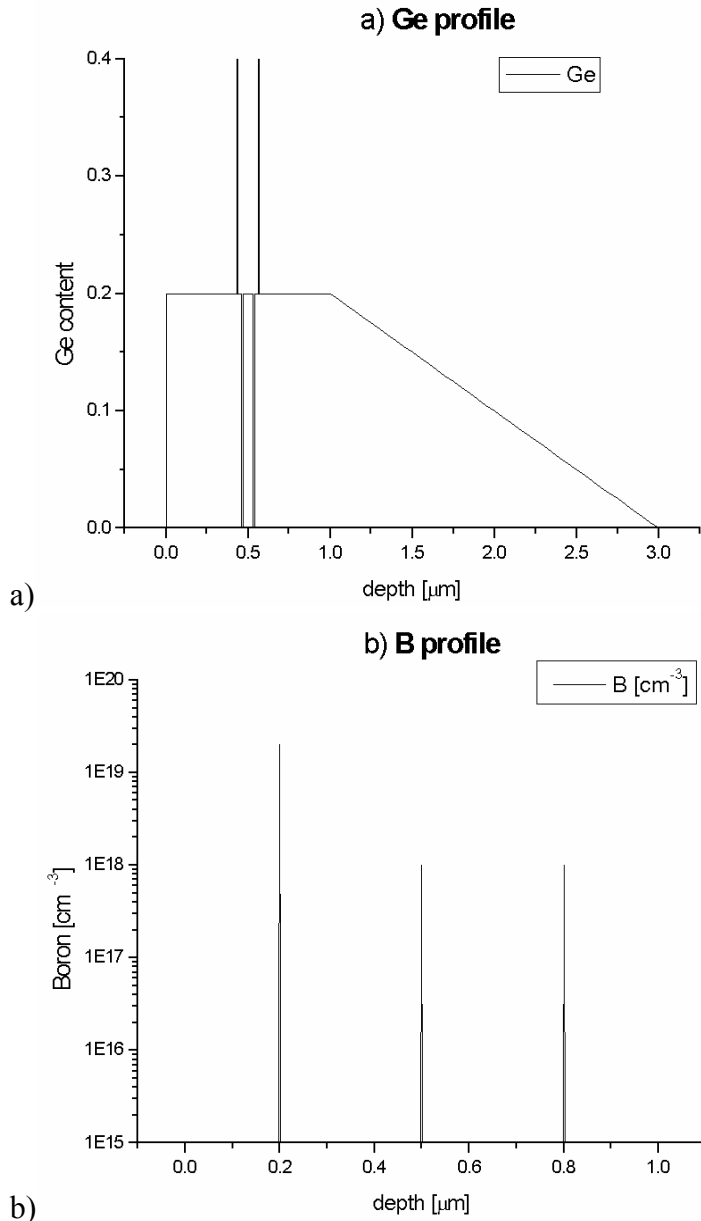


Figure 6-1. Dopant profiles in a  $\text{Si}_{1-x}\text{Ge}_x$  material. Figure a) contains Ge profile for  $\text{Si}_{0.8}\text{Ge}_{0.2}$  material, while figure b) has B profile

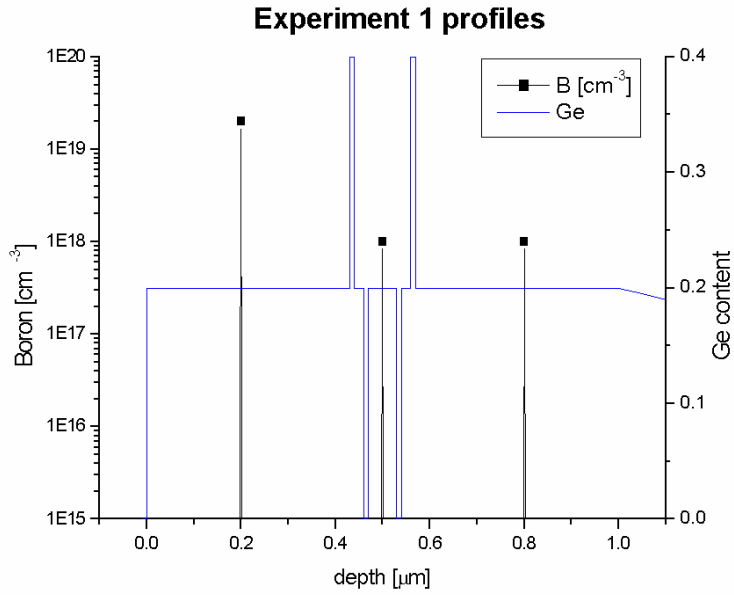


Figure 6-2. Boron profile in  $\text{Si}_{0.8}\text{Ge}_{0.2}$  material

## LIST OF REFERENCES

- [Azi99] M. J. Aziz, *Appl. Phys. Lett.* 70, 2810 (1997)
- [Bau69] R. Bauerlein, *Radiation damage in solids*, D. S. Bellington, Ed., p. 358, Academic Press, New York (1969)
- [Bra95] H. Bracht, N. A. Stolwijk, and H. Mehrer, *Phys. Rev. B* 52, 16542 (1995)
- [Bra98] H. Bracht, E. E. Haller, and R. Clark-Phelps, *Phys. Rev. Lett.* 81, 393 (1998)
- [Cat98] M. J. Caturla, M. D. Johnson, and T. Diaz de la Rubia, *Appl. Phys. Lett.* 72, 2736 (1998)
- [Cha96] H. S. Chao, P. B. Griffin, and J. D. Plummer, *Appl. Phys. Lett.* 68, 3570 (1996)
- [Chr81] L. A. Christel, J. F. Gibbons, and T. W. Sigmon, *J. Appl. Phys.* 52, 7143 (1981)
- [Cla02] M. H. Clark, K. S. Jones, T. E. Haynes, C. J. Barbour, K. G. Minor, and E. Andideh, *Appl. Phys. Lett.* 80, 4163 (2002)
- [Cow99] N. E. B. Cowern, G. Mannino, P. A. Stolk, F. Roozeboom, H. G. A. Huizing, J. G. M. van Berkum, F. Cristiano, A. Claverie, and M. Jaraíz, *Phys. Rev. Lett.* 82, 4460 (1999)
- [Dut91] D. Dutartre, G. Brémond, A. Souifi, and T. Benyattou, *Phys. Rev. B* 44, 11525 (1991)
- [Eag94] D. J. Eaglesham, P. A. Stolk, H.-J. Gossmann, and J. M. Poate, *Appl. Phys. Lett.* 65, 2305 (1994)
- [Fah85] P. Fahey, G. Barbuscia, M. Moslehi, and R. W. Dutton, *Appl. Phys. Lett.* 46, 784 (1985)
- [Fah89a] P. M. Fahey, P. B. Griffin, and J. D. Plummer, *Rev. Mod. Phys.* 61, 289 (1989)
- [Fah89b] P. Fahey, S. S. Iyer, and G. J. Scilla, *Appl. Phys. Lett.* 54, 843 (1989)
- [Fai81] R. B. Fair, *Impurity Doping Processes in Silicon*, edited by F. F. Y. Wang, p. 315, North Holland, Amsterdam, (1981)
- [Fan96] T. T. Fang, W. T. C. Fang, P. B. Griffin, and J. D. Plummer, *Appl. Phys. Lett.* 68, 791 (1996)

- [FLO02] FLorida Object Oriented Process Simulator, University of Florida, Florida 2002.
- [Gos97] H.-J. Gossmann, T. E. Haynes, P. A. Stolk, D. C. Jacobson, G. H. Gilmer, J. M. Poate, H. S. Luftman, T. K. Mogi, and M. O. Thompson, *Appl. Phys. Lett.* 71, 3862 (1997)
- [Gri00] M. Griglione, T. J. Anderson, Y. M. Haddara, M. E. Law, K. S. Jones, and A. van den Bogaard, *J. Appl. Phys.* 88, 1366 (2000)
- [Gri01] M. Griglione, T. J. Anderson, M. E. Law, K. S. Jones, A. van den Bogaard, and M. Puga-Lambers, *J. Appl. Phys.* 89, 2904 (2001)
- [Gri85] P. B. Griffin, P. M. Fahey, J. D. Plummer, and R. W. Dutton, *Appl. Phys. Lett.* 47, 319 (1985)
- [Had00] Y. M. Haddara, B. T. Folmer, M. E. Law, and T. Buyuklimanli, *Appl. Phys. Lett.* 77, 1976 (2000)
- [Hu74] S. M. Hu, *J. Appl. Phys.* 45, 1567 (1974)
- [Imp06] [http://eserver.bell.ac.uk/semicd/semi\\_p/topics/implant/imp\\_e2.htm](http://eserver.bell.ac.uk/semicd/semi_p/topics/implant/imp_e2.htm), Aug 2006
- [Jai03] S. H. Jain, P. B. Griffin and J. D. Plummer. *J. Appl. Phys.* 93 (2), 1060 (2003)
- [Jon96a] K. S. Jones, R. G. Elliman, M. M. Petravic, and P. Kringhøj, *Appl. Phys. Lett.* 68, 3111 (1996)
- [Jon96b] K. S. Jones, J. Liu, and L. Zhang, *Proceedings of Spring Electrochemical Soc. Meeting*, 96-4, 116 (1996)
- [Kil59] Jack Kilby, US3138743, US3138747, US3261081, and US3434015 patents
- [Kri96] P. Kringhøj, *Appl. Phys. Lett.* 68, 247 (1996)
- [Kri97] P. Kringhøj and A. Nylandsted Larsen, *Phys. Rev. B* 56, 6396 (1997)
- [Kuo93] P. Kuo, J. L. Hoyt, J. F. Gibbons, J. E. Turner, R. D. Jacowitz, and T. I. Kamins, *Appl. Phys. Lett.* 62, 612 (1993)
- [Kuo95a] P. Kuo, J. L. Hoyt, J. F. Gibbons, J. E. Turner, and D. Lefforge, *Appl. Phys. Lett.* 66, 580 (1995)
- [Kuo95b] P. Kuo, J. L. Hoyt, J. F. Gibbons, J. E. Turner, and D. Lefforge, *Appl. Phys. Lett.* 67, 706 (1995)
- [Lai03] P. Laitinen, I. Riihimaki, and J. Raisanen, *Physical Review B* 68, 155209 (2003)

- [Lan85] D. V. Lang, R. People, J. C. Bean, and A. M. Sergent, *Appl. Phys. Lett.* 47, 1333 (1985)
- [Lev98] R. F. Lever, J. M. Bonar, and A. F. W. Willoughby, *J. Appl. Phys.* 83, 1988 (1998)
- [Lil02] A. D. Lilak, M. E. Law, L. Radic, K. S. Jones, and M. Clark, *Appl. Phys. Lett.* 81, 2244 (2002)
- [Lil30] J. E. Lilienfeld, Method and apparatus for controlling electric currents, US Patent 1,745,175, application filed October 8, 1926, granted January 18, 1930; J.E. Lilienfeld, Device for controlling electric current, US Patent 1,900,018 application filed March 28, 1928, patented March 7, 1933
- [Lil97] A. D. Lilak, M. E. Law, K. S. Jones, M. D. Giles, and S. K. Earles, *IEDM*, 493 (1997)
- [Lin63] J. Lindhart, M. Scharff, and H. Schiott, *Mat.-Fys. Med. Dan. Vid. Selsk* 33, 1 (1963)
- [Liu00] X.-Y. Liu, W. Windl, and M. P. Masquelier, *Appl. Phys. Lett.* 77, 2018 (2000)
- [May70] J. W. Mayer, L. Erikson and J. A. Davies, *Ion Implantation in Semiconductors*, p. 24, Academic Press, New York (1970)
- [Mic87] A. E. Michel, W. Rausch, P. A. Ronsheim, and R. H. Kastl, *Appl. Phys. Lett.* 50, 416 (1987)
- [Mir03] S. Mirabella, E. Bruno, F. Priolo, D. De Salvador, E. Napolitani, A. V. Drigo, and A. Carnera, *Appl. Phys. Lett.* 83, 680 (2003)
- [Mog96] T. K. Mogi, Michael O. Thompson, H.-J. Gossmann, J. M. Poate, H. S. Luftman, *Appl. Phys. Lett.* 69, 1273 (1996)
- [Moo03] G. E. Moore, presentation at International Solid State Circuits Conference (ISSCC), February 10, 2003 (<http://www.intel.com/technology/silicon/mooreslaw/index.htm>, Aug 2006)
- [Moo65] G. E. Moore, *Electronics* 38 (1965)
- [Mor93] N. Moriya, L. C. Feldman, H. S. Luftman, C. A. King, J. Bevk, and B. Freer, *Phys. Rev. Lett.* 71, 883 (1993)
- [Nic89] C. S. Nichols, C. G. van de Walle, S. T. Pantelides, *Phys. Rev. Lett.* 62 (1989) 1049; C. S. Nichols, C. G. van de Walle, S. T. Pantelides, *Phys. Rev. B* 40 (1989) 5484
- [Ols88] G. L. Olson, J. A. Roth, *Material Science Reports* 3, 1 (1988)

- [Pac90] P. A. Packan and J. D. Plummer, *J. Appl. Phys.* 68, 4327 (1990)
- [Pel97] L. Pelaz, M. Jaraiz, G. H. Gilmer, H.-J. Gossmann, C. S. Rafferty, D. J. Eaglesham, and J. M. Poate, *Appl. Phys. Lett.* 70, 2285 (1997)
- [Pel99] L. Pelaz, V. C. Venezia, H.-J. Gossmann, G. H. Gilmer, A. T. Fiory, C. S. Rafferty, M. Jaraiz, and J. Barbolla, *Appl. Phys. Lett.* 75, 662 (1999)
- [Peo85] R. People, *Phys. Rev. B* 32, 1405 (1985)
- [Psi06] [http://www.psiberaudio.com/tube\\_history\\_2.htm](http://www.psiberaudio.com/tube_history_2.htm), Aug 2006
- [Rob92] D. J. Robbins, L. T. Canham, S. J. Barnett, A. D. Pitt, and P. Calcott, *J. Appl. Phys.* 71, 1407 (1992)
- [Sas88] Y. Sasaki, K. Itoh, E. Inoue, S. Kishi, T. Mitsuishi, *Solid State Electronics* 31, 5 (1988)
- [See68] A. Seeger, K. P. Chik, *Physica Status Solidi* 29, 455 (1968)
- [Sol00] S. Solmi, M. Bersani, M. Sbeti, J. Lundsgaard Hansen, A. Nylandsted Larsen, *J. Appl. Phys.* 88, 4547 (2000)
- [Sto95] P. A. Stolk, H.-J. Gossmann, D. J. Eaglesham, D. C. Jacobson, J. M. Poate, and H. S. Luftman, *Appl. Phys. Lett.* 66, 568 (1995)
- [Str02] A. Strohm, T. Voss, W. Frank, P. Laitinen, J. Raisanen, *Zeitschrift fur Metallkunde* 93, 737 (2002)
- [Ura98] A. Ural, P. B. Griffin, and J. D. Plummer, *Appl. Phys. Lett.* 73, 1706 (1998)
- [Ura99a] Ant Ural, Peter B. Griffin, and James D. Plummer, *J. Appl. Phys.* 85, 6440 (1999)
- [Ura99b] Ant Ural, Peter B. Griffin, and James D. Plummer, *Phys. Rev. Lett.* 83, 3454 (1999)
- [UTM00] UT-Marlowe version 5.0, University of Texas, Austin, Texas 2000.
- [Vic69] G. L. Vick and K. M. Whittle, *J. Electrochem. Soc.* 116, 1142 (1969)
- [Vuo96] H.-H. Vuong, C. S. Rafferty, S. A. Eshraghi, J. L. Lentz, P. M. Zeitzoff, M. R. Pinto, and S. J. Hillenius, *IEEE Transactions on Electron Devices* 43, 1144 (1996)
- [Web89] J. Weber and M. I. Alonso, *Phys. Rev. B* 40, 5683 (1989)
- [Wil01] A. F. W. Willoughby, J. M. Bonar, A. H. Dan, and B. M. McGregor, *Diffusions in materials: DIMAT2000, Defect And Diffusion Forum* 194-1, 717 (2001)

- [Wil84] J. S. Williams and J. M. Poate, *Ion Implantation and Beam Processing*, p. 1, Academic Press, New York, (1984)
- [Win99] W. Windl, M. M. Bunea, R. Stumpf, S. T. Dunham, and M. P. Masquelier, *Phys. Rev. Lett.* 83, 4345 (1999)
- [Xia99] J. Xia, T. Saito, R. Kim, T. Aoki, Y. Kamakura, and K. Taniguchi, *J. Appl. Phys.* 85, 7597 (1999)
- [Zan01] N. R. Zangenberg, J. Lundsgaard Hansen, J. Fage-Pedersen, and A. Nylandsted Larsen, *Phys. Rev. Lett.* 87, 125901 (2001)
- [Zan03] N. R. Zangenberg, J. Fage-Pedersen, J. Lundsgaard Hansen, and A. Nylandsted Larsen, *J. Appl. Phys.* 94, 3883 (2003)
- [Zie00a] J. F. Zeigler. *Ion Implantation Science and Technology*, 214 (2000)
- [Zie00b] J. F. Zeigler. *Ion Implantation Science and Technology*, 303 (2000)

## BIOGRAPHICAL SKETCH

Ljubo Radic was born in Zagreb, Croatia, on August 13<sup>th</sup>, 1975. He attended the XV Gymnasium from 1989 until 1993 prior to studies of electrical engineering at the University of Zagreb. During the first year studies he received an award for academic excellence “Josip Loncar,” and graduated as a valedictorian on the 30<sup>th</sup> of June 1998. The graduate education commenced in August 2000, as he joined the University of Florida to study electron device processing and simulation. The graduate research involved boron diffusion in silicon, the transient diffusion and interaction with germanium, clustering and cluster dissolution phenomena. Upon the completion of the graduate education and the receipt of the Doctor of Philosophy degree, he will join the Freescale Semiconductor modeling and simulation group.